# TECHNIQUES AND TECHNOLOGIES FOR FAR-INFRARED ASTRONOMY

**GEOFFREY ROBERT HURT SITWELL**
**Bachelor of Science, University of Lethbridge, 2016**

A thesis submitted
in partial fulfillment of the requirements for the degree of

**MASTER OF SCIENCE**
in
**PHYSICS**

Department of Physics and Astronomy
University of Lethbridge
LETHBRIDGE, ALBERTA, CANADA

TECHNIQUES AND TECHNOLOGIES FOR FAR-INFRARED ASTRONOMY

GEOFFREY ROBERT HURT SITWELL

Date of Defence: July 15, 2019

| | | |
|---|---|---|
| Dr. Locke Spencer<br>Thesis Supervisor | Associate Professor | Ph.D. |
| Dr. David Naylor<br>Thesis Examination Committee Member | Professor | Ph.D. |
| Dr. Kenneth Vos<br>Thesis Examination Committee Member | Associate Professor | Ph.D. |
| Dr. Behnam Seyed-Mahmoud<br>Chair, Thesis Examination Committee | Associate Professor | Ph.D. |

# Dedication

This thesis is dedicated to my nana Noreen Sitwell who taught me everything I needed outside the classroom.

# Abstract

Far infrared astronomy is pivotal to our understanding of how the universe evolved, from the earliest galaxies to ongoing star and planet formation. Observations in the far infrared, however, are limited by thermal radiation in optics, and low spatial resolution.

Reducing the noise brought about by thermal radiation of optical systems used in far infrared astronomy requires cryogenically cooled components. It is therefore important to understand how the physical properties of structural materials change in the cryogenic regime in order to understand their behaviour at operational temperatures. The design of a dedicated cryogenic materials testing site for probing thermal contraction and thermal conductivity of materials is presented.

The characterization of two nanometer precision metrology systems is discussed, and the systems are used to measure the thermal contraction of aluminium and carbon fibre reinforced polymers to temperatures below 10 K. Suggestions for improvements in the experimental procedure are provided.

# Acknowledgments

I would like to first acknowledge my supervisor Dr. Locke Spencer for sparking my interest in research. From taking me on as an undergraduate research assistant more than five years ago, to helping me through my undergraduate honours thesis, and now through my masters degree. Your tutelage has been invaluable in my development as an academic and I am incredibly grateful to have had you as my mentor.

Additionally, I would like to thank all of the many professors who have taught me over the years, particularly Dr. David Naylor whose course on cosmology played an integral role in convincing me to pursue physics, and Dr. Adriana Predoi-Cross who first encouraged me to approach Locke concerning a summer work position.

I would never have been able to accomplish the work in this thesis without the help of all the members of both the Spencer and Naylor groups. In particular Ian Veenendaal and Tony Huber who taught me everything I know about cryogenics, and Vince Weiler whose assistance with circuitry and metrology experiments was critical. Adam Christiansen and Rebecca Sirota also deserve special thanks for their development of the metrology systems used in experimentation, and for their patient attention in diagnosing them. Thank you to Geoff Minors for machining the components in my mechanical design work, despite occassionally lacking technical drawings. Thank you as well to our department secretary Catherine Drenth for your support.

Chris Benson and Jeremy Scott have been constant resources in both classwork and labwork and I thank you both for your support. Countless other classmates and labmates through the years have contributed not only to my academic success, but have served as important commiserators when things weren't going to plan.

Thank you to my wonderful girlfriend Alison Jang for all the time you put into editing figures in my work as well as your constant love and support through a stressfull time. I'd like to finish off by thanking all of my loving family for their constant encouragement through my post-secondary career, and indeed my entire life. Without the support of my loved ones the work in this thesis would never have been possible.

I must also acknowledge the support I've received from numerous institutions over the years and thank those who have made their wonderful software packages available freely. Thank you to the the school of graduate studies at the University of Lethbridge, CFI, and NSERC for the funding which has enabled me to do this work. Thanks to the Herschel Science Archive which was used to access data and generate plots of Herschel data. Likewise a thank you to the CADC who host and make available the JCMT data used in this thesis. The astropy distribution was used in generating astronomical figures with world coordinate systems and was very helpful. Finally a thank you to our collaborators through the CRN at Glyndwr University and UBC who provided us with CFRP samples for testing.

# Contents

# List of Tables

# List of Figures

# List of Abbreviations

**ALMA** Atacama Large Millimeter Array.

**CFRP** Carbon Fibre Reinforced Polymers.

**COBE** Cosmic Background Explorer.

**CTE** Coefficient of Thermal Expansion.

**CTIC** Cryogenic Thermal Isolation Chamber.

**EGO** Extended Green Object.

**ESA** European Space Agency.

**FIR** Far Infrared.

**FPGA** Field Programmable Gate Array.

**GLIMPSE** Galactic Legacy Infrared Mid-Plane Survey Extraordinaire.

**HIFI** Heterodyne Instrument for the Far-Infrared.

**IMF** Initial Mass Function.

**IRAC** Infrared Array Camera.

**IRAS** Infrared Astronomical Satellite.

**ISM** Interstellar Medium.

**ISO** Infrared Space Observatory.

**JCMT** James Clark Maxwell Telescope.

**JWST** James Webb Space Telescope.

**MIPS** Multiband Imaging Photometer.

**NIST** National Institute of Standards and Technology.

**OPD** Optical Path Difference.

**PSO** Position Synchronized Output.

**PTC** Pulse Tube Cooler.

**RMS** Root Mean Squared.

**SNR** Signal to Noise Ratio.

| | |
|---|---|
| **SPICA** | Space Infrared Telescope for Cosmology and Astrophysics. |
| **SPIRE** | Spectral and Photometric Imaging Receiver. |
| **TEC** | Thermo-Electric Control. |
| **TFC** | Test Facility Cryostat. |
| **VLA** | Very Large Array. |
| **WMAP** | Wilkinson Microwave Anisotropy Probe. |

# List of Symbols

| | |
|---|---|
| **Chapter One** | |
| $\lambda$ | Wavelength |
| $T$ | Temperature |
| $z$ | Redshift |
| $E$ | Energy |
| $h$ | Planck Constant |
| $\nu$ | Frequency |
| $c$ | Speed of Light |
| $\theta$ | Angle |
| $D$ | Diameter |
| **Chapter Two** | |
| $\Delta S$ | Mass Used in New Star Creation |
| $\phi(M)$ | Initial Mass Function |
| $M$ | Mass |
| $\mathcal{N}_M dM$ | Number of New Stars in Interval $(M + dM)$ |
| $K$ | Empirical Constant |
| $k_B$ | Boltzmann Constant |
| $G$ | Gravitational Constant |
| $m$ | Molar Mass |
| $\rho$ | Mass Density |
| $A, B$ | Chemical Variables |
| $\gamma$ | Photon |
| $e^-$ | Electron |
| $I$ | Ionization Potential |
| $n_H$ | Volumetric Density of Atomic Hydrogen |
| $J_\nu$ | Mean Intensity of Radiation |
| $a_\nu$ | Cross-section for Ionization |
| $n_e$ | Volumetric Density of Electrons |
| $n_p$ | Volumetric Density of Protons |
| $\alpha_a$ | Cross-section for Recombination to All Levels |
| $\alpha_{nL}$ | Cross-section for Recombination to a Given Level |
| $B_\nu$ | Blackbody Function |

| | |
|---|---|
| $G(H)$ | Ionization Heating |
| $\nu_0$ | Ionization Frequency |
| $T_*$ | Stellar Temperature |
| $p^+$ | Proton |
| $R_*$ | Stellar Radius |
| $S_*$ | Rate of Production of Ionizing Photons |
| $r$ | Radius |
| $\rho_{Phot}$ | Spatial Density of Ionizing Photons |
| $\dot{\mathcal{N}}_I$ | Ionization Rate per unit Volume |
| $\dot{\mathcal{N}}_n$ | Recombination Rate to Level $n$ per unit Volume |
| $\beta_n$ | Recombination Coefficient to Level $n$ |
| $\dot{\mathcal{N}}_R$ | Recombination Rate to All Levels per unit Volume |
| $x$ | Fractional Ionization |
| $\Delta\sigma$ | Frequency Spacing |
| $L_{OPD}$ | Length in Optical Path Difference |

**Chapter Four**

| | |
|---|---|
| $C_V$ | Molar Heat Capacity |
| $N_A$ | Number Density of Atoms |
| $N_e$ | Number Density of Electrons |
| $\theta_D$ | Debye Temperature |
| $K_1$ | Multiplicative Constant |
| $\epsilon_D$ | Debye Cutoff Energy |
| $c_D$ | Constant Related to Electron Heat Capacity |
| $\vec{q}$ | Heat Flux |
| $\kappa$ | Thermal Conductivity |
| $Q$ | Heat |
| $A_{CS}$ | Cross-sectional Area |
| $\dot{Q}$ | Rate of Heat Exchange |
| $L$ | Length |
| $y(T)$ | Thermal Conductivity or Specific Heat (Depending on values of coefficients) |
| $c_i$ | Coefficients for Analytical Approximation of Thermal Conductivity or Specific Heat |
| $L_T$ | Length at Temperature, T |
| $L_{293}$ | Length at 293 K |
| $\alpha$ | Coefficient of Thermal Expansion |
| $\mathcal{A}$ | Area of emitting surface |
| $\varepsilon$ | Emissivity |
| $\sigma_{SB}$ | Stefan-Boltzmann Constant |
| $v$ | Velocity |
| $t$ | Time |

| | |
|---|---|
| $n$ | Number |
| $M_{Mol}$ | Molar Mass |
| **Appendix A** | |
| $C$ | Capacitance |
| $\epsilon_0$ | Permittivity of Free Space |
| $\epsilon_r$ | Relative Permittivity of a Dielectric |
| $A_{Cap}$ | Area of Capacitor |
| $d$ | Distance |

# Thesis Format

This thesis was typeset using Latex using an adapted version of the thesis template provided by the Math and Computer Science Department of the University of Lethbridge , `uleththesis.cls`. Images have been generated using the Scientific PYthon Development EnviRonment (SPYDER), the Herschel Interactive Processing Environment (HIPE), and SolidWorks unless otherwise stated. Labeling of images was done using Adobe Photoshop.

This thesis uses the following conventions:

**References** External references to works by other authors are denoted by numbers in square parentheses (e.g. [4,5] indicates a refers to references 4 and 5). Internal cross-references are denoted by Type a.b.c. where “Type” refers to a chapter, section, or subsection and a.b.c. refer to the number of the chapter, section, and subsection respectively. Figure, table, and equation numbers are denoted by Type a.b., where “Type” refers to a figure, table, or equation, and a.b. represent the chapter and ordering respectively (e.g. Figure 1.7 refers to the seventh figure in the first chapter).

**Equations** Equation units are included in square parenthesis following each equation (e.g $F = ma \quad [\mathrm{N}]$ indicates units of newtons).

**Units** An attempt has been made to use SI units throughout this work. Angles are presented in units of degrees, arcminutes, and arcseconds to remain consistent with astronomical standards. Temperature is presented both in kelvin and degrees celsius, though the latter is only used in reference to temperatures about room temperature (293 K).

**Uncertainties** Uncertainties are presented inside parenthesis after the mean value and are taken to be in the nearest digits (e.g, 17.8(1) is 17.8±0.1, and 21.94(3.01) is taken to mean 21.94±3.01).

# Chapter 1

# Introduction

While early humans recognized the utility of stars for navigation and story-telling, they likely did not realize that stargazing would one day yield answers to some of the most fundamental questions for which they desperately sought answers. Questions about the origin and evolution of the universe have piqued human curiosity and been intimately linked to our cultures and mythologies, and many of the same questions about the nature of the universe which concerned early humans still linger today. While the last few centuries have resulted in enormous milestones in the fields of astronomy and cosmology, the advancements in discovery have only left us with more questions. As an example, consider that less than one hundred years ago the National Academy of Science in Washington hosted a debate about whether the Milky Way galaxy was the entire universe [1]. Estimates based on Planck telescope results released in 2015 suggest that in terms of energy density the universe is only approximately 30% matter, and of that matter approximately 80% is undetected 'Dark Matter' [2]. In less than a century we have gone from observing the entire universe, to observing less than 5% of it.

If we wish to learn more about the universe the best method is to inspect it. Since astronomers are confined to Earth, in-situ experimentation has only recently been made available[3, 4], and only for objects relatively near to the Earth, therefore anything learned about distant astronomical sources must be inferred from the radiation (and more recently gravitational waves [5]) seen coming from those sources. The type of electromagnetic radiation coming from a source can inform astronomers about the atomic, ionic, and molecular gases and dust present in the source. It can also sometimes be used to measure temperatures and densities, magnetic field strengths, and the motion of gases within the source. The intensity of radiation in different spectral bands can also carry information about the type of source, for instance, far-infrared (FIR) observations are used to examine some of the coldest objects in the universe, x-ray observatories by contrast, focus on very energetic regions of space with high temperature, such as supernovae remnants. The focus of the work contained within this thesis is on advancing observational techniques and technologies in the FIR with the goal of improving the existing knowledge on star forming regions. Despite the focus on star formation, FIR observations can help to fill in the gaps in knowledge about other important scientific topics as well.

The European Space Agency (ESA) [2005] 'cosmic vision' [6] identified four major scientific questions designed to motivate future space missions. The four questions are outlined below, and their specific relevance to (FIR) astronomy follows.

1. What are the conditions for life and planetary formation?
2. How does the solar system work?
3. What are the fundamental laws of the universe?
4. How did the universe begin, and what is it made of?

Two of these questions, "What are the conditions for life and planetary formation?" and "How did the universe begin, and what is it made of?" have been identified within the cosmic vision as benefiting from FIR observations of both newly forming stellar systems and the red-shifted light of the oldest galaxies in the universe [6]. Observing these systems comes with many challenges though, and current instrumentation and observational techniques have been pushed to their limits by missions like *Herschel* [7] and the proposed *Space Infrared Telescope for Cosmology and Astrophysics* (SPICA) [8] mission. The cosmic vision confirms that FIR astronomy is considered critical to our understanding of the universe, but observing in these wavelengths often pose technical challenges.

## 1.1 FIR Astronomy

The FIR region is often defined as covering the wavelengths from approximately 30–300 $\mu$m [9] but for the purpose of this thesis the FIR will be considered to extend from 12–350 $\mu$m (the proposed waveband for the SPICA telescope [10]). According to Wien's law [11],

$$\lambda_{Peak} = \frac{2.898 \times 10^{-3}}{T} \quad [\mathrm{m}], \tag{1.1}$$

where $T$ is the temperature of the emitting source. Wien's law implies that objects whose peak emission falls within the FIR will range from approximately 8 K–240 K. This makes the FIR convenient for observing cold regions of the InterStellar Medium (ISM) where star formation is most likely to occur. It also means that FIR astronomers concern themselves with very dim objects, and even the optics with which these objects are viewed may be brighter than the source itself as was the case for *Herschel* [12].

In addition to the cold ISM, FIR observations are important for studying the birth and evolution of galaxies. Approximately half of the energy ever emitted by stars and galaxies lies in the cosmic infrared background [13]. The infrared background light is coming from some of the earliest galaxies to form in the universe and involve significant look-back times. This is not the same as the cosmic microwave background which contains the majority of radiant energy in the universe [13]. The cosmic microwave background is light from the epoch of recombination when electrons and protons first bound into atoms [14], rather than starlight.

The redshift of light is defined as [11]

$$z = \frac{\lambda_{obs} - \lambda_{emit}}{\lambda_{emit}}, \tag{1.2}$$

where $\lambda_{obs}$ and $\lambda_{emit}$ are the observed and emitted wavelengths of a photon. The expansion of space causes shorter wavelength light emitted from very distant sources to be stretched into the FIR band. This makes the infrared background light optimal for studying the chemical evolution of galaxies which peaks at a redshift of z∼1–4 [10]. The fine-structure lines emitted by active galactic nuclei and during star formation are also visible in the FIR and enable the tracking of these phenomena through time. Additionally, both solid (silicates) and gas phase (poly-cyclic aromatic hydrocarbons) chemistry can be observed with FIR observations across a wide range of redshifts enabling astronomers to track the chemical evolution of galaxies [15].

The ability to track physical phenomena across a range of redshifts makes observations in the FIR particularly useful in studying the evolution of those processes in cosmic time. The FIR is also useful for studying smaller scale objects though. Exoplanetary surveys are often performed in the infrared where the contrast between a star and the planets around it is more suppressed than in the visible [15]. Observations in the FIR are also useful in probing the processes of individual star forming regions since stars form in cold molecular clouds which obscure visible light, but glow brightly in the FIR. It is this use of FIR which is most closely tied to the work in this thesis although, as outlined, there are many other important drivers for improving FIR observational data.

### 1.1.1 Challenges of FIR Astronomy

Despite the need for improved observations in the FIR, observing in this waveband presents many challenges. The largest challenge facing FIR astronomers is the opacity of Earth's atmosphere. As can be seen in Figure 1.1, radiation in the FIR band is absorbed by our atmosphere making it impossible to observe in the FIR from the ground. In order to bypass this obstacle observatories are built in high and dry places where the column density of water vapour is low, or on-board high-flying airplanes such as *SOFIA* [16], but the most effective solution is to go above the atmosphere and observe from space. Of course, observing from space introduces many other challenges not associated with ground based observations. *Herschel* was the largest single dish monolithic telescope launched with a 3.5 m diameter primary mirror. This imposes a strict limit on the size of space-borne telescopes, which in turn affects both sensitivity (because of a limit to the light-collecting area) and resolution. FIR telescopes are positioned at what is known as the second Lagrangian point of the Sun-Earth system, $1.5\times10^6$ km away from Earth along the Sun-Earth axis. This distance means that once a telescope is launched there is no way to access the craft and correct any hardware or mechanical errors as was done with the *Hubble* space telescope [17].

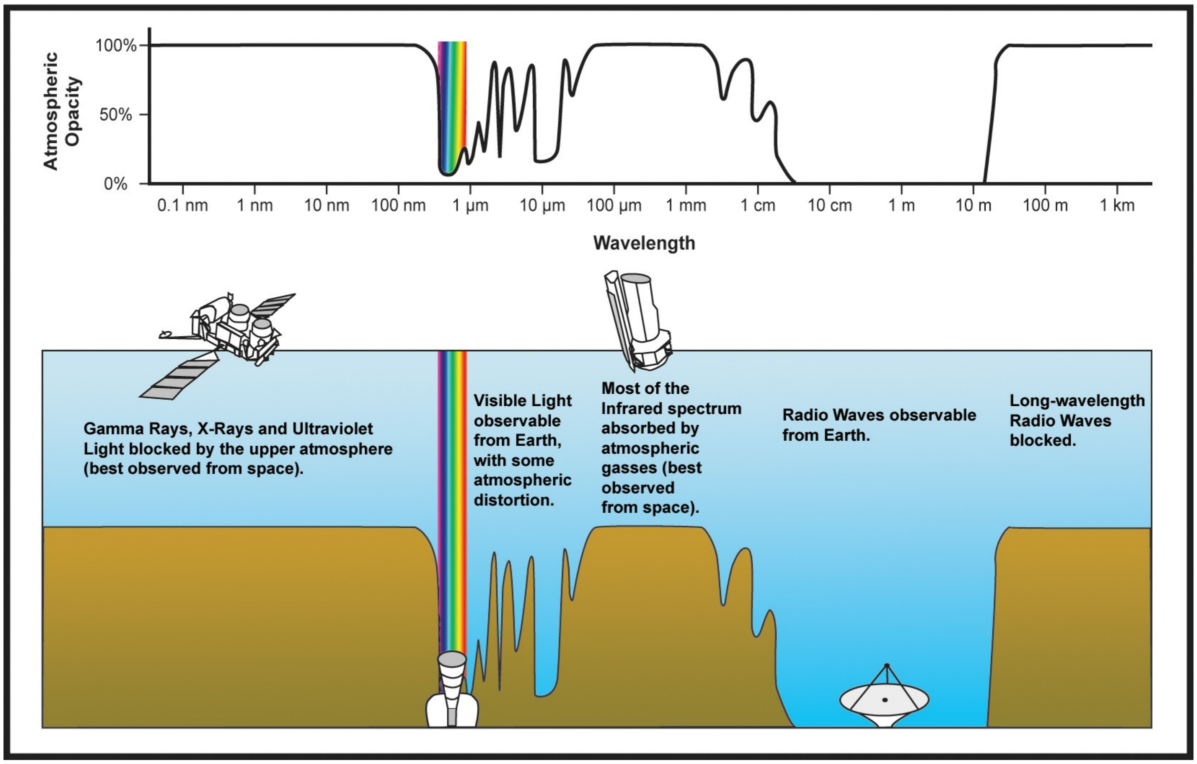

Figure 1.1: Transmission of electromagnetic radiation through the Earth's atmosphere. Though the near infrared has a few windows for observation, nearly all FIR radiation is extincted (absorbed or reflected) before reaching the ground. Figure Source: IPAC [18].

In addition to the challenges posed by atmospheric opacity, FIR photons are relatively low-energy and therefore fundamentally difficult to detect. The energy of a photon is [11]

$$E = h\nu = \frac{hc}{\lambda} \quad [\mathrm{J}], \tag{1.3}$$

where $h$ is Planck's constant, $\nu$ is the frequency of the light, and $\lambda$ is the wavelength. The long wavelengths of the FIR correspond to shorter frequencies and lower energies. The small amount of energy carried by FIR photons necessitates very sensitive equipment in order to be detected.

Photons in the FIR are also produced in great quantity by thermal radiation from optical components if they are warmer than ~10 K. This means that dimmer signals of distant sources may not be detectable above the noise-floor and important information may be obscured by thermal emission in the optics. Finding a means to mitigate these effects will allow the next generation of FIR observations to probe structures and systems which are currently undetected at these wavelengths.

### 1.1.2 Overcoming the Challenge

The future of FIR astronomy will depend on two major advancements in the field, increased sensitivity combined with cryogenically cooled optics for reduced background emission, and an improvement in spatial resolution. Sensitivity can be improved by an increased aperture size, or by a reduction in the noise floor which enables fainter signals to become more prominent. For observations in the FIR, thermal radiation from the optics may be a significant source of noise, and cryogenic cooling of the optics can help to reduce the thermal background. The need to cool optics has meant previous observers have been forced to choose between a large, or a cold, primary optic, trading spatial resolution for a reduced noise floor.

Table 1.1 lists some of the most famous IR telescopes in chronological order, continuing to the proposed JWST and SPICA telescopes. It can be seen that broadly speaking previous telescopes were either very cold (IRAS, COBE, ISO, Spitzer, Akari) or large (*Herschel*, *Planck*, WMAP). The SPICA telescope is proposed to be a large and cold telescope, with a 2.5 m primary mirror actively cooled to ~8 K. The cooled optics mean it will be a factor of $10^3$ more sensitive than *Herschel* or *Spitzer* [10]. Cooling materials to cryogenic temperatures (sometimes classified as $< 123$ K [30], the term ‘cryogenics’ will be used in this work to refer to temperatures $\lesssim 10$ K) comes with a number of challenges though, as the characteristics of their temperature-dependent physical properties are altered.

Table 1.1: List of infrared space telescopes sorted chronologically.

| Name | Waveband [$\mu$m] | Primary Aperture [m] | Primary Mirror Temperature [K] | Date of Launch | Mission End Date |
|---|---|---|---|---|---|
| IRAS [19] | 8–120 | 0.57 | $<10$ | January 25, 1983 | November 22, 1983 |
| COBE [20] | 1.2–10000 | 0.19 | $<1.8$ | November 18, 1989 | December 23, 1993 |
| ISO [21] | 2.5–240 | 0.6 | $\sim 3$ | November 17, 1995 | April 8, 1998 |
| WMAP [22] | 22–90 | 1.5 | $\sim 90$ | June 30, 2001 | October 28, 2010 |
| Spitzer [23] | 3.6–160 | 0.85 | 5.5 | August 25, 2003 | Continuing Observation |
| Akari [24] | 2–180 | 0.71 | 5.8 | February 22, 2006 | November 24, 2011 |
| WISE [25] | 3.4–22 | 0.4 | $<12$ | December 14, 2009 | Continuing Observation |
| Herschel [26] | 55–672 | 3.5 | $\sim 85$ | May 14, 2009 | April 29, 2013 |
| Planck [27, 28] | 300–11000 | 1.5 | $\sim 50$ | May 14, 2009 | October 23, 2013 |
| JWST [29] | 0.6–29 | 6.6 | 50 | $2021^*$ | $2026–2031^\dagger$ |
| SPICA [10] | 12–350 | 2.5 | $<8$ | $2032^*$ | $2035–2037^\dagger$ |

$^*$ Anticipated Launch Date

$^\dagger$ Estimated based on projections of mission duration

Though SPICA would represent a significant improvement over previous telescopes, the spatial resolution of SPICA is still too poor to resolve even the nearest solar system sized objects ($<0.2$ arcseconds [31]) outside of our own solar system. For a single-dish telescope the Rayleigh criterion states that the minimum angular separation between two distinguishable points is proportional to the wavelength of light, $\lambda$, and inversely proportional to the diameter of the telescope, $D$, as [32]

$$\Delta\theta = \frac{1.22\lambda}{D} \quad \text{[radians]}. \tag{1.4}$$

Thus working at long wavelengths requires large optics for high spatial resolution, and highlights the desire for large diameter telescopes. *Herschel* was the largest single-dish telescope launched thus far with a primary aperture of diameter 3.5 m. Any telescope larger than 3.5 m must either be launched in multiple pieces and constructed in space, or use a folding, segmented mechanism like the *James Webb Space Telescope* (JWST). These methods both come with a number of other technical challenges, and still limit the size of the aperture to a couple of meters. For instance, the JWST is proposed to have a 6.6 m diameter aperture [29], less than a factor of 2 greater than *Herschel*. Consider that for the longest wavelengths of the FIR ($\sim$350 $\mu$m) the telescope diameter would need to be $\sim$435 m to achieve the spatial resolution required to image distant solar-system sized objects.

Spatial resolution may also be improved by spatial interferometry which simulates the resolution of a larger aperture by scanning smaller dishes over a baseline of length $B$. Unlike the construction of an aperture in space, the theoretical size of an interferometer is unbounded, and improves spatial resolution by a factor of $\frac{B}{D}$ [33]. Long baseline interferometry is the best chance at achieving the spatial resolution desired at FIR wavelengths and it has already been used successfully at other wavelengths in ground-based arrays, but to implement the technique in space would come with a host of technical challenges.

Spatial interferometry uses the interference from different points on a coherent wavefront to reconstruct the intensity distribution of the source, and relies on precise measurements of both time and position for signals from each of the collecting dishes. For a space-bound interferometer there are a few primary proposals: free-flying telescopes, telescopes bound by a tether [34], or dishes which move along a rigid mechanical structure [35].

The uncertainty in relative position of two observing dishes must be smaller than the wavelength of light under study. For the shortest wavelengths in the FIR this tells us that the uncertainty in relative position should be less than a few microns over a baseline of hundreds of meters. This amounts to $\sim 10^{-8}$ relative uncertainty at the longest baseline, and that level of variance could be caused by thermal gradients, bending, or twisting in the baseline material. To successfully perform spatial interferometry in space requires precision monitoring of relative position, and an intimate knowledge of the cryogenic material properties of the constituents of the baseline and individual observing dishes.

For the next generation of FIR astronomical observations, long baseline interferometry is the best method for achieving the spatial resolution required. In order to preserve the visibility of spatial fringes the surface smoothness must be known to sub-wavelength precision [36]. One must also know the relative position of receivers, which may be accomplished with laser position metrology systems with nanometer precision. Additionally, thermal modeling of composite materials for spacecraft must be robust enough to develop predictive models. The advent of long baseline interferometry will help FIR astronomers to answer fundamental questions about star formation, and the evolution of galaxies in the early universe just as the Atacama large millimeter array (ALMA) [37] has done over narrow spectral bands visible from the ground.

## 1.2 Thesis Overview

This thesis will focus on some of the outlined techniques and technologies for improving astronomical observations in the FIR waveband. Chapter two is an introduction to star-formation theory, with an emphasis on the process by which an individual star comes to form and the influence it has on the surrounding nebula. A discussion on the important physical differences between high-mass and low-mass stars and their relative number densities will follow. Chapter two concludes by introducing extended green objects (EGOs) as an example of massive star-forming regions and a demonstration of the difficulty in understanding source behaviour using current observational data.

Chapter three will cover the characterization of two metrology systems used in experimentation, allowing the determination of the approximate uncertainty of the two systems. There will be particular emphasis on a custom-built three-phase laser metrology system. The three-phase metrology system is used in comparison with an Aerotech ALS20045 linear translation stage [38], and a Renishaw RLU10 laser unit with an RLD10 differential laser interferometer and detector head [39], hereafter referred to solely as the 'Aerotech' and the 'Renishaw', respectively. The Renishaw data are used to profile both the metrology system, and the stage. This chapter will conclude with an introduction to a prototype of a frequency modulated laser metrology system which has yielded promising preliminary results on the thermal contraction of aluminium and carbon fibre reinforced composite materials.

The profiling of cryogenic properties of composite materials may be important for ensuring predictable material and instrument behaviour in future missions. Chapter four covers the means by which thermal energy is stored and transported in solid-state materials like copper and aluminium. The utility of composite materials for space-borne instrumentation will be discussed, and methods for profiling the thermal conductance and the coefficient of thermal expansion (CTE) will be considered. Attempts to profile these particular thermal properties of carbon-fibre reinforced polymers (CFRP) composites will be presented with a discussion on the benefits and drawbacks of different methods of measurement.

The designs for a number of apparati used in cryogenic testing are presented in Chapter 4, and the results of manufacturing are shown where relevant. Limitations on the utility of each of the designs are explored, and a final design for a comprehensive experimental setup is presented. Thermal conduction of the final design is included to approximate cool-down time, and will conclude the chapter.

The thesis will finish with chapter five, a summary of the results thus far and a list of suggested improvements to the experiments performed. Suggestions for improving the methods used in calibration of the two laser metrology systems to measure thermal contraction at cryogenic temperatures will also be included. For aspects of the work presented the task of performing more experiments and collecting conclusive data is still unfinished, and though the experimental framework is largely in place, there was insufficient time to finalize and manufacture the apparatus for cryogenic testing of material properties presented in this work. The progress towards dedicated cryogenic materials testing infrastructure is presented, along with technical drawings for a prototype in Appendix C.

# Chapter 2

# Investigating Star Formation

Stars have been described as the "atoms" of the universe due to their fundamental role in determining its structure and evolution [40, 41]. The creation and distribution of stars throughout the universe informs astronomers about the formation, structure, and evolution of galaxies. Stars are responsible for the creation of all heavy elements (atomic mass greater than helium) except for trace amounts of lithium [14], including many of the elements necessary for life on earth. These heavier elements are created by nuclear fusion in the center of stars and expelled in supernovae, enriching the surrounding ISM with heavy elements and helping to trigger further star formation. Planet formation and questions of extra-terrestrial life are also linked to the process of star formation as planets form in the accretion disks of new stars [42]. Stars are also efficient generators of entropy, and as a consequence the distribution of stars in the universe is an important factor for cosmologists interested in the thermodynamic evolution of the universe [42].

This chapter will cover the basic principles of star formation with the specific goal of motivating improvements to current observational techniques. The conditions by which a star comes to form will be explored followed by examples of observable tracers of these mechanisms such as line emission from atomic, ionic, and molecular species. The interactions between a newly-formed star with the surrounding ISM will be considered, and the physical theory will predict some observable tracers. Once predictions from theory have been established, an example of a known star-forming region will be considered. The observations of this region will be compared and contrasted against the predictions from theory. When theory and observation disagree it will be used to discuss inadequacies of theory, and the ways in which observational data collection may be improved.

## 2.1 General Star Formation

McKee & Ostriker [40] wrote a review on star formation in 2007, and suggest the study of star formation should be split into “macrophysics” and “microphysics”. Macrophysical studies focuses on the larger scale formation of stars within giant molecular clouds, addressing questions about the rate of star formation within clouds and galaxies and the mass distribution of forming stars (i.e. how many stars of a given mass are produced). Microphysics by contrast focuses on the formation of individual stars and binaries and the mechanisms by which these systems accrete mass and dissipate energy. Although it is important to understand the physics on both scales, the theory presented will have an emphasis on microphysical processes.

### 2.1.1 Macrophysics

Macrophysical studies are most important for understanding the chemical evolution of galaxies and the universe as they look at larger scale structures [8]. One of the most important macrophysical aspects of star formation is the initial mass function (IMF) which measures the mass distribution of newly-formed stars and is defined by [42]

$$\Delta S \phi(M) dM = \mathcal{N}_M dM. \tag{2.1}$$

In Equation 2.1 $\phi(M)$ is the IMF with units of $M_\odot^{-2}$, $\mathcal{N}_M dM$ is the number of new stars in the mass interval $(M,\ M + dM)$, and $\Delta S$ is the total amount of mass in units of $M_\odot$ within the given star-forming region used in creating new stars [42]. The IMF is normalized according to [42]

$$\int_{M_{min}}^{M_{max}} \phi(M) M dM = 1, \tag{2.2}$$

such that the product of $\phi(M)M$ gives the fraction of $\Delta S$ used to create stars in the interval $(M,\, M + dM)$. The IMF was first derived by Salpeter when he fit a power law for masses between $0.4\,\mathrm{M}_\odot$ and $10\,\mathrm{M}_\odot$ finding the relationship [42]

$$\phi(M)dM \approxeq KM^{-2.35}dM, \tag{2.3}$$

with $K$ a constant related to the total star formation rate [42]. Salpeter derived the empirical relationship in Equation 2.3 more than 60 years ago, and current observational data have shown that the IMF is best-fitted with a piece-wise function, though the same functional form is used. The IMF is an important facet of macrophysical star formation, and is part of what enables astronomers to track the chemical evolution of galaxies and the universe. The mass of a star is related to the elements it will be capable of creating, and the timescale of the life of the star which in turn dictates how quickly those elements are recycled back into the surrounding interstellar space. The distribution of stellar masses therefore predicts the relative abundance of heavy elements, as well as the rate at which heavier elements are recycled in star formation. To understand these aspects of star formation however, requires a narrowing of focus from the macro to the micro.

### 2.1.2 Microphysics

The life-cycle of a star depends a great deal on the cloud from which it is formed, particularly on how much mass the star accumulates. The most massive stars will live for approximately $3 \times 10^6$ years and stars with mass $M < 10\,M_\odot$ have lifespans which approximately obey $t \approx 10^{10} \left(\frac{M}{M_\odot}\right)^{-2.35}$ years [43] with some stars having nearly the same age as the universe itself [44]. In addition to the disparity in lifespan amongst stars of different masses the physical processes undergone by stars during their lives and deaths are dominated by their mass. Massive stars are capable of fusing elements heavier than carbon, and produce stronger radiation fields which affect the ionization structure of the surrounding ISM differently than radiation produced by a lower-mass star. The additional radiative pressure may also prevent further mass accretion, making it more challenging for massive stars to form [45, 46]. Massive stars are also capable of ending their lives as supernovae, which enrich the ISM with heavy elements [47]. As shown by the $M^{-2.35}$ relation in Equation 2.3, massive stars are also considerably less likely to form than lower-mass stars, and combining this with their comparatively short lifespans means massive stars are much less common.

Explaining the differences in life-cycle for stars of different masses requires more rigorous models of star formation. The relatively long timescales over which stars are formed make it impossible for astronomers to monitor the development of any individual source. Dynamic observations of an individual source are untenable so detailed observations of separate but comparable sources at each stage of their evolution are needed in order to develop more comprehensive models of star formation. Classifying objects based on their evolutionary stage enables the development of a chronology without dynamic monitoring of a single source. The current understanding of star formation was laid out in a Shu et al. 1987 paper titled "*Star Formation in Molecular Clouds: Observation and Theory*" [48] and involves four stages.

1. Pre-stellar cores form within dense regions of molecular clouds after losing turbulent and magnetic support.
2. A protostar with a surrounding nebular disk forms within the collapsing cloud.
3. A stellar wind breaks out along the rotational axis of the system creating a bipolar outflow.
4. The cloud collapse ends and the surrounding material is blown away leaving the newly formed star with a circumstellar disk.

These four stages are represented graphically in Figure 2.1 in panels (b) through (e) along with the approximate time scales, length scales, and emission spectra for each stage. Though this theory has been expanded, the underlying principles remain the same.

The theory posits that stars are created when clouds of dust and molecular gas collapse under their own gravity and the pressure, temperature, and density are high enough to

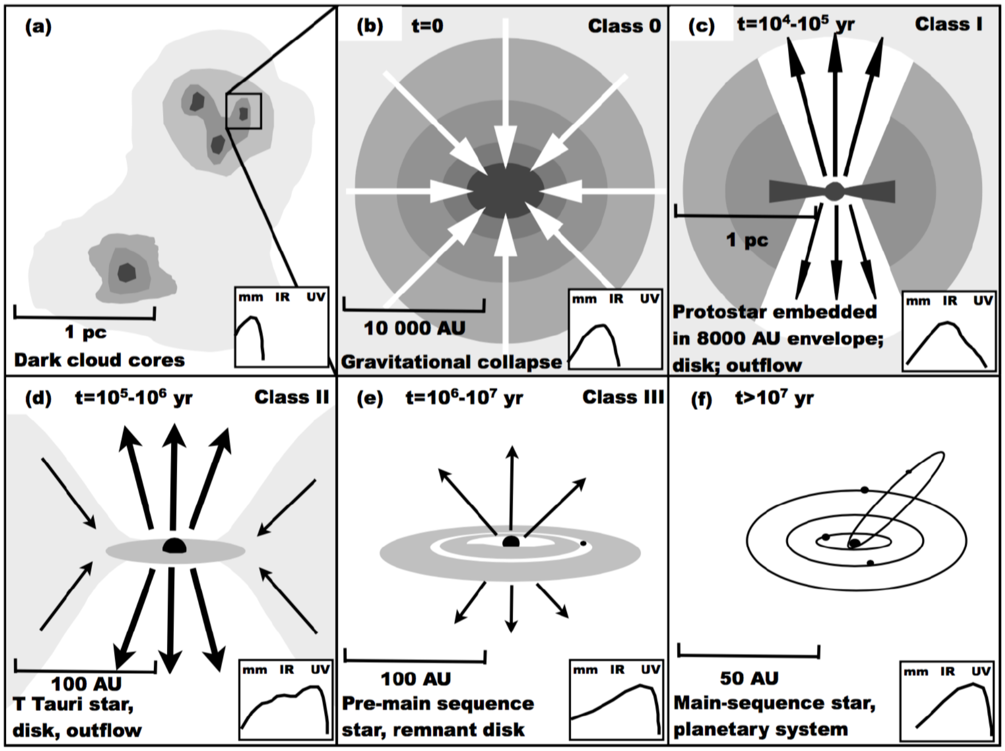

Figure 2.1: Diagramatic representation of the stages of star formation. Note that each stage is estimated to last approximately ten times longer than the previous. The class of protostar is determined based on the slope of the spectral energy distribution. Figure Source: Makiwa [49], originally from Jonkheid [50].

trigger nuclear fusion. The primary barrier to this condition being satisfied is the thermal pressure supporting the cloud against self-gravity. Though there are many other important effects such as magnetic fields and turbulence, they are often non-linear effects which are difficult to model. Assuming that only the thermal pressure balances self-gravity a spherical cloud will collapse to form a star if it exceeds the Jean's mass [11],

$$M_J = \left(\frac{5k_BT}{Gm}\right)^{3/2}\left(\frac{3}{4\pi\rho}\right)^{1/2} \quad [\mathrm{kg}], \tag{2.4}$$

where $\rho$ is the density, $G$ the gravitational constant, and $k_B$ is the Boltzmann constant. Equation 2.4 shows that the mass required to form a star is minimized where the temperature is cold, and the density is high (it also depends on the mass of the particle, $m$, but we can assume $m \approx m_{H_2}$). This model of star formation is helpful as a first-order approximation, however it is known that the process of star formation is far more chaotic than the situation assumed above. Incorporating other effects like magnetism, turbulence, density gradients, or changes in geometry quickly complicates models and observational data are needed for comparison to theory. The best place to seek observational data for constraining models is in the cold dense clouds of the ISM, and the wavelengths best suited for investigating these sources fall in the FIR.

The need for detailed observations of objects at every stage of formation demands that relevant sources are identified for each stage, and that they are probed very thoroughly. Since stars form within clouds of dust and gas it is often not possible to identify whether star formation is taking place except by looking for other tracers of star formation such as in-falling gas and dust and ensuring that the theories linking such tracers to star formation are valid. For stellar objects in the earliest stages of their life-cycle the sources are still embedded in clouds of cold dust and gas and it is important to look for the tracers of mechanisms which facilitate cooling of the cloud.

## 2.2 Cooling of Interstellar Clouds

Before a cloud can collapse to form a star it must cool enough that the Jean's mass is met by the matter in the cloud. Interstellar clouds are extremely poor at conducting and convecting heat so the primary mechanism for heat transfer is radiation. An interstellar cloud can cool by many mechanisms but the most effective is when energy levels are excited by inelastic collisions, and de-excited by radiation [43, 46, 51]. This process converts kinetic energy to radiation, and when the radiation leaves the cloud the thermal energy is lost. This reaction is described by Equations 2.5 and 2.6 below [51],

$$A + B \rightarrow A + B*, \tag{2.5}$$

$$B* \rightarrow B + \gamma, \tag{2.6}$$

where $A$ and $B$ are two collisional partners and $B*$ indicates a higher excitation state of $B$. The cooling rate is determined by the probability of the collisional excitation resulting in emission of a photon that will escape the cloud, and the energy of that escaped photon. The cooling rate of a cloud and the primary mechanism by which a cloud cools are themselves temperature dependent. Towards lower temperatures the average kinetic energies are lower and are only able to excite lower energy transitions, making them less efficient at dissipating energy. As higher-energy interactions freeze out only the lowest-energy reactions will be able to cool clouds to the point of collapse.

A transition is considered to be most effective at cooling when it satisfies the following criteria [46]:

1. frequent collisional excitation,
2. excitation energy less than the average thermal energy,
3. collisional quenching is not a problem,
4. emitted photons escape the cloud.

If these conditions are satisfied then energy is frequently transferred from kinetic to potential (1 & 2), it is then transferred to radiative energy rather than transferred back to kinetic energy (3), and the radiative energy is able to escape the cloud (4). If all these criteria are satisfied then the mechanism is an efficient coolant.

As is shown by Equation 2.4, the methods by which interstellar clouds are cooled determine in great part whether the cloud will collapse at all. Understanding the transitions by which an interstellar cloud dissipates its thermal energy is important for understanding star formation. A few of the most common transitions will be discussed from highest interaction energy to lowest, thereby following the dominant mechanisms towards cooler temperatures. This will conclude by considering the lowest-energy interactions which can still be excited at the low temperatures most easily viewed in the FIR.

### 2.2.1 Cooling by Ionic Transitions

For hotter clouds with higher kinetic energies the dominant mechanism will be emission from ions and atoms. In order for condition (1) to be satisfied both the species of interest and its collisional partner (normally electrons) are needed in large quantity. This means that the most likely candidates will be some of the most abundant atoms including carbon, nitrogen, oxygen, and their ions. Though hydrogen is far more abundant than any other element, it suffers from self-absorption and violates condition (4) [46]. At temperatures typical of a diffuse cloud ($\sim$100 K) condition (2) tells us that the relevant transitions should have excitation energies below the temperature given by [46]

$$T = \frac{h\nu}{k_B} = \frac{hc}{\lambda k_B} \quad [\mathrm{K}]. \tag{2.7}$$

Rearranging the equation to solve for wavelength at 100 K we find that $\lambda = \frac{hc}{k_B T} = 1.439 \times 10^{-4}$ m. This result implies transitions with wavelengths longer than 144 $\mu$m will satisfy condition (2) for a typical interstellar cloud. Table 2.1 lists a number of common ions and transitions which act as coolants in interstellar clouds. An atom with a single roman numeral next to it denotes a neutral atom (e.g. NI is neutral nitrogen). Any number greater than one is an additional ionization (e.g. OIV is triply ionized oxygen). Due to the abundance of carbon, nitrogen, and oxygen they can act as important coolants and the transitions listed demonstrate their ability to cool even at the low temperatures corresponding to emission in the FIR. The superscripted number in the transition denotes the multiplicity, equal to $2s$+1, where $s$ is the spin quantum number. The letter is indicative of the orbital angular quantum number, $l$, with $l = 0, 1, 2, 3, 4...$ corresponding to the letters $S, P, D, F, G$ and so on alphabetically. The subscripted number denotes the total angular momentum and may take on values between $|l_1$ - $l_2|$ and $|l_1$+$l_2|$ [52] While the species listed in Table 2.1 are important coolants due to their relatively high abundance, there are other less abundant elements like neon, magnesium, silicon, sulfur, and argon which also contribute to cooling [51].

Table 2.1: List of some common ionic and atomic transitions in decreasing order of energy. Each of these transitions falls in the FIR. The effective temperature of the line is included as an indication of when the line ceases to be an effective cooling mechanism. Data acquired from Splatalogue [53].

| Species | Transition | Wavelength [$\mu$m] | Effective Temperature [K] |
|---|---|---|---|
| OIII | $^3P_2$–$^3P_1$ | 51.81 | 278 |
| OIII | $^3P_1$–$^3P_0$ | 88.36 | 163 |
| NII | $^3P_2$–$^3P_1$ | 121.9 | 118 |
| CII | $^2P_{3/2}$–$^2P_{1/2}$ | 157.7 | 92 |
| NII | $^3P_1$–$^3P_0$ | 205 | 70 |
| CI | $^3P_2$–$^3P_1$ | 370.4 | 39 |
| CI | $^3P_1$–$^3P_0$ | 609.1 | 24 |

As the cloud cools to $<$100 K the dominant mechanism for cooling changes from atomic and ionic transitions to rotational transitions in molecules, particularly carbon monoxide due to its abundance.

### 2.2.2 Cooling by Rotational Molecular Transitions

Rotational transitions in linear molecules like CO are relatively low energy phenomena, for instance the CO(1–0) transition has an effective temperature of 5.5K. These extremely low excitation temperatures mean that the transitions may be collisionally excited at temperatures of $\sim$10K. This quality ensures that CO satisfies the first two criteria of an effective coolant.

The large abundance of CO which makes it an efficient cooler may, however, result in a violation of the third and fourth criteria if the density is too high. Self-absorption is a common problem with CO and violates criterion (4) as the radiation which carries energy out of the cloud is re-absorbed and not able to dissipate the energy efficiently. If the density of CO is too high the lines may also become collisionally quenched. In quenching the excited states are de-excited by collisions, and transfer their energy back into the thermal energy of the cloud. Collisional quenching is an explicit violation of criterion (3), and paired with self-absorption strongly limits the cooling capacity of regions with CO in very high densities.

Under these conditions less common molecules like water and hydroxide may become more important for cooling despite their under-abundance [46]. It's also possible for isotopologues of CO, particularly $^{13}$CO to act as effective coolants. This is demonstrated in Figure 2.2. The maps show the temperatures and densities of both $^{12}$CO and $^{13}$CO in three sources believed to represent massive star forming regions which are discussed further in Section 2.6. The temperature of the clouds are measured to be different by the two species because of self-absorption in lines of $^{12}$CO. The column density of $^{12}$CO is high enough that self-absorption is a significant problem so the light seen is radiating from the edge of the cloud whereas the emission from $^{13}$CO is probing deeper into the cloud where temperatures are higher.

One might reasonably expect that the densities would also be higher towards the center of the cloud. Using the solar ratio of $^{12}$CO to $^{13}$CO of 100:1 [56], the $^{13}$CO density is relatively high in the sources shown in Figure 2.2. This is further evidence that the $^{13}$CO lines probe deeper into the cloud, and that self-absorption is problematic for $^{12}$CO lines, reducing their efficiency as coolants in these sources.

Once a given cloud has cooled enough for core collapse and the onset of nuclear fusion the star enters a new evolutionary phase and the physics changes accordingly.

## 2.3 Heating of Interstellar Clouds

Once nuclear fusion has begun the cloud of dust and gas is largely blown away and the temperature of the remaining material increases as high-energy photons are generated and reheat the surrounding interstellar medium [51]. Assuming that a star is 'switched on' instantaneously, certain conclusions about the interaction of the newly produced stellar radiation and the surrounding cocoon of dust and gas may be inferred.

Perhaps the most obvious effect of stellar radiation on the surrounding environment will be to heat the previously cold cloud [51]. A star with spectral type O-B can be expected to radiate as a blackbody with temperature on the order of $2\times10^4$ to $6\times10^4$ K [46] and the cloud from which a star of this type is formed is typically approximately 100 K. The high-energy

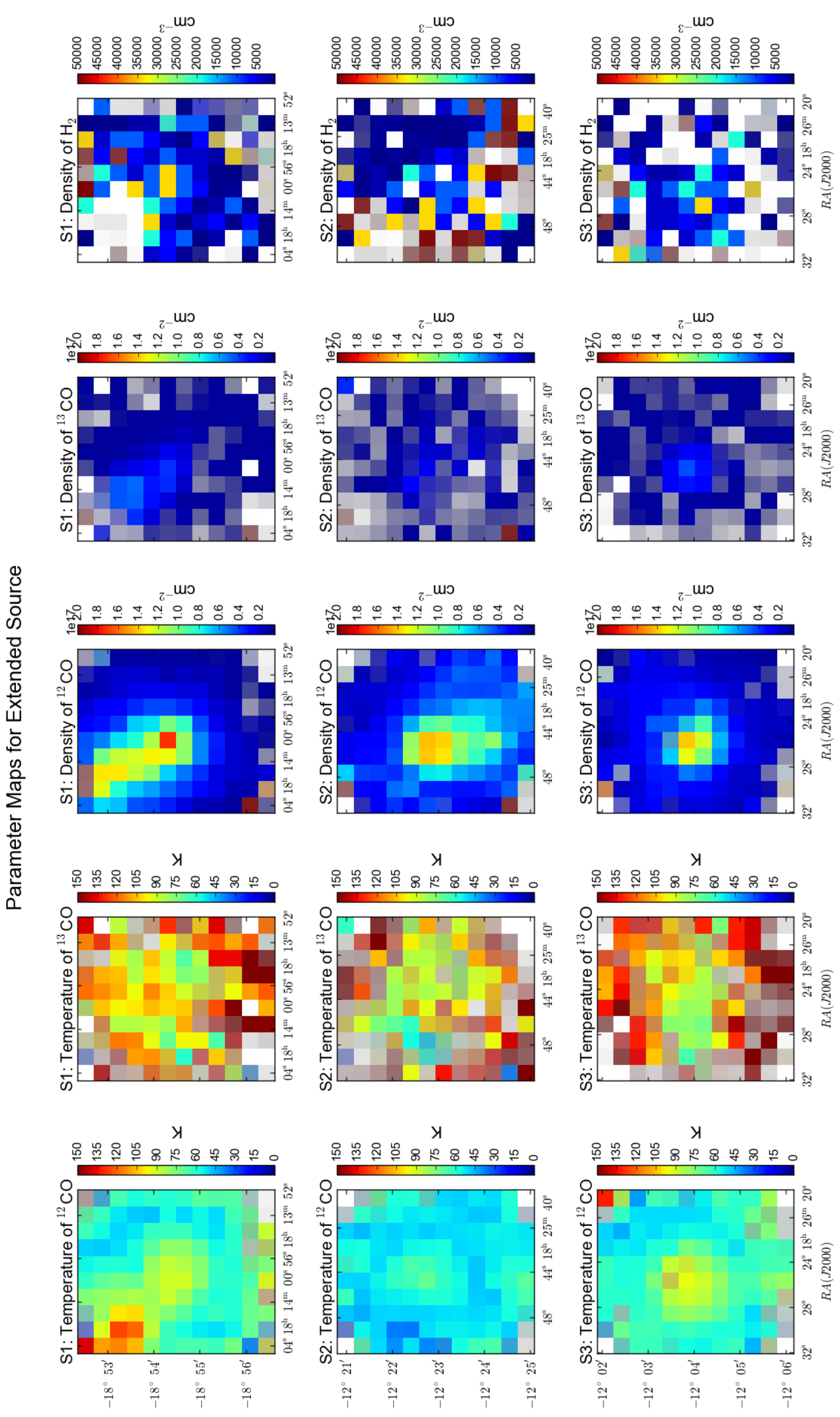

Figure 2.2: Temperatures and column density of both $^{12}$CO and $^{13}$CO towards the star forming region G11.92-0.61. Temperatures and densities found using the rotation diagram method [54]. Densities of H$_2$ found using Radex modeling software [55]. Data are masked based on signal-to-noise ratio (SNR), the opacity is a linear gradient from transparent at SNR of ≤1 to opaque for SNR ≥5.

photons produced by the new star will ionize the surrounding region, and in doing so it will raise the temperature.

Each time a photo-ionization takes place the reaction goes as [51],

$$A + \gamma \rightarrow A^{+} + e^{-}, \tag{2.8}$$

where $A$ is an atom, $\gamma$ the ionizing photon, and $e$ is the liberated electron. The electron released in the right hand side of Equation 2.8 will have kinetic energy equal to the difference between photon energy, $h\nu$, and the ionization potential, $I$, of $A$. This kinetic energy is then shared with the rest of the cloud by elastic collisions increasing the thermal energy of the cloud by $(I - h\nu)$.

To quantify the amount of heat imparted by photo-ionizations let us first take the simplest case of a nebula in ionization equilibrium and consisting of purely hydrogen gas. Though this model is not truly representative, including additional species severely complicates the balance equations. Ionization equilibrium is defined as a balance between ionizations and recombinations of the gas and is described as [51]:

$$n_H \int_{\nu_0}^{\infty} \frac{4\pi J_\nu}{h\nu} a_\nu d\nu = n_e n_p \alpha_a(T) \quad [\mathrm{m}^{-3}\mathrm{s}^{-1}]. \tag{2.9}$$

The left hand side of Equation 2.9 is the time rate per unit volume of ionizations, where $n_H$ is the number density of neutral hydrogen, $a_\nu$ is the frequency-dependent cross-section for ionization, and $J_\nu$ is the mean intensity of radiation, which has units of $\frac{W}{m^2 sr Hz} \equiv \frac{J}{m^2 sr}$. The right hand side is the time rate of recombinations per unit volume where $n_e$ and $n_p$ are the number densities of electrons and protons respectively, and $\alpha_a(T)$ is the cross-section for recombination to all levels given by [51]

$$\alpha_a(T) = \sum_{n} \sum_{L=0}^{n-1} \alpha_{nL}(T) \quad [\mathrm{m}^{-3}\mathrm{s}^{-1}], \tag{2.10}$$

where $n$ and $L$ represent the quantum levels. For simplicity we will let the mean radiation field be equal to the blackbody spectrum of the star, $J_\nu{=}B_\nu(T_*)$.

Now let us consider the amount of heat imparted to the cloud by ionization events. The amount of kinetic energy produced by a single ionization event is $E = h(\nu{-}\nu_0)$, and therefore the kinetic energy created across all ionization events will be given by the expression [51]

$$G(H) = n_H \int_{\nu_0}^{\infty} \frac{4\pi J_\nu}{h\nu} h\left(\nu - \nu_0\right) a_\nu d\nu \quad [\mathrm{Jm^{-3}s^{-1}}], \tag{2.11}$$

where $G(H)$ is the kinetic energy gained by the cloud per unit volume every second due to ionization of hydrogen. Equation 2.11 is very similar to the left hand side of Equation 2.9. If the latter is solved in terms of $n_H$ and substituted into the former the result is [51]

$$G(H) = n_e n_p \alpha_a(T) \frac{\int_{\nu_0}^{\infty} \frac{J_\nu}{h\nu} h\left(\nu - \nu_0\right) a_\nu(H) d\nu}{\int_{\nu_0}^{\infty} \frac{J_\nu}{h\nu} a_\nu(H) d\nu} = n_e n_p \alpha_a(T) \frac{3}{2} k_B T \quad [\mathrm{Jm^{-3}s^{-1}}]. \tag{2.12}$$

The quotient of integrals yields the average energy per liberated electron, and this is equal to $\frac{3}{2}k_B T$ where $T$ is the temperature of the electron before it has the opportunity to thermalize with the surrounding material. In the case where the mean radiation field is equal to the blackbody of the star $T \approx T_*$. This yields a simple expression for the heat imparted by photo-ionization events in terms of densities and stellar temperature.

Assuming that the nebula consists of purely atomic hydrogen the number of protons will be exactly equal to the number of electrons and we can substitute $n_e = n_p$ to find the heating from ionizations to be [51]

$$G(H) = n_e^2 \alpha_a(T) \frac{3}{2} k_B T_* \quad [\mathrm{Jm^{-3}s^{-1}}]. \tag{2.13}$$

Other forms of heating may occur, such as ionization from cosmic rays, or x-ray radiation from external sources. This ionization behave in much the same way, liberating electrons with a finite kinetic energy that is then shared amongst the cloud, and it shall be assumed that this contribution is implicitly included in Equation 2.13. It is also speculated that dust grains may be an important heat source, but this is primarily relevant in diffuse neutral clouds rather than the dense ionized regions surrounding a newly formed star.

## 2.4 Ionization Structure of Stellar Nebulae

A less intuitive change in the physics of a cloud after a newly formed star has switched on is the change in state of the surrounding matter due to the injection of large numbers of high-energy photons. The fusion reactions which take place inside a newly formed star generate a great deal of energy, so much so that any molecules close to the core will be photo-dissociated. Following dissociation of molecules most of the atoms close to the core will become ionized. The physical size of the cloud of ionized gas will depend on the ionization potential of the species, the cross-section for interaction with ionizing photons, and the density of the species. This phenomenon is referred to as ‘ionization stratification’ [46] and its characterization tells astronomers a great deal about the stellar object within the cloud.

Take the example of a cloud consisting solely of hydrogen which will have the simplest possible ionization structure. Any photons with energy greater than 13.6eV, the ionization potential of hydrogen, are going to be absorbed in ionization reactions of the form [46]

$$H + \gamma \rightleftharpoons p^{+} + e^{-}. \tag{2.14}$$

Any photons which have energies less than the ionization potential will eventually escape the cloud because even if they are capable of exciting atomic energy levels below the ionization potential, the de-excitation will occur by cascading down through the energy levels. This cascade produces the Balmer and Lymann series lines [57] and these lower energy photons pass relatively unimpeded through the rest of the gas.

Electrons liberated in ionization events will also recombine with protons, and the recombination will result in one of two situations. Either the recombination will be to the ground level, and produce another ionizing photon, or it will recombine to an excited state. In the event that the recombination is to the ground state, and an ionizing photon is produced we may make the 'on the spot' approximation [51]. The 'on the spot' approximation assumes the photon immediately ionizes another hydrogen atom nearby and allows the recombinations to the ground state to be neglected. Alternatively, the electron will be trapped into a state above the ground level, and the cascade will again produce a series of lines with lower energies capable of escaping the cloud.

When there is balance between the rate of production of ionizing photons by the star and the recombination rate of protons and electrons in the surrounding nebula it is called the equilibrium ionization rate. Let us assume the production rate of ionizing radiation is approximately constant and the medium is of uniform density. Then let us assume that each ionizing photon will produce one ionization event before the energy is dissipated by lower energy transitions. In this simple case the geometric dilution of radiation is the sole factor in determining the size of the ionized region.

The rate at which ionizing radiation is produced will be determined by the temperature, and radius of the star. Assuming that a star emits as a blackbody at a temperature typical of an O-B spectral type star (the hottest classification of stars [58]) with $T_*$=40000 K and radius=12.5 $R_{Sun}$, one can determine the number of photons emitted at each frequency. By integrating all photons with an energy greater than or equal to the ionization potential of hydrogen it is possible to determine a constant rate of production of ionizing photons.

The blackbody curve in Figure 2.3 is an expression of power emitted per unit area per unit solid angle per frequency as a function of frequency. Some important adjustments are needed to convert from the blackbody curve to a number of photons. The blackbody function is divided by solid angle and in order to account for the isotropy of radiation the blackbody curve is multiplied by $4\pi$ steradians. The blackbody is also an area-dependent curve so one must account for the surface area of the emitting source. If the star is considered to be spherically symmetric the area is simply, $A = 4\pi R_*^2$. Finally one must convert from energy

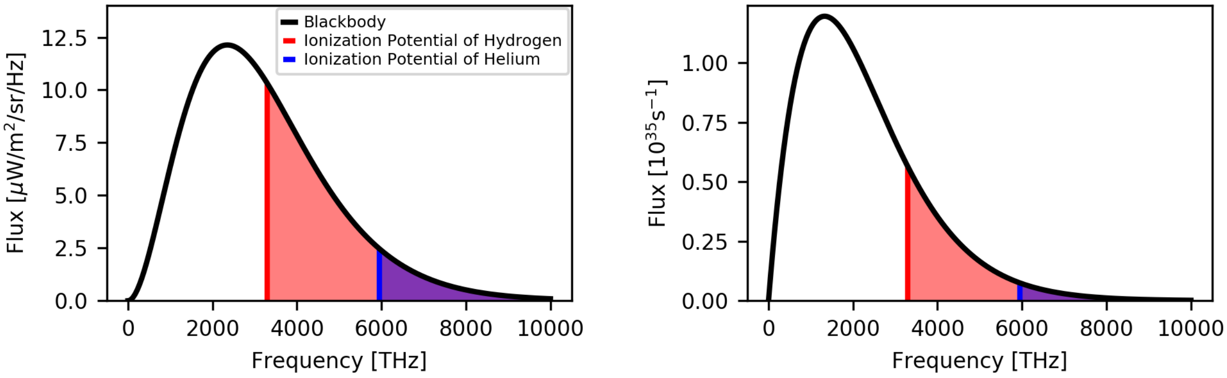

(a) (b)

Figure 2.3: Photon creation by a new star. (a) A typical blackbody curve for a star of temperature $4\times10^4$ K and radius $12.5\, R_{Sun}$. The shaded areas represent photons capable of ionizing the corresponding species. (b) The rate of photon production by the star with blackbody shown in panel (a).

to number of photons using the relationship, $N = \frac{E}{h\nu}$, where $N$ is the number of photons at the frequency of interest, $\nu$. The result of these adjustments is a frequency-dependent function for the number of photons produced by a star, $S_*$, and integrating the frequencies above the ionization potential will yield the total number of ionizing photons. The exact form of this relationship is then given by [46]

$$S_* = (4\pi R_*)^2 \int_{\nu_0}^{\infty} \frac{B_\nu(T_*)}{h\nu} d\nu \quad [\mathrm{s}^{-1}]. \tag{2.15}$$

To determine the rate at which these ionizing photons are absorbed by the surrounding ISM one must make use of the number density of the neutral hydrogen, $n_H$, and the cross-section for ionization, $\alpha_0$. The geometric dilution of the photons goes as $\frac{1}{r^2}$ making the spatial density of ionizing photons [46]

$$\rho_{Phot} = \frac{S_*}{4\pi r^2} = 4\pi \left(\frac{R_*}{r}\right)^2 \int_{\nu_0}^{\infty} \frac{B_\nu(T_*)}{h\nu} d\nu \quad [\mathrm{m}^{-2}\mathrm{s}^{-1}]. \tag{2.16}$$

Equation 2.16 tells us the flux of ionizing photons through a cross-sectional area, and this can be converted to a volumetric ionization rate by accounting for the ionization cross-section, and the volumetric density of the neutral hydrogen. The total ionization rate per unit volume is [46]

$$\dot{\mathcal{N}}_I = \alpha_0 n_H \rho_{Phot} \quad [\mathrm{m}^{-3}\mathrm{s}^{-1}]. \tag{2.17}$$

The ionizations are canceled out by recombinations of protons and electrons, represented by the right-to-left arrow in Equation 2.14. The rate at which the protons and electrons recombine to level $n$ is given by [46]

$$\dot{\mathcal{N}}_n = n_e n_p \beta_n(T_e) \quad [\mathrm{m}^{-3}\mathrm{s}^{-1}], \tag{2.18}$$

where $\beta_n$ is the recombination rate to level $n$, and depends on the electron temperature, $T_e$. In Equation 2.18 we can assume again that $n_e = n_p$ since the region is taken to be entirely comprised of hydrogen. If we also assume the region has uniform density then the recombination rate to each level becomes a constant value. The total recombination rate may be found by summing over the recombination to each state excluding the ground state, which, as stated earlier, may produce ionizing radiation that we account for by way of the 'on the spot' approximation. Excluding the ground state recombinations, the total recombination rate is given by the sum [46]

$$\dot{\mathcal{N}}_R = \sum_{n=2}^{\infty} n_e n_p \beta_n(T_e) \equiv n_e^2 \beta_2(T_e) \quad [\mathrm{m}^{-3}\mathrm{s}^{-1}]. \tag{2.19}$$

Equation 2.19 utilizes a total recombination coefficient of $\beta_2(T_e)$, and a useful approximation for this value is [46]

$$\beta_2(T_e) = 2 \times 10^{-16} T_e^{-3/4} \quad [\mathrm{m}^3\mathrm{s}^{-1}]. \tag{2.20}$$

With a number of simplifying assumptions we see from Equations 2.19 and 2.20 that the recombination rate is effectively constant, fixed by the electron temperature and the density of neutral hydrogen in the nebula prior to ionization.

If one assumes a spherically symmetric region to be fully ionized, the radius of such a region may be determined. Assuming that the ionized region is one in which the recombination rate of hydrogen from Equation 2.19 is exactly balanced by the rate at which ionizing radiation is produced then [46],

$$\frac{4}{3}\pi r^3 n_e^2 \beta_2(T_e) = S_* \quad [\mathrm{s}^{-1}], \tag{2.21}$$

and solving for the radius [46],

$$r = \left( \frac{3S_*}{4\pi n_e^2 \beta_2(T_e)} \right)^{\frac{1}{3}} \quad [\mathrm{m}], \tag{2.22}$$

shows that a canonical value for the radius may be found. In order to treat the problem more precisely one must account for the fractional ionization.

Because the recombination rate is effectively constant, dilution of ionizing radiation is the only factor in approaching ionization equilibrium. The equilibrium ionization rate is given by [46]

$$\dot{\mathcal{N}}_R = \dot{\mathcal{N}}_I \quad [\mathrm{m}^{-3}\mathrm{s}^{-1}], \tag{2.23}$$

and [46]

$$n_e^2 \beta_2(T_e) = \alpha_0 n_H \rho_{Phot} \quad [\mathrm{m}^{-3}\mathrm{s}^{-1}]. \tag{2.24}$$

Note that $n_e$ and $n_H$ must be related by the number density of neutral hydrogen atoms in the cloud prior to ionization [46],

$$n_e + n_H = n \quad [\mathrm{m}^{-3}]. \tag{2.25}$$

In this form it is possible to express both $n_e$ and $n_H$ in terms of fractional ionization as [46]

$$n_e = xn \quad [\mathrm{m}^{-3}], \tag{2.26}$$

and

$$n_H = (1 - x)n \quad [\mathrm{m}^{-3}], \tag{2.27}$$

respectively. Equations 2.26 and 2.27 allow the ionization equilibrium to be rewritten as [46],

$$\frac{x^2}{1 - x} = \frac{\alpha_0 \rho_{Phot}}{n\beta_2(T_e)} = \frac{\alpha_0}{n\beta_2(T_e)} \frac{S_*}{4\pi r^2}, \tag{2.28}$$

which is an expression for the fractional ionization of hydrogen as a function of the distance from the star. Solving for these values iteratively yields the curve shown in Figure 2.4, and as can be seen, the fractional ionization ≈1 until it rapidly drops off. This is an example of the aforementioned 'ionization stratification', and the distance at which the fractional ionization is equal to $\frac{1}{2}$ is known as the 'Stromgren Radius'. If we let $n_H = 10^8\,\mathrm{m}^{-3}$, and $T_e = 10^4\,\mathrm{K}$ then using Equation 2.22 we find the canonical Stromgren radius is 6.76 pc. This line is plotted in Figure 2.4 for comparison with the iterative solution to Equation 2.28 and the two show excellent agreement.

Incorporating the effects of helium and other heavier elements like oxygen and carbon make modeling the region very challenging as higher energy photons will ionize different species preferentially, based on energy dependent cross-sections for each species. Additionally, re-combinations from higher energy transitions in heavier elements will have sufficient energy to ionize hydrogen and the feedback makes modeling more difficult [51].

In order to better understand these regions astronomers need very sensitive detectors to see signal from under-abundant species. Since the structure of these regions is vital to understanding the relationship between ionizing radiation and the surrounding ISM, spectral and spatial resolution will also be critical in improving current models.

## 2.5 Gas Kinematics Surrounding Newly-Formed Stars

Since the photo-dissociation of molecules and ionization of atoms effectively increases the density, pressure waves form within the ionized regions and expand outward sweeping

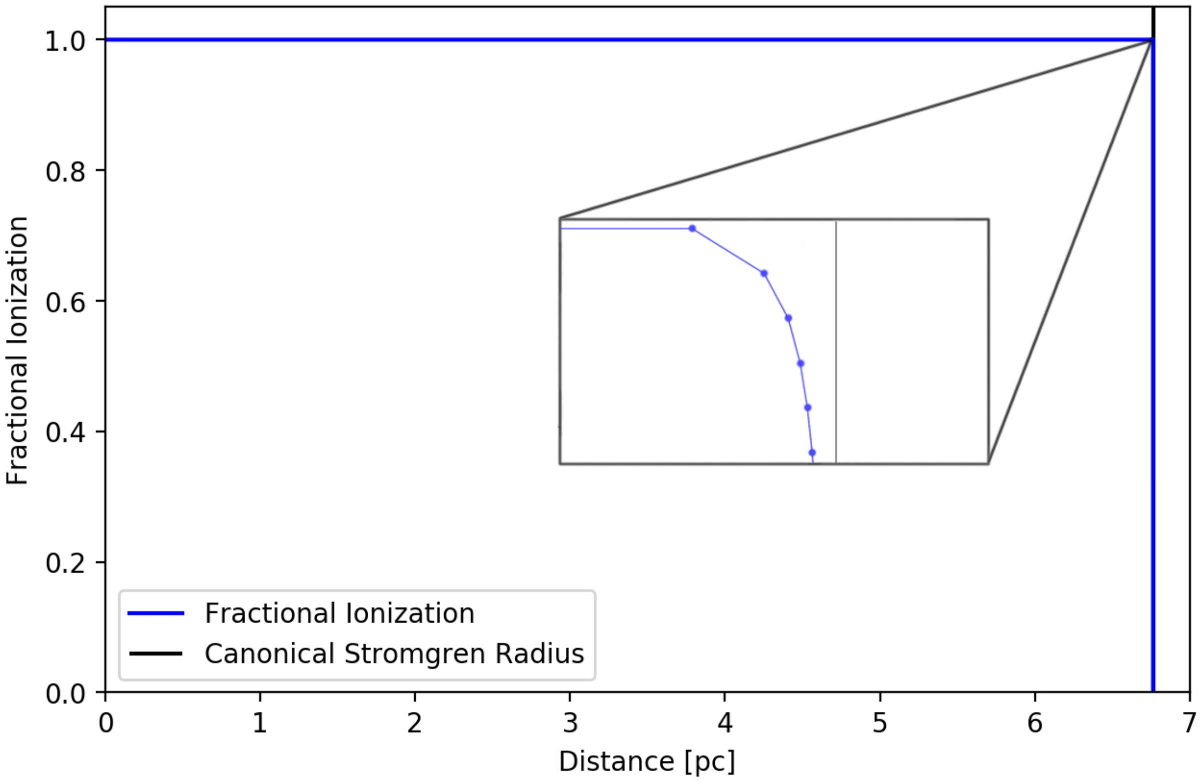

Figure 2.4: The fractional ionization of a pure $H_2$ region surrounding a newly formed star with r=12.5$R_\odot$ and T=40000K.

up dust and gas along the way. The kinetic energy of a traveling shock can excite neutral gas it comes into contact with. In this process shock-excited gases are created, and radiate away their energy in optical and IR fine-structure transitions when the electron temperature is $5\times10^3\,\mathrm{K}\lesssim T_e \lesssim 10^5\,\mathrm{K}$, typical of an interstellar cloud [46]. Observing these lines around a given source provides further evidence of ongoing star formation as these outflows are only present in the earlier stages of stellar evolution when the source is still embedded in a molecular cloud.

Testing the theoretical models of star formation involves searching for these specific tracers and measuring their spatial distributions. Current models are strongly constrained and highly degenerate owing to the difficulty in identifying sources at each relevant stage of star-formation as well as the quality of relevant data from observations of the identified sources [59].

## 2.6 EGOs

One particularly interesting example of massive star formation are the Extended Green Objects (EGOs) discovered in the *Spitzer* Galactic Legacy Infrared Mid-Plane Survey Extraordinaire (GLIMPSE) survey [60, 61]. Detecting sites of massive (stars with $M > 8M_\odot$ may collapse to form black holes [47]) star formation is very challenging due to the relative infrequency of massive stars paired with their rapid development, thus EGOs offer a unique testing ground for probing current theory.

The EGO sources are defined by their extended emission in the *Spitzer* IRAC instrument's $4.5\,\mu$m band coded as green. It is believed this extended emission traces proto-stellar outflows of shock-excited gas [59]. The EGOs are also associated with infrared dark clouds, and lie in the region of MIR colour-colour space associated with young stellar objects. A follow-up maser survey with the Very Large Array (VLA) showed that $\gtrsim$64% of a sample of 28 EGOs surveyed are associated with Class II 6.7 GHz $CH_3OH$ masers which trace massive young stellar objects [62]. Furthermore, $\sim$89% of the EGOs associated with Class II masers are also associated with Class I 44 GHz $CH_3OH$ masers which are associated with molecular outflows. Complimentary data taken with the James Clark Maxwell Telescope (JCMT) showed that the EGO sources are also correlated with molecular emission from SiO(5–4) and $HCO^+$(3–2) which both trace shock-excited gases. Warm in-falling dust has been traced by $24\,\mu$m continuum emission detected by the Multiband Imaging Photometer (MIPS) instrument on-board *Spitzer*, and a lack of 44 GHz continuum emission rules out the possibility that molecular outflows are being powered by ultra-compact HII regions. All of this evidence taken together suggests that EGOs are massive young stellar objects with molecular outflows powered by ongoing accretion.

A subset of four EGO sources were selected for follow-up observations with the Spectral and Photometric Imaging REciever (SPIRE) and the Heterodyne Instrument for the Far-Infrared (HIFI) instruments on-board the Herschel Space Observatory due to their strong association with all of the above criteria. Preliminary modeling of the sources yielded dust and gas temperatures, dust emissivity, and column densities for $H_2$ and CO. Due to the high degeneracy of theoretical models, these parameters still have a significant degree of uncertainty. Many of the assumptions which have gone into the models used are also known to not hold true.

Consider the EGO G11.92-0.61 for instance. Simpler models assume that a source is spherically symmetric and in Herschel observations this appears to be a valid assumption. However, follow-up observations from the ALMA observatory revealed that in this particular source there were 19 individual cores distributed throughout the cloud as shown in Figure 2.5 below.

Even the smaller cores within the EGO identified by ALMA are relatively large and recent observations have shown that MM1 contains substructures which warrant further investigation [64]. The inability to distinguish multiple sources is termed 'source confusion', and is a fundamental issue for modeling. Attempts to model G11.92-0.61 using the spectral energy distribution from photometric observations at 9 wavelengths spanning 3.6 $\mu$m to 870 $\mu$m preferred models without a disk which is a direct contradiction of observational data [65]. Towner et al. [65] state that none of their models accurately describe the source, and suggest this is due to insufficient spatial resolution in the infrared sources which is necessary to distinguish smaller structures. There are other ways to disentangle multiple sources including improvements in spectral resolution coupled with increased sensitivity which enables discrimination between source components based on chemical makeup and velocity, but improving spatial resolution when possible is one of the most effective methods. All FIR observatories have considerably poorer spatial resolution than ALMA and if astronomers wish to mitigate source confusion then significant improvements to spatial resolution will be needed in future FIR missions.

Despite the difficulty in modeling, important physical information can be gleaned from the limited data available. The lines detected by *Herschel*, seen in Figure 2.6, confirm that the EGOs are molecular clouds and the expected molecular transitions are present. In addition

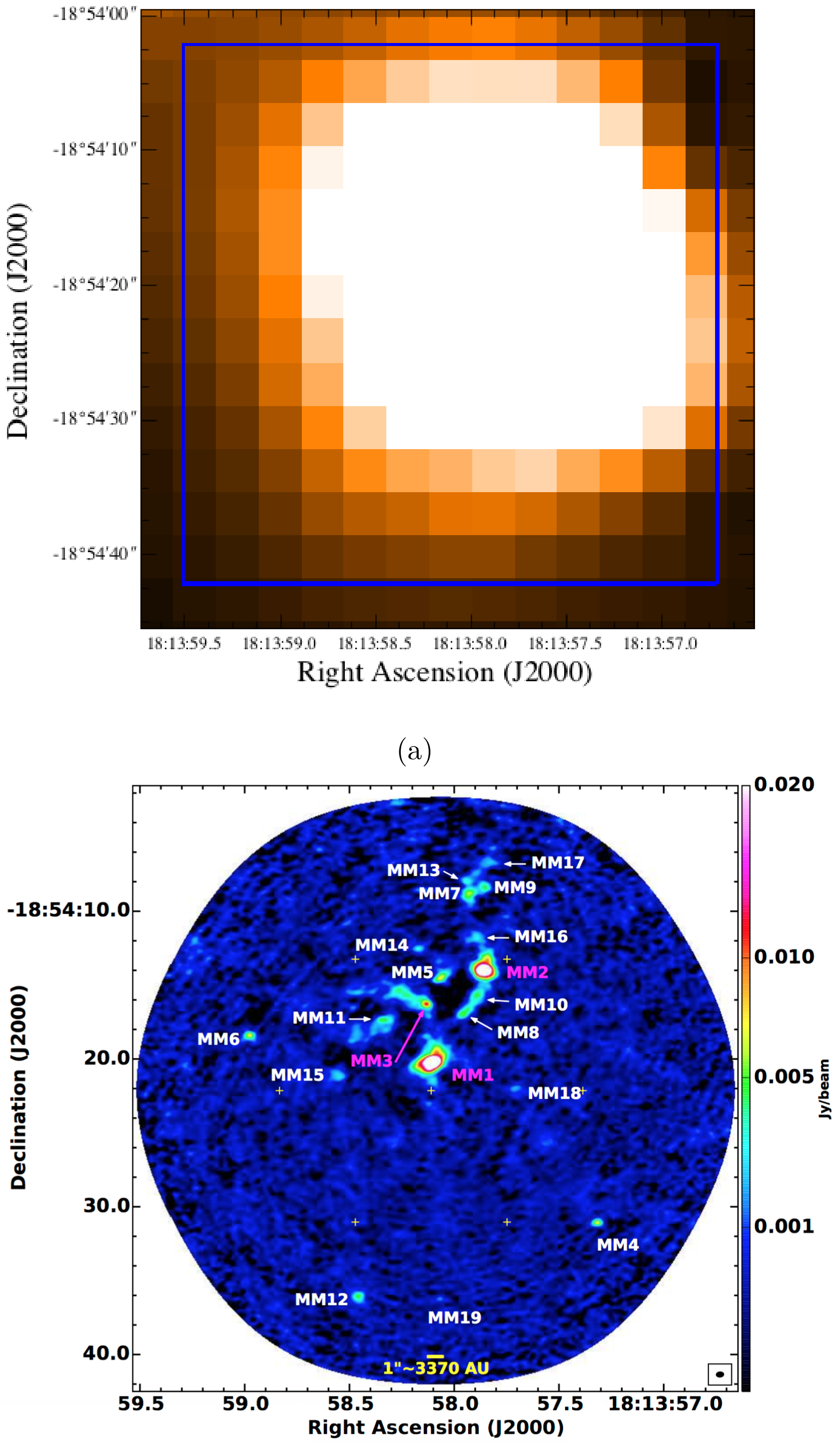

(a)

(b)

Figure 2.5: The EGO G11.92-0.61 as viewed by the Herschel space telescope (a) and ALMA (b). Note the differences in spatial resolution, ALMA has a much finer view of the sources which appear as one coherent source in the Herschel data. ALMA view acquired from Cyganowski et al., 2017 [63].

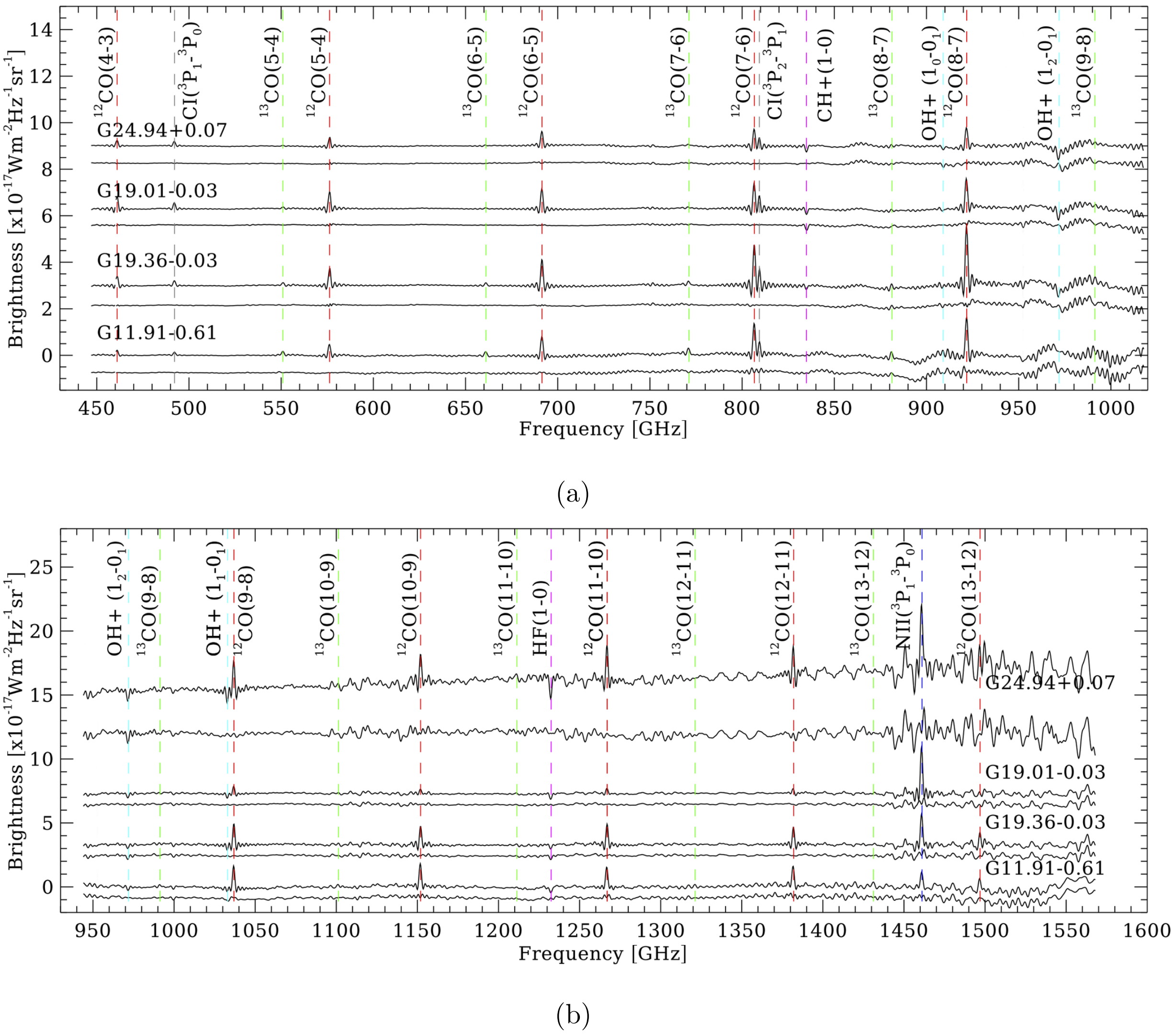

Figure 2.6: Continuum-subtracted SPIRE long wavelength (a) and SPIRE short wavelength (b) observations of four EGOs.

to the abundance of CO lines, it can be seen that every source is associated with an ionized nitrogen line at ∼1460 GHz, and neutral carbon transitions at ∼490 GHz and ∼810 GHz. It is important to note that NII, CI, and CO transitions arise in different energy regimes and can't be co-located. This means that despite the fact all these signatures are associated with cooling molecular clouds as per Section 2.1, we must be observing different regions when all the signatures are present in the same spectrum. The mapping qualities of the SPIRE spectrometer meant that the spectra can also be overlaid with photometer maps to show the spatial extent of spectral features. This is demonstrated in Figure 2.7 which shows that the

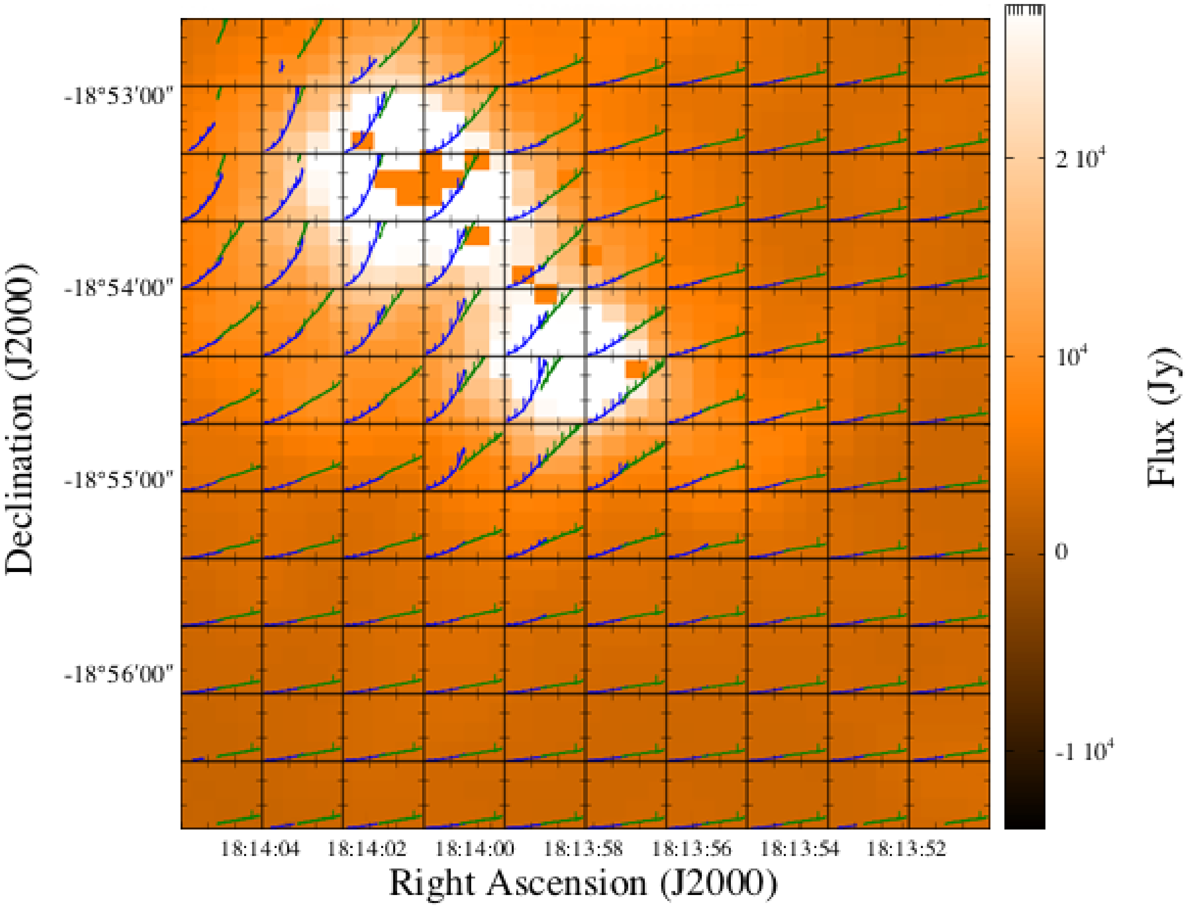

Figure 2.7: SPIRE 250 $\mu$m photometer map with overlaid spectral map. The blue spectra represents the SPIRE long wavelength observations and the green spectra is the SPIRE short wavelength band. Dark pixels on the source indicate dead pixels.

CO transitions are associated strongly with the source, whereas the NII emission is spatially ubiquitous. The $^{12}$CO transitions were used in the modeling in Figure 2.2 as they are most strongly correlated with the bright continuum emission of the EGO.

Figures 2.8 and 2.9 show examples of species towards G11.92-0.61 observed with high spectral resolution and SNR. In addition to the HCO+ line detected by JCMT and the species seen by HIFI there are at least three other molecular species which have been detected towards G11.92-0.61 [62]. All seven of these species identified towards G11.92-0.61 have transitions within the SPIRE waveband that were too faint to be detected within the SPIRE spectrometer observation. These undetected species demonstrate that increased sensitivity

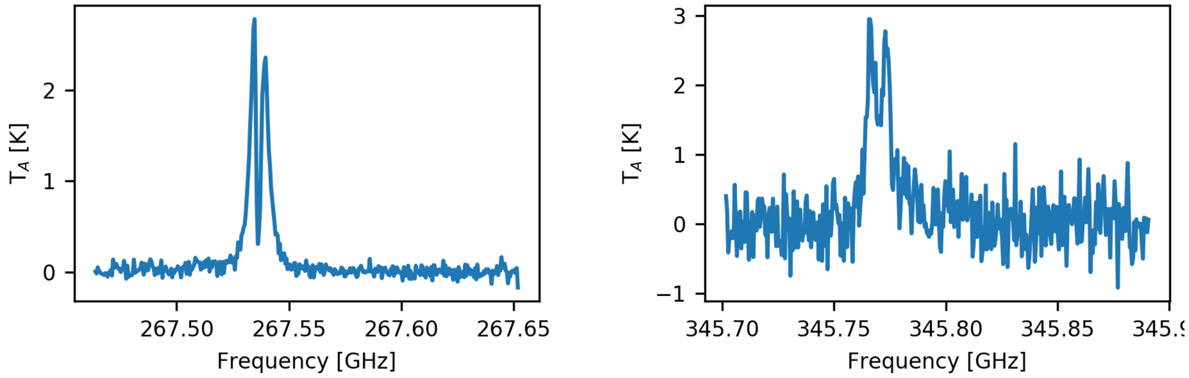

(a) (b)

Figure 2.8: Two lines seen by JCMT towards the EGO G11.92-0.61. (a) HCO+ (3-2) transition. (b) $^{12}$CO (3-2) transition. Acquired form the JCMT database [66].

is an area in which the quality of FIR observations can be improved. The combination of reduced background through cryogenically cooled optics and an increase in spatial resolution by use of long baseline interferometers will enable detection of many more under-abundant species.

HIFI observations of G11.92-0.61, shown in Figure 2.9, also demonstrate that better resolved spectra will inform modeling of the gas kinematics. With very high spectral resolution the shape of the emission line will carry information about the velocity profile of the source. For unresolved spectral features, spectral resolution in a Fourier transform spectrometer such as SPIRE is determined by the maximum optical path difference between two inputs, $L_{OPD}$, [67]

$$\Delta\sigma = \frac{1}{2L_{OPD}} \quad [\text{cm}^{-1}], \tag{2.29}$$

where $\Delta\sigma$ is the spacing in the frequency array [67]. Note that in Fourier spectroscopy inverse wavelength is used for frequency, but can be converted to conventional frequency using the speed of light. This is another significant way in which long baseline interferometry can aid FIR astronomers in understanding the sources in which they are interested, particularly sites of massive star formation where the kinematics are critical to searching for and modeling molecular outflows, in-falling clouds and disk formation [68].

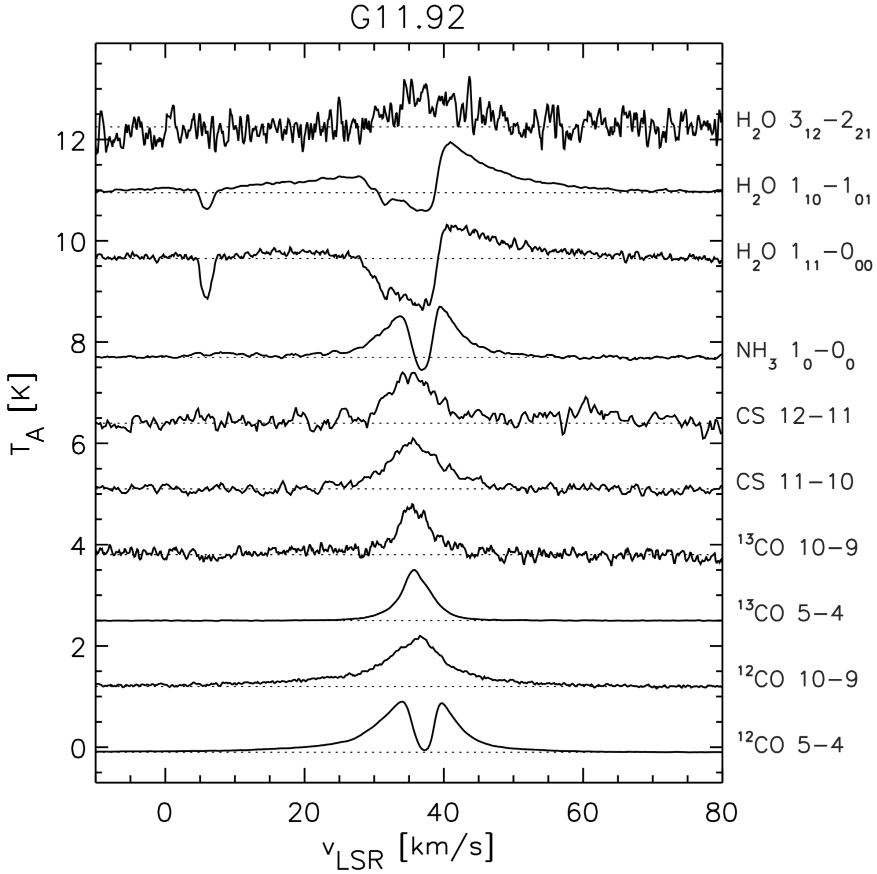

Figure 2.9: Lines seen by HIFI towards the EGO G11.92-0.61 plotted in velocity space. All of these lines have transitions which fall in the SPIRE band. Provided by Dr. Adwin Boogert via private communication.

## 2.7 Conclusion

Understanding the process by which stars, particularly massive stars, come to form is a tremendous technical challenge owing to the relatively small population of these sources and the difficulty in identifying them. Current models are insufficient for describing the physics of these regions, and often even the highest quality scientific data produce models which directly contradict observational evidence [65]. In order to improve on these models it is critical to identify relevant sources, such as EGOs, and to improve the quality of scientific data available on these sources. A space-borne interferometer could in principle provide tremendous improvements in spatial and spectral resolution, and with cryogenically cooled apertures could reduce thermal noise enough to detect important relatively under-abundant species like $H_2O$.

The success of interferometry depends heavily on precision timing and position measurements in order to preserve coherence of the incident signal. As mentioned in the introduction to this thesis the relative positions of dishes must be known to within a fraction of a wavelength and this necessitates precision metrology. A laser metrology system may be one of the best options for tracking the relative position of optical components with the necessary precision at great distances [69]. Studying the applications of laser metrology as well as understanding the limitations of such systems is therefore important for astronomical interferometry and Chapter 3 covers that topic.

# Chapter 3

# Characterization of Laser Interferometer Metrology Systems

As outlined in both Chapters 1 and 2, long baseline interferometry is an appealing prospect for FIR astronomers because of the potential improvement in spatial resolution offered by the technique. However, in order to successfully perform this type of observation, the relative positions of receiving apertures must be known to sub-wavelength precision. A few examples of existing metrology sensor types and their approximate specifications are shown in Table 3.1. Comparison with other methods demonstrates the utility of interferometer systems for the long range over which they may be used without sacrificing high precision. For more information on the listed metrology systems see Appendix A.

Table 3.1 also demonstrates that interferometers have exceptionally good resolution, and are therefore also useful for short range measurements. A three-phase metrology system developed for the monitoring of position in a Fabry-Perot interferometer [70] was re-purposed

Table 3.1: Comparison of the capabilities of different position metrology systems. Acquired from Naylor et al. [70], based on Fleming [69].

| Sensor Type | Range | Resolution [nm] | Accuracy |
|---|---|---|---|
| Resistance | $10-500\,\mu$m | 23 | 1% Full-Scale Range |
| Capacitive | $10\,\mu$m $-$ 10 mm | 2.4 | 0.1% Full-Scale Range |
| Eddy Current | $100\,\mu$m $-$ 80 mm | 1 | 0.1% Full-Scale Range |
| LVDT | 0.5 – 500 mm | 5 | 0.25% Full-Scale Range |
| Optical Encoder | 1 m | 6 | 5 ppm |
| Interferometer | >1 m | 0.5 | 1 ppm |

to make measurements of thermal contraction at cryogenic temperatures. The design of these experiments is covered in Chapter 4. Preliminary tests with the Renishaw indicated that measurements of thermal expansion necessitated a system internal to the cryostat, and therefore the laser metrology system needs to operate under vacuum.

## 3.1 Three-Phase Metrology System

The Astronomical Instrumentation Group based out of the University of Lethbridge designed and manufactured a system which uses the interference of three coherent signals with mutual phase difference of 120° to measure magnitude and direction of change in distance with a reported precision of approximately 2.3 nm [71, 72].

The metrology system works by guiding laser light from an Eblana DX1-DM laser diode and thermo-electric control (TEC) [73], hereafter referred to as the 'Eblana', through a circulator which prevents back-reflections that may interfere with laser stability. After passing through the circulator, the light enters a 3x3 splitter which splits the input signal into three equal-intensity signals with mutual phase differences of 120°. Of these three signals, one is terminated and the other two are projected through collimators and through a free-space interface towards Thorlabs PS974M-C [74] retro-reflectors. The two signals which are reflected back re-enter the circulator where the signals are again split into three and intensity at the optical outputs is converted to a voltage by three InGaAs photodiodes. Each of the three outputs, ($U_a$, $U_b$, $U_c$) are normalized and converted to quadrature by use of the Clarke transform [70], and the phase difference in quadrature may then be converted to a difference in optical path length [70]. Figure 3.1 shows the optical schematic of the metrology system.

Preliminary tests using the three-phase system to measure the CTE of aluminium revealed a number of sudden changes in position recorded by the metrology system. The difference in position from each point to the next was plotted and it was found that they clustered around multiples of half-integer wavelengths corresponding to integer wavelengths in optical path difference (OPD) as shown in Figure 3.2. This seemed to indicate that the

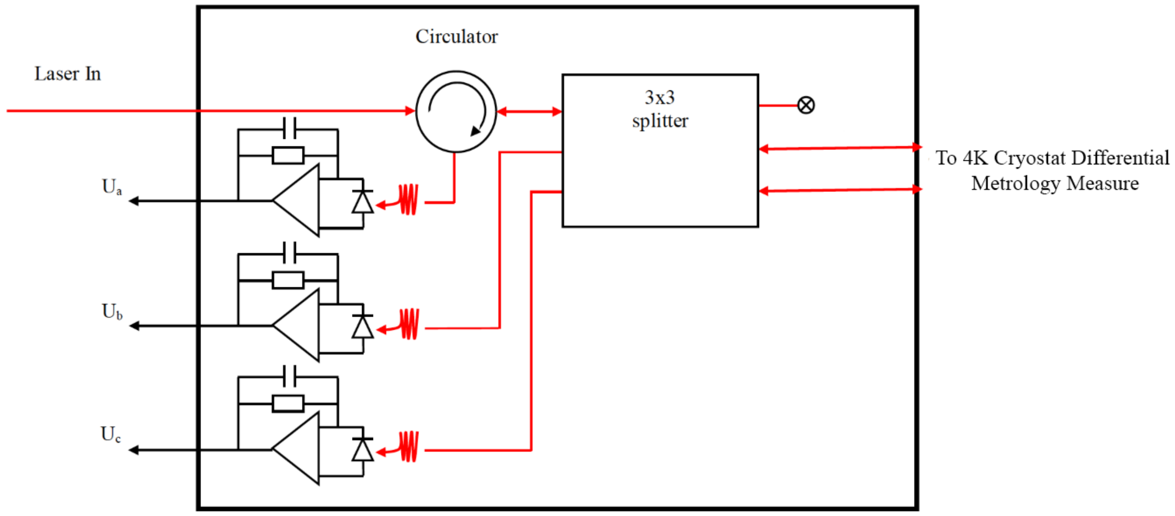

Figure 3.1: Schematic representation of the optical path within the three-phase interferometer, where red lines indicate the path of the laser. Figure adapted from Naylor et al. [70].

skips are a product of the data reduction algorithm rather than physical. The peculiar behaviour of the metrology system prompted more rigorous testing of the system to determine the cause.

## 3.2 Characterization

The absolute precision of the three-phase metrology system was determined to be ∼2.3 nm [71]. This was determined by fitting a polynomial function to a segment of a sinusoid ∼20 ms in duration and ∼3 $\mu$m in magnitude of displacement as shown in Figure 3.3 [71]. Utilizing the metrology system for measurements within the cryostat presented a number of challenges not present during the original calibration, which made it necessary to test for robustness against issues such as rapid accelerations brought on by mechanical shocks and vibrations, long-distance motion, and running for an extended period of time. The Aerotech linear translation stage and the Renishaw interferometer were used in the lab to test the precision of the metrology system against more reliable metrics.

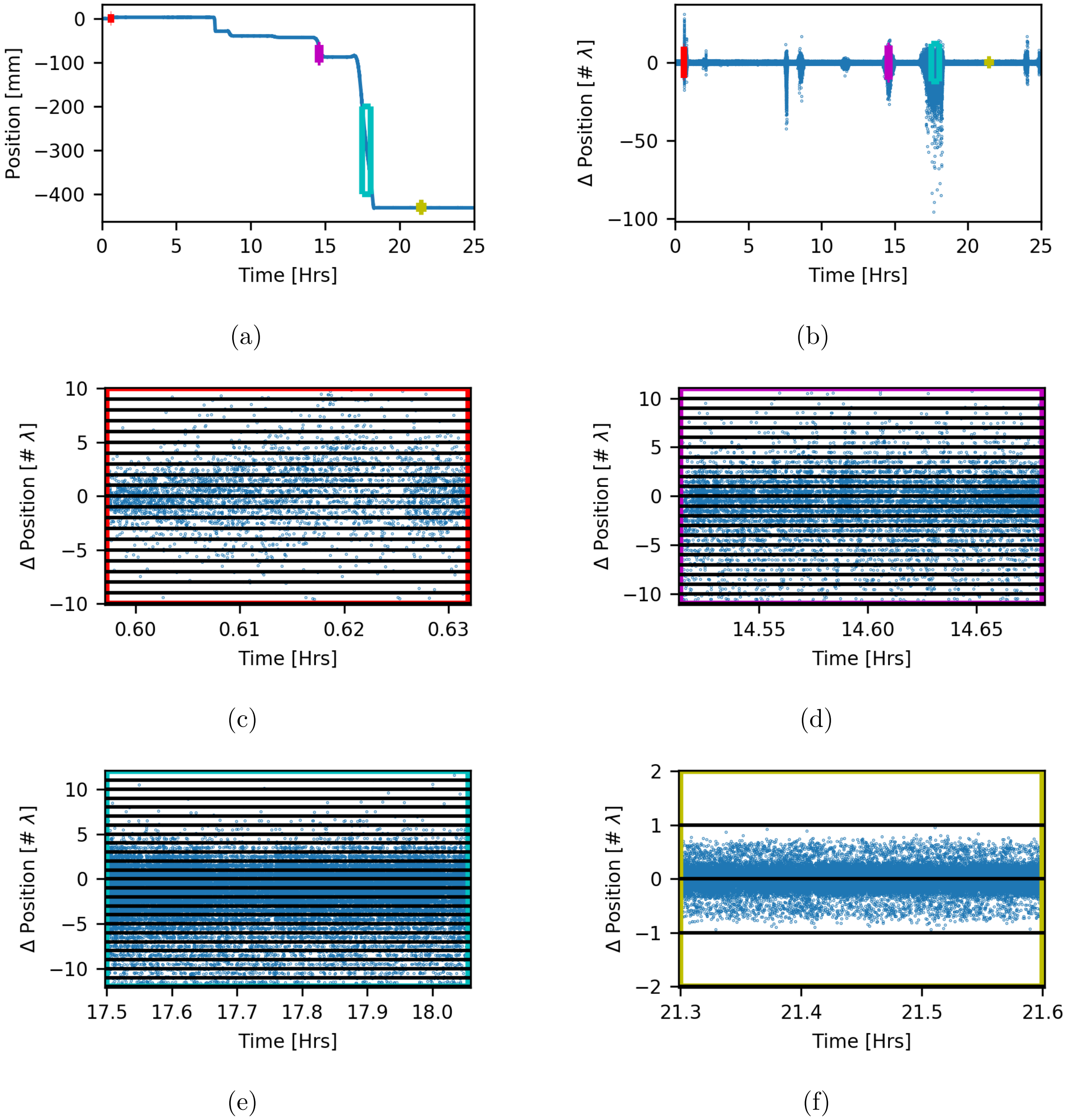

Figure 3.2: Discretization of length data recorded with the three-phase metrology system. (a) Faulty position data taken during a warmup when the metrology system was not behaving as predicted. The length change is in units of millimeters and approximately three orders of magnitude larger than the predicted expansion. (b) The change in position (Δx) converted to number of wavelengths. Regions of interest highlighted in red, magenta, cyan, and yellow corresponding with panels (c) through (f) respectively. (c) Zoom of the red square in panel (b). (d) Zoom of the magenta square in panel (b). (e) Zoom of the cyan square in panel (b). (f) Zoom of the yellow square in panel (b). The discrete bands shown in panels (c) through (f) show that segments of the data corresponding to rapid non-physical changes in position cluster about integer wavelength intervals.

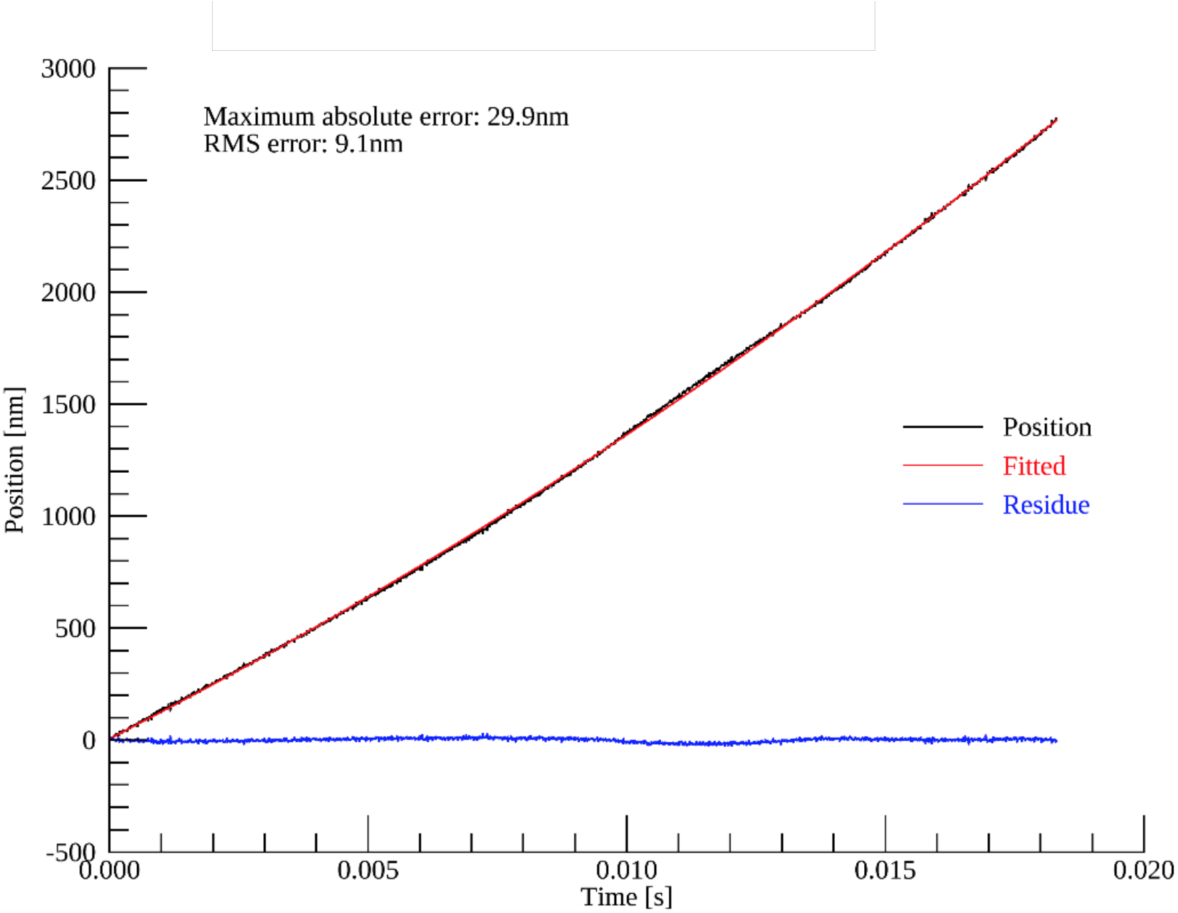

Figure 3.3: First calibration of the three-phase metrology system showing very high precision over a limited magnitude and duration. Optical path difference of 9.1 nm is a factor of 4 greater than mechanical path difference making position uncertainty 2.3 nm. Figure Source: Veenendaal et al. [71].

The Renishaw (Section 1.2) was used as the benchmark measurement for the simple reason that it has a precision of 38.6 pm [75], better than either the three-phase system or the Aerotech stage (Section 1.2). The Aerotech stage has a position synchronized output (PSO) which reports a time-stamp every time the stage has moved a certain distance down to 15.82 pm. The experimental setup is shown in Figure 3.4.

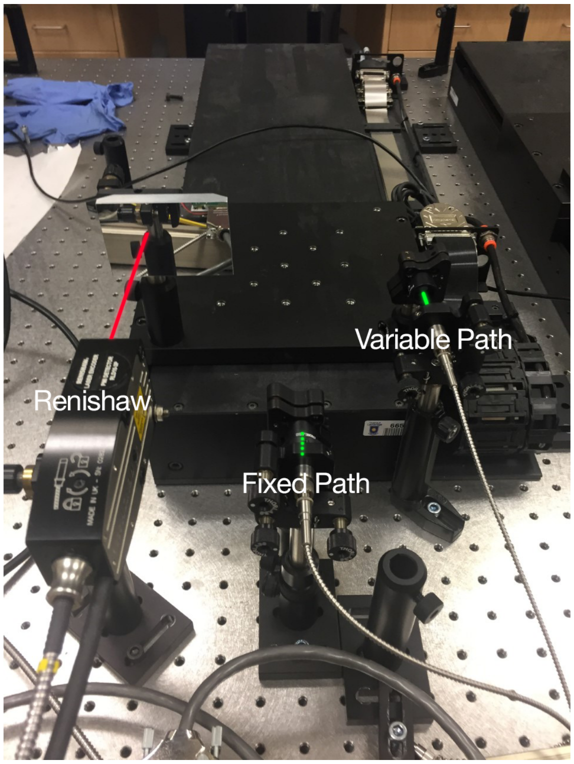

Figure 3.4: The setup used in comparing the precision of the three-phase metrology system to that of the Renishaw. The Renishaw may be seen at left with the approximate optical path shown in red, with the two ends of the three-phase metrology system shown in armoured cables at right. The green dashed line is the fixed beam path and the green solid line shows the variable beam path.

The primary objective in characterization was to determine what level of precision could reliably be expected from the metrology system in a comparable environment to that of the operating cryostat. Using the linear translation stage meant it was also possible to test a range of velocities and accelerations to determine whether physical shocks causing rapid acceleration (impulses) led to a breakdown in the metrology. Given the lack of mechanical isolation within the cryostat, physical impulses are expected during cool-down as the pulse tube cooler (PTC) is still in operation and the pulsing introduces vibration to the cryostat. Even during the warmup period during which the PTC compressor system is off it is possible that natural movements about the room or building may cause shaking of the sample. These vibrations may be large enough to cause the metrology system to lose track of fringes by displacing the retro-reflector a distance of more than $\frac{\lambda}{4}$ in a sampling period. If this occurs then it may be an impractical approach for obtaining measurements of thermal contraction, particularly whilst the PTC is in operation.

To test the consistency of the three-phase metrology system it was used to measure the distance traveled by the Aerotech stage, run at a series of different speeds ranging from $10\,\mathrm{nm/s}$ to $800\,\mu\mathrm{m/s}$. While some of these speeds were outside of the stage specifications, the data collected verified that the stage traveled as commanded. The stage was commanded to go back-and-forth in a triangle wave with brief periods of rest at the scan boundaries. This motion was typically repeated between five and ten times depending on the speed and length of the trial. Testing the consistency of the system when used continuously for many hours ($\sim$35–45 hours for a full thermal cycle in the cryostat) was simulated by having the metrology system measuring the position of a reflector on the Aerotech stage as it was stationary overnight. Finally, the metrology system must be robust against vibrations, so impulse testing was performed, where the collimator mount or the stage were lightly jarred (either by gently flicking the mount, or rotating the retro-reflectors in place). All of these experiments were performed with the Aerotech stage mounted to a vibration-isolated Newport Actively Damped Smart Table [76] to minimize environmental noise.

The tests performed on the optical table demonstrated similar problems seen during cryogenic testing with the three-phase system. In addition to the nominal skips, shock testing would sometimes induce skips in the data, but other times did not, rendering this qualitative level of impulse testing inconclusive. Likewise, long duration measurements were occasionally successful but unpredictable at best as skips, and a general ‘drifting’ of the length were both observed. These are discussed in subsection 3.2.3.

### 3.2.1 Comparison with the Renishaw

As mentioned, determining the precision of the metrology system was done by comparison with the Renishaw. If the three-phase system is as precise as the Renishaw and the two devices are perfectly co-aligned then the residual between them should have noise normally distributed about zero. The residual between the two length measurements will carry information about the metrology system, assuming the Renishaw is functioning correctly. This information can be used to determine the effective precision of the three-phase system in normal operation, and will highlight any systematic issues.

The difference in distance recorded by the Renishaw and that recorded by the three-phase metrology system is shown in panels (a) through (d) of Figure 3.5. The length has been converted from microns to number of wavelengths in OPD to emphasize the discretized nature of the problem. As can be seen, particularly in panel (d), there exists a nominal noise level between the skips, but the magnitude of the skips obscures the lower-amplitude noise. The magnitude of the skips is consistently a power of two, steps of 2 and 4 integer counts at the smallest level (panel (d)) and in approximately 128 integer counts in the largest skips (panel (c)).

The hypothesis developed was that the bit priority in data conversion was scrambled for some of the least significant bits. The rapid variations expected in the least-significant bit were thought to be manifesting in more-significant bits. This would cause rapid changes on a larger scale, but would also be approximately random in nature. The problem was diagnosed as a bad electrical connection, and replacing the damaged connector corrected these periodic integer jumps in the data resulting in a change from the data seen in Figure 3.5 to that shown in Figure 3.6. After resolving the bad connector, further testing showed that the three-phase metrology system still lacked the absolute precision of the Renishaw system, and testing shown in subsection 3.2.3 shows that the discretized skips persisted.

The three-phase metrology system had been reading shorter path lengths than both what was commanded and reported by the stage, and what the Renishaw measured as the

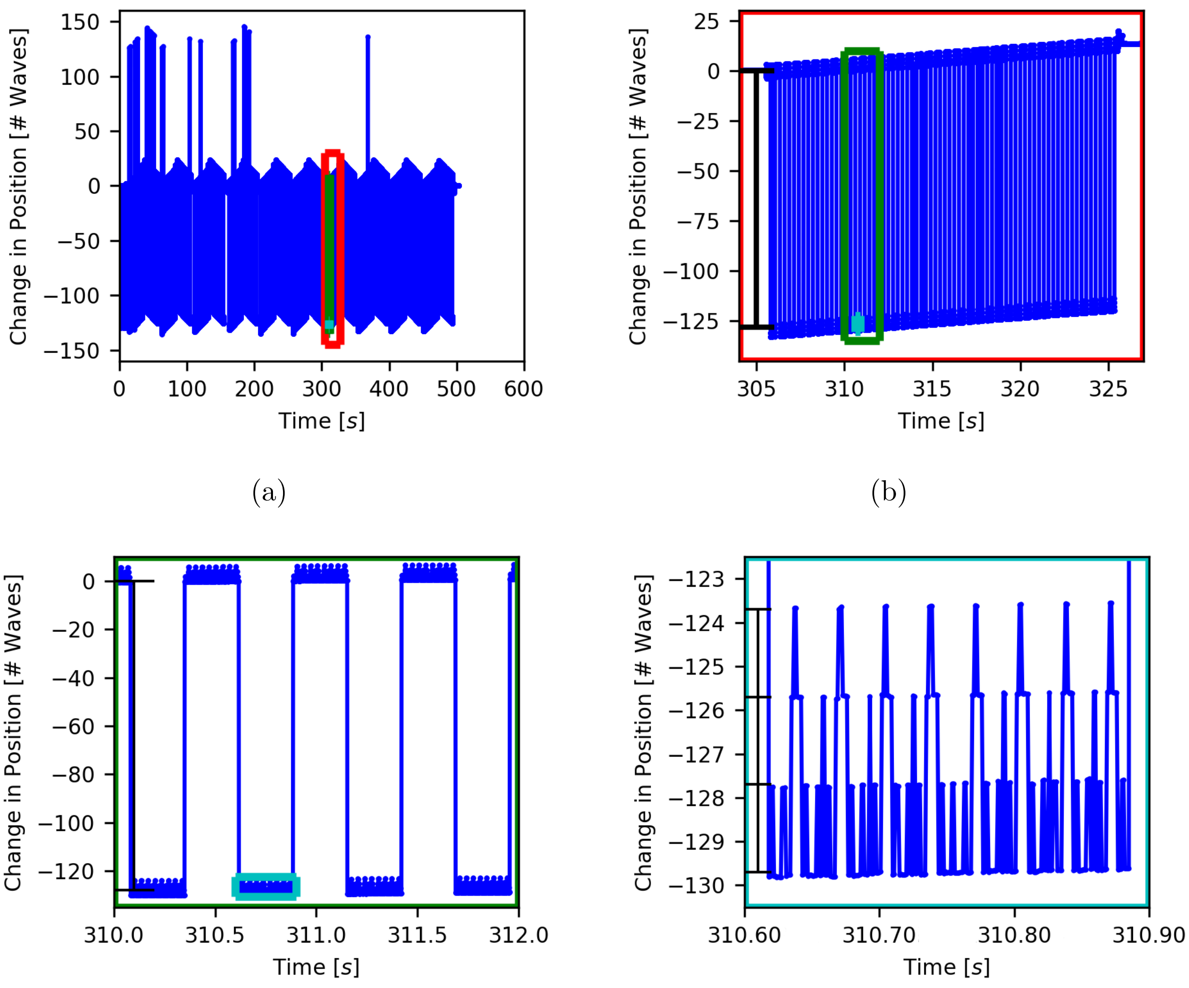

(a) (b)

(c) (d)

Figure 3.5: The residual of the three-phase metrology system after subtracting the length recorded by the Renishaw data. Zooming in on the residual demonstrates the discrete nature of the skips in the data. (a) Path difference between the three-phase metrology system and the Renishaw for the entire scan. (b) Residual inside the red box shown in panel (a) representing a single scan. The black bar denotes a step of 128, showing the skips to be integer counts. (c) Residual inside the green box shown in panel (b). The black bar denotes a step of 128, showing the skips to be integer counts. (d) Residual inside the cyan box shown in panel (c). The black bar denotes steps of 2, showing the skips to be the same integer counts.

distance traveled. Agreement between the Renishaw and the commanded distance for the stage to travel indicated that the problem was in the three-phase metrology system and not the Renishaw. Running a series of trials at different velocities, and different commanded

Table 3.2: Comparison between the three-phase metrology system and the Renishaw interferometer. The relative difference was found by fitting a straight-line to a plot of difference in position as a function of position. The trial shown in Figure 3.6 corresponds with the 750 $\mu$m/s trial in this table, and all of these trials were performed after the faulty electrical connection had been fixed.

| | | Sampling Frequency [Hz] | | |
|---|---|---|---|---|
| Speed [$\frac{\mu m}{s}$] | Distance [mm] | Renishaw | Three-Phase | Relative Difference in Distance [%] |
| 0.01 | 0.001 | 10.0 | 5.0 | 0.62(4) |
| 0.05 | 0.05 | 10.0 | 5.0 | 1.870(9) |
| 1 | 0.05 | 500.0 | 100.0 | 1.419(12) |
| 50 | 5 | 5000.0 | 500.0 | 1.17151(1) |
| 100 | 15 | 25000.0 | 5000.0 | 1.170616(3) |
| 200 | 15 | 25000.0 | 1000.0 | 1.17251(9) |
| 400 | 15 | 25000.0 | 5000.0 | 1.170772(5) |
| 500 | 15 | 25000.0 | 5000.0 | 1.170806(6) |
| 600 | 15 | 25000.0 | 5000.0 | 1.170109(4) |
| 750 | 15 | 25000.0 | 1000.0 | 1.308(3) |
| 800 | 15 | 25000.0 | 5000.0 | 1.170616(3) |

distances revealed a fairly consistent scale-factor by which the metrology system differed from the Renishaw. The tabulated results for the different trials including their sampling frequencies, and the relative difference in recorded length between the Renishaw and the three-phase system are shown in Table 3.2.

The relative difference between the two measures was found by plotting the difference in measured position as a function of the distance measured by the Renishaw. Since the trials involved a number of back-and-forth motions, any relative differences would be seen numerous times. An example of the scaling is shown in panel (b) of Figure 3.6, with the absolute data shown in panel (a) of the same figure.

The results of these tabletop trials revealed that the three-phase system has a characteristic difference when compared to the Renishaw results. It was postulated that perhaps this was due to an error in the wavelength of the laser, approximately 1550 nm, however, this error corresponds to a change in wavelength of ∼17 nm, outside of the reported 3 nm uncertainty [77]. Time constraints prevented an investigation into the specific wavelength of

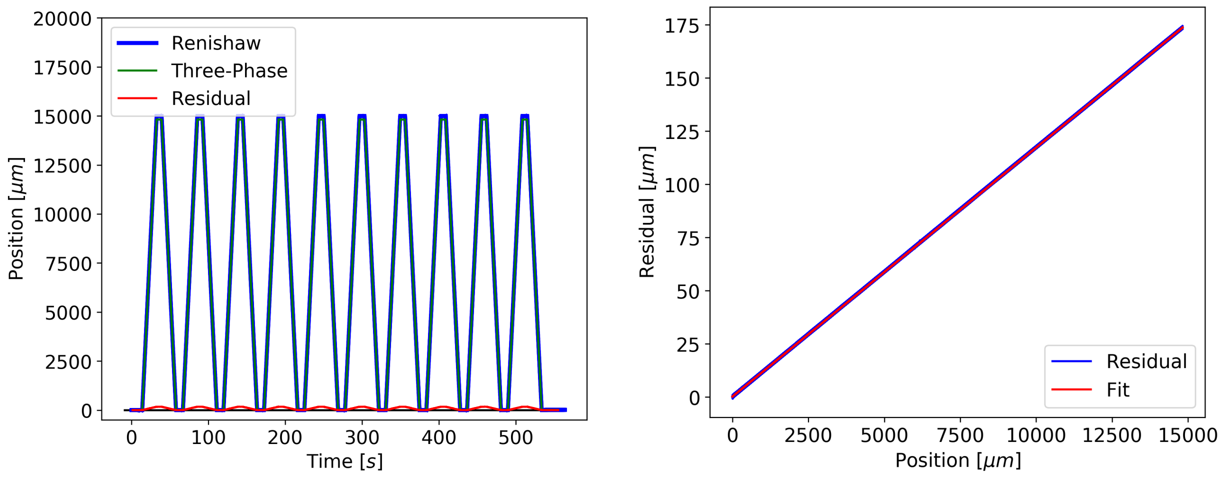

(a)

(b)

Figure 3.6: The raw measurements made by both the Renishaw, and the three-phase metrology. (a) The absolute measures of distance recorded by the Renishaw and the three-phase metrology system and the residual between them. (b) The difference in distance recorded by the Renishaw and the three-phase metrology system as a function of the distance measured by the Renishaw. The constant slope is indicative of a systematic difference between the two measurement systems.

the laser. Another suggestion was that perhaps the scaling was a cosine factor from misalignment, but a misalignment would result in measures longer than that of the Renishaw, rather than shorter. Additionally, since the alignment of the optics was done over approximately 500 mm, and the beam width is only approximately 2 mm for the Renishaw the angular tolerance for this beam is less than a quarter of one degree and would not result in changes to path length of the magnitude observed. Although this problem persisted, the consistency of the difference meant that it could be empirically corrected and time constraints prevented further investigation.

### 3.2.2 Comparison with the Aerotech PSO

The testing of the metrology system also allowed testing the precision of the Aerotech stage. If the stage is to be used as the arm of an interferometer then its motion must be well-understood. Deviations from linear velocity, and uncertainty in reported position during measurement of an interferogram contribute significantly to uncertainty in recovered spectra.

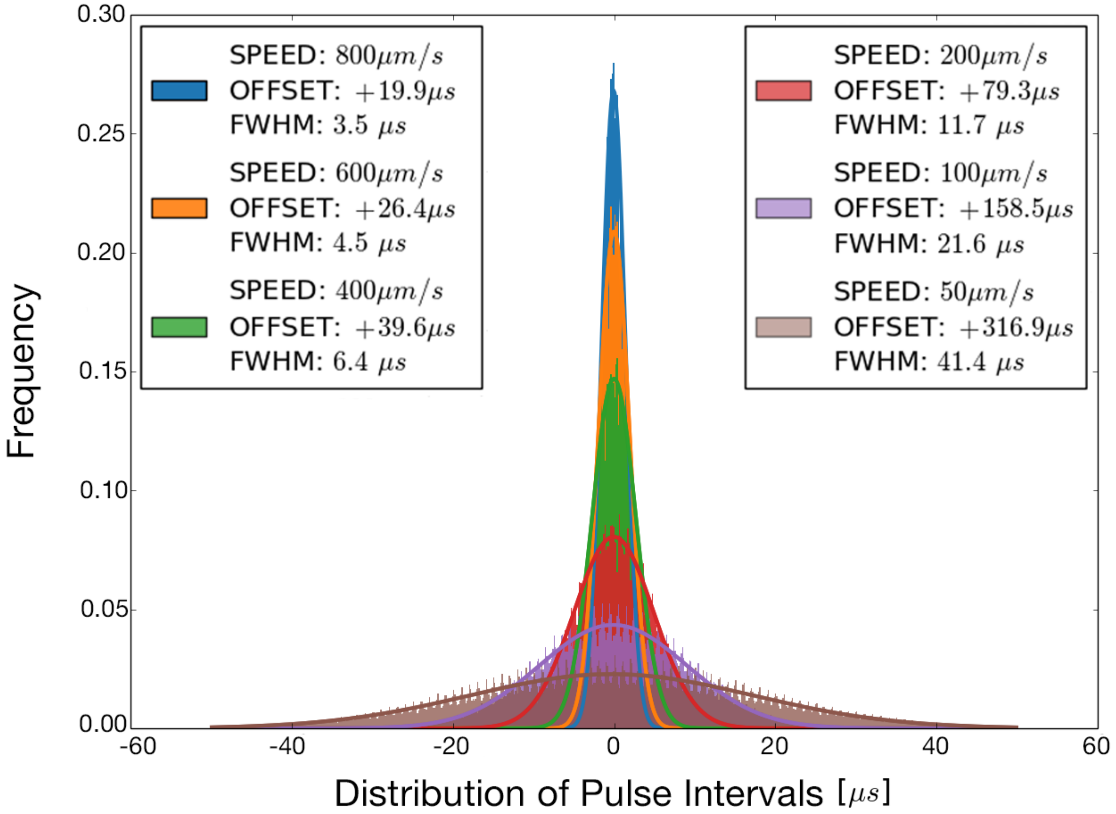

Figure 3.7: Distribution of pulse intervals for Aerotech PSO. Narrowing distribution towards faster speeds is a product of the consistency in relative error. Normalized histograms of the timing between PSO pulses when the stage was run at different velocities fitted with a Gaussian function. The faster the stage was run, the more closely spaced the timing gaps are expected to be.

The stage was commanded to move at many different speeds, and along differing path lengths. At a constant speed the PSO pulses would be expected to trigger with constant timing intervals, however this is not what was observed. As demonstrated by the slope of the plot in Figure 3.8, the PSO is consistently subject to about 12.7% relative error in timing with the parameter settings used.

This relative uncertainty was seen to apply nearly exactly at every speed between 50 $\mu$m/s and 800 $\mu$m/s and the Gaussian shapes of the distributions seem to indicate that this error is random. This disparity in PSO interval timing could result from a combination of an uncertainty in the PSO distance, deviations from linearity in the velocity of the stage, and

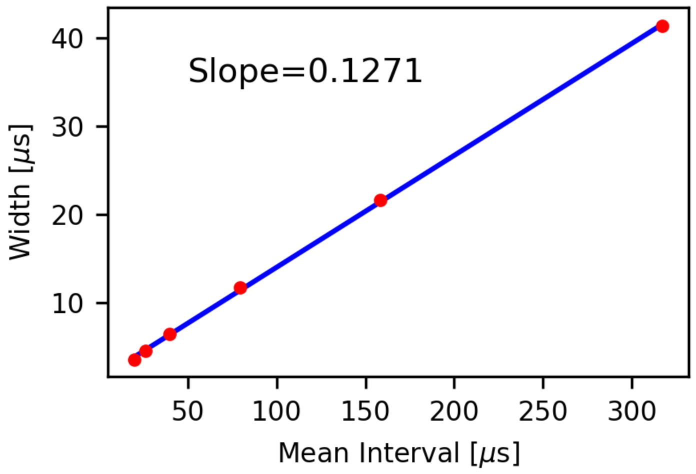

Figure 3.8: The width of the distribution of PSO timing intervals as a function of the mean timing interval.

Table 3.3: Comparison of the measured PSO distances at different stage speeds.

| Speed $[\frac{\mu m}{s}]$ | $PSO_{Measured}$ (±2.0) [pm] |
|---|---|
| 800 | 15.9 |
| 600 | 15.8 |
| 400 | 15.8 |
| 200 | 15.9 |
| 100 | 15.9 |
| 50 | 15.9 |

errors in timing individual PSO pulses.

It is also interesting to note the fluctuation in expected PSO distance for each of the speeds. The product of the mean PSO pulse interval timing with the commanded speed of the stage gives an average PSO distance. The variation in this value across different stage speeds is indicative of either an inconsistency in the PSO itself or a failure of the stage to move constantly at the commanded speed. Table 3.3 shows the different values for PSO, which are all expected to be equal to the default value of 15.82 pm. This significant uncertainty in PSO pulse interval timing makes the calculated PSO distances equally uncertain.

It remains unclear whether the velocity of the stage was responsible for the errors, or whether the PSO itself is subject to uncertainty. Filtering the data based on changes in

Table 3.4: Comparison of the fitted stage speeds for eight scans at a commanded velocity of 750 $\mu$m/s. Direction determined by magnitude and direction of change in position.

| Scan Number | Forward Speed [$\mu$m/s] | Backward Speed [$\mu$m/s] | Stationary Speed [nm/s] |
|---|---|---|---|
| 0 | 749.43900(5) | -749.43048(6) | 191.6(3) |
| 1 | 749.44362(5) | -749.43770(6) | -128.0(12) |
| 2 | 749.44082(6) | -749.43400(6) | 38.6(3) |
| 3 | 749.44469(6) | -749.43949(6) | -126.1(12) |
| 4 | 749.43972(5) | -749.43194(5) | 38.7(4) |
| 5 | 749.4360(5) | -749.43572(6) | -123.7(10) |
| 6 | 749.44107(5) | -749.43320(6) | 32.7(3) |
| 7 | 749.44253(5) | -749.43461(6) | -87.0(11) |
| 8 | 749.44126(5) | -749.43478(6) | 53.7(4) |
| Averages | 749.440(2) | -749.435(3) | -32(95) |

position to determine whether the scan was in a forward scan, a reverse scan, or stationary allowed the fitting of straight-lines to the data for a determination of velocity. Fits to the relevant sections of data yielded slopes slightly less than what was commanded as shown in Table 3.4. This may be evidence for deviations in the velocity that could be giving rise to the uncertainty in the timing of PSO pulse intervals. Table 3.4 shows the fitted stage speeds for a trial during which the stage was commanded to travel 750 $\mu$m/s. The fitted velocities differ from what was commanded of the stage. The data were classified into scan directions only by considering the change in position from one point to the next and this shows that during the linear motion the velocity is consistently less than commanded as shown in Table 3.4. The height of the envelope of data in Figure 3.9 however, shows that the instantaneous velocity changes significantly during a scan. The histograms of these data can be seen in Figure 3.10 and indicate a significant spread, and this deviation from linearity in velocity is possibly the cause of uncertainty in timing of PSO pulses. The width of these histograms are approximately 1% of the mean values for the forward and reverse scans. For the stationary scan the mean value is zero so the finite width indicates that there is an issue with position stability even when the stage is not in motion. The uncertainty increases when the stage is in motion which indicates there is both a relative and absolute error in the stage position.

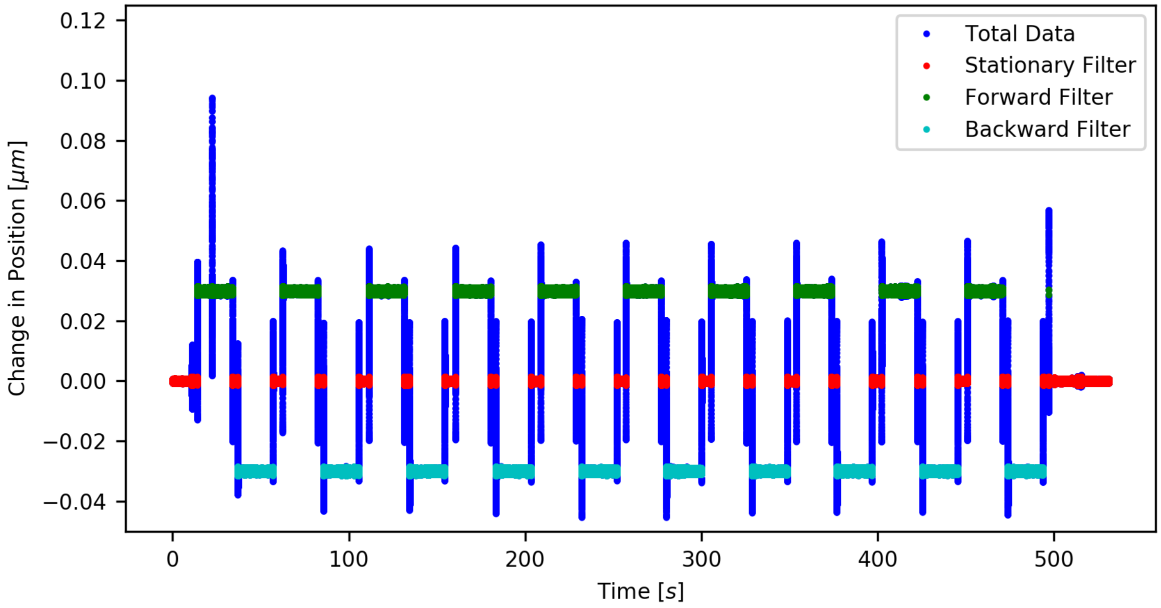

Figure 3.9: Forward, reverse, and stationary classifications of stage speed based on the change in position from one point to the next. Uncovered blue data were not included in any of the classifications.

Given that the widths of the histograms for forward and reverse scans are considerably less than 12.7% of the mean value it is unlikely deviations from linear velocity are responsible for the error in PSO pulse interval timing. The results of these experiments indicate that the uncertainty is in the PSO distance itself, which means that care must be taken in using the PSO interval timing to determine stage position, particularly in future interferometry experiments.

### 3.2.3 Overnight Trials

Though the Aerotech stage enabled the measurement of specific velocities, the residual noise will contain noise arising from the normal motion and operation of the stage and distortions arising from movement of people and items around the lab and building as well as atmospheric turbulence. To get a reliable determination of the noise floor resultant from long-term use of the metrology system the laser was directed at stationary mirrors and left

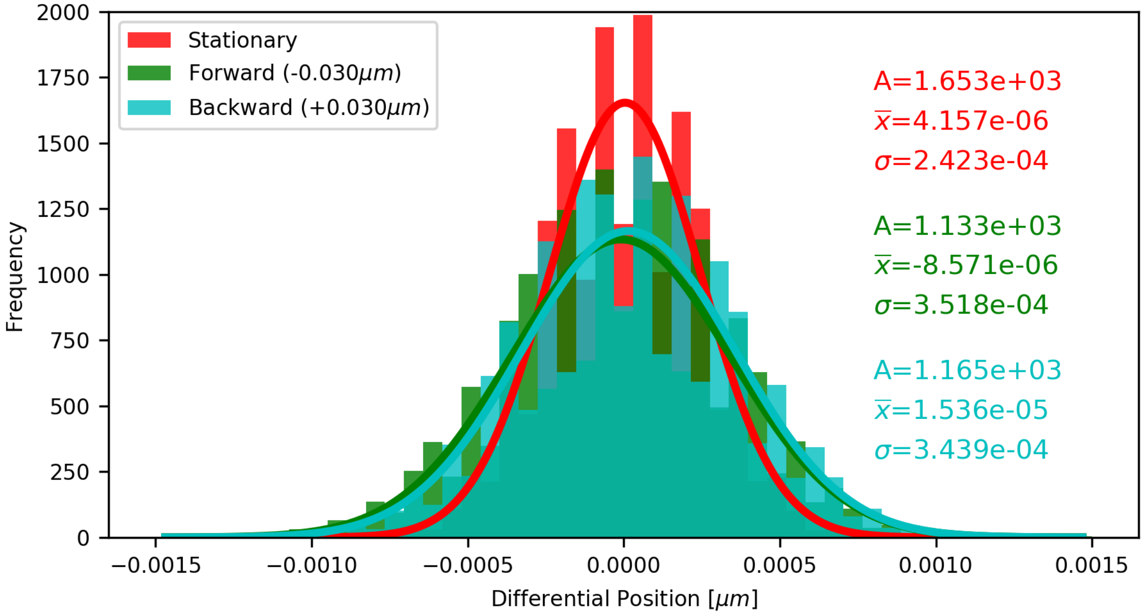

Figure 3.10: Histograms of the change in position for forward, reverse, and stationary classifications of stage motion. The width of each histogram can be taken as an uncertainty in the average change in position, and therefore velocity.

alone overnight.

Results of the overnight trials confirmed the issue of skips in the data, but also include an element of long-term drift not seen in the previous trials. These issues manifested repeatedly across overnight trials, an example of which is shown in Figure 3.11.

The experimental results from leaving the sample overnight prompted an investigation into possible causes of both the skips, and the long-term drift. Although temperature data were typically recorded during such trials, an error in the data collection overnight means that temperature logs for this trial are unavailable. To rule out thermal effects it was decided the sample should be heated and cooled whilst recording temperature and length data to see if small temperature changes could induce these skips.

In the same trial a number of impulses were applied to the sample to test against vibrational effects which may cause the laser to lose alignment. These impulses were meant to

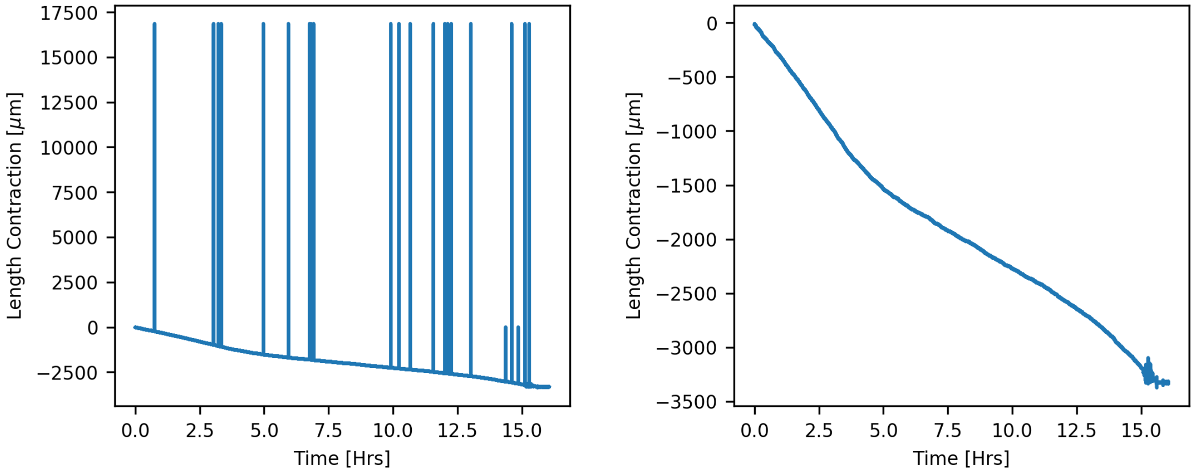

(a) (b)

Figure 3.11: Results of metrology system measurements taken overnight with retro-reflectors affixed to a CFRP sample. (a) Unfiltered data showing seemingly random skips in the distance measurement. Note that the skips differ in their magnitude, and return to the curve, unlike those seen in Figure 3.2. (b) Data after skips have been filtered out which still show a considerable drift in the measurement. Jitter at the end is likely the result of entering the room in the morning.

test robustness against normal lab operations and included slamming the door to the lab, stomping beside the table, flicking the retro-reflector mounts with a finger, and rotating the retro-reflectors. Each of these actions was undertaken to affect the alignment of the optics and ensure that the skips weren't being caused by vibrations in the system or other external factors.

Results of these tests are shown in Figure 3.12 and seem to indicate that strong impulses would cause the metrology system to lose track of home and replicate the 'skips' seen in previous data sets. This did not solve the problem of skips seen in the overnight trials, nor the drift, however, as the skips caused by impulses to the system are relatively small. While thermal cycling of the sample did cause an increase in the noise floor of the metrology system it did not replicate any of the skips or the drift in the metrology system observed in the longer trials. The increase in the noise floor during heating is not a surprise given a convective heat gun was used to heat the sample. The blowing air may cause the sample to vibrate and consequently increases the noise floor by adding jitter. Kapton tape was used to adhere the thermometers and likely contributed to uncertainty in the temperature measurements.

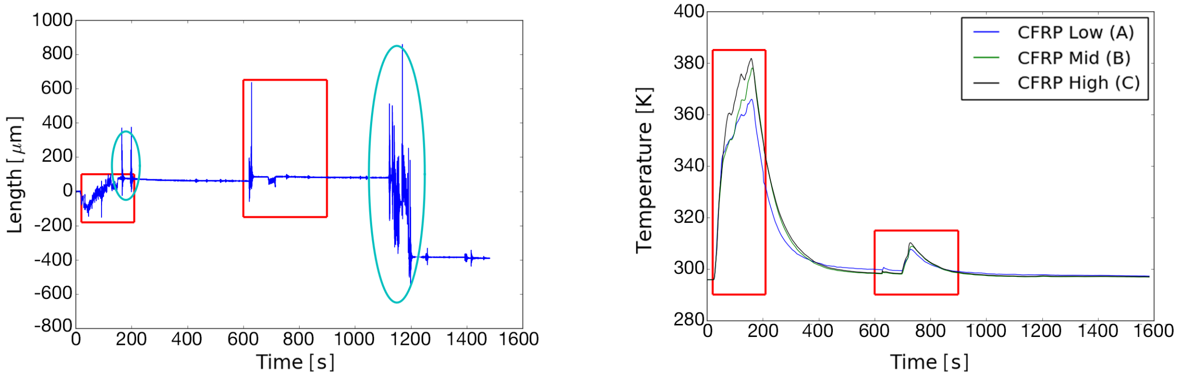

(a) (b)

Figure 3.12: Demonstration of the inability of the metrology system to re-home after a substantial impulse. (a) Length recorded by the metrology system whilst being agitated by heating (red), rotation of the retro-reflector, or impulses (cyan) applied to the mounting block for the retro-reflectors. (b) Temperature of the CFRP sample during the trials in which the sample was agitated. Red squares show the periods of heating and match to those seen in panel (a).

The skips and long-term drift observed in overnight trials could not be explained by minor impulses or thermal fluctuations resultant from climate control in the lab. This prompted questioning about whether the Eblana laser had been mode-hopping, which could be a potential cause of the skips in recorded length. Though the temperature in the lab was within the operable range, the temperature during cryostat operation was unknown. If the laser was heating or cooling dramatically it may have been temporarily in-operational, or perhaps even damaged which could explain problems in successive trials.

## 3.3 Laser Temperature

The Eblana used for recording distance is servoed to approximately 25°C and if the temperature rises above this the laser may begin to mode-hop. Conversely the laser will no longer be able to provide enough power to maintain its temperature if the heat loss to the environment is greater than the heater power available to servo the temperature. The combination of these effects results in an operable range of temperatures for the metrology system, and it is critical to monitor this temperature to ensure the laser is operating in a reliable manner. The laser operates at approximately room temperature so there's no need for sophisticated thermometry, to monitor this however it must be able to withstand vacuum.

A few varieties of semi-conductor diodes were tested as thermometers, given that their voltage response to temperature is linear in certain regimes. Eventually transistor diodes were chosen because of their consistency and reduced noise-profile relative to the other varieties. A series of calibrations were run in order to determine the best circuit for making the measurements.

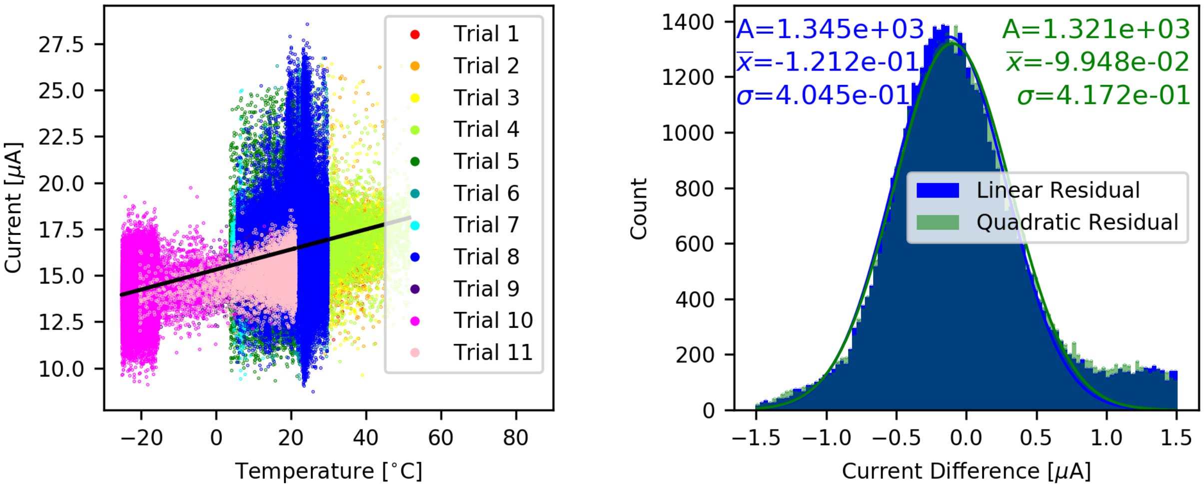

(a) (b)

Figure 3.13: Characterization of current through the circuit for room temperature thermometry. (a) The eleven independent calibration currents plotted as a function of temperature. A linear fit to the data indicates a relationship of $54.1(2)\frac{nA}{K}$. (b) The histogram of the residual current after subtracting both a linear and quadratic fit.

Since the measured quantity in calibrating thermometry is the voltage drop across a diode, ensuring current control is important for consistency of results. If the current changes the voltage too will change and this could be incorrectly attributed to a change in temperature. After testing a few different circuits it was found that the most reliable results came when a mega-ohm resistor was used in series with the diodes. This ensured the effective resistance of the circuit changed very little since the resistance of the diodes is much smaller than a mega-ohm.

Though fairly consistent, effective resistance still changed with temperature, and consequently the current also changed with temperature as shown in Figure 3.13. The distribution is a linear profile with random error and a slight right-skew due to the substantial amount of data near room temperature which fall above the straight-line fit. The reason for the large spread close to room temperature is the quantity of data collected near to these temperatures. This level of variability in the current was far less than that found with other circuits though, so the mega-ohm resistor was chosen as the current-control mechanism. The final circuit was rather simple in conception and is shown in Figure 3.14.

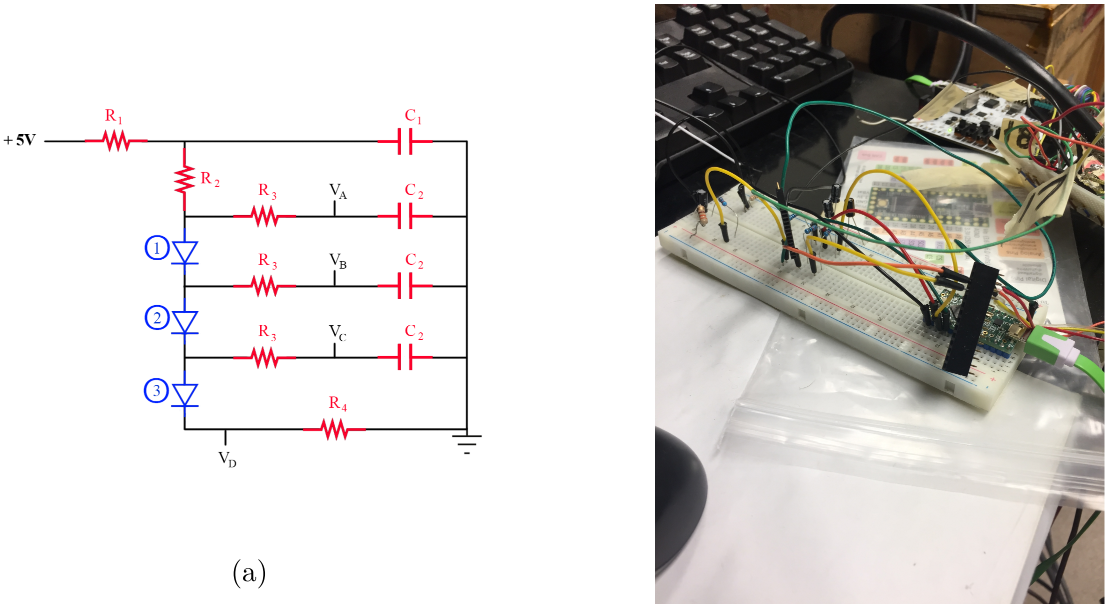

(a)

(b)

Figure 3.14: The circuit diagram and completed circuit for measuring the temperature of the metrology system. (a) Circuit diagram for measuring the voltage drops across three diodes. Voltages are measured at $V_A$, $V_B$, $V_C$, and $V_D$. (b) The completed circuit measuring temperature within the room temperature volume of the cryostat.

Knowing that the current was approximately constant, a Teensy-LC [78] was programmed to regularly measure voltages before and after each diode since the change in voltage across a diode is proportional to the temperature of that diode. The voltage drop was plotted against

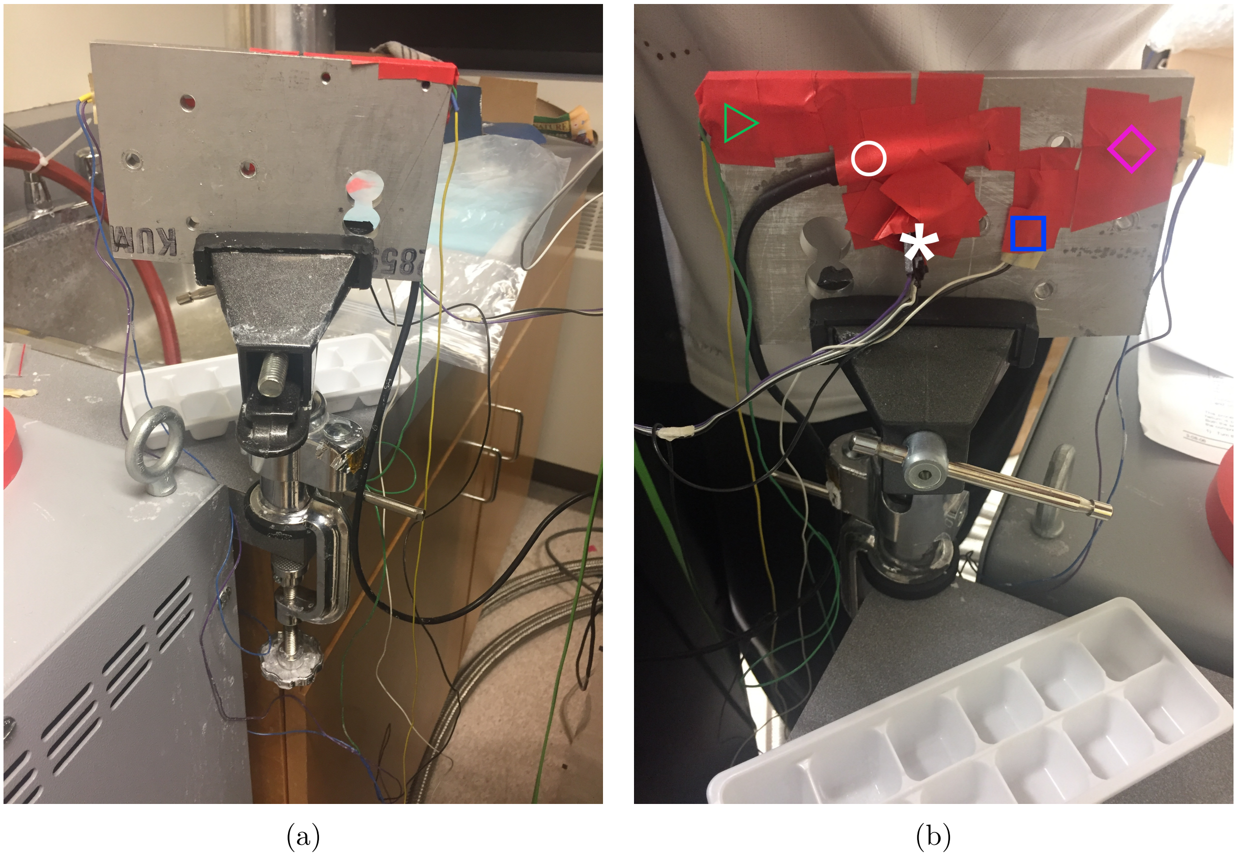

Figure 3.15: The experimental setup used in calibration of diodes for use as thermometers. (a) The front of the aluminium plate used in calibration. (b) The back side of the aluminium plate showing the three diodes (blue square, pink diamond, and green triangle) and the two thermometers used to calibrate them (white circle and star).

the temperature as recorded by an electronic thermometer affixed to a block of aluminium with the diodes. By heating or cooling the front face of the block shown in panel (a) of Figure 3.15 and waiting a short amount of time the diodes and thermometry were able to approach thermal equilibrium. Although it would have been preferred to measure the temperature at physical setpoints like the freezing point and boiling point of water, it proved too difficult to thermalize the aluminium block in a bath whilst keeping the electronics dry, and therefore the temperature measures were still unreliable. To compensate for this uncertainty the temperature was recorded with the two electric thermometers shown in panel (b) of Figure 3.15 and the mean value was used as the true temperature of the sample.

By wiring the power to the circuit and voltage measurements after each diode externally, the temperatures could be recorded and monitored under vacuum from outside the cryostat. A pair of tests were run, one with the laser turned off, and one with the laser turned on. The first trial monitored the environmental temperature during a cool-down, and the second trial looked for a change in temperature associated with the laser in operation. In both tests the three diodes were attached with GE varnish [79] and taped over top in three places:

1. At the back of the mounting plate, near to the spool of fibre-optic cable
2. On the front of the photonics box
3. On the outside of the metal laser housing itself

in hopes that a model for heat transfer into or out of the laser could be modeled. The setup can be seen in Figure 3.16.

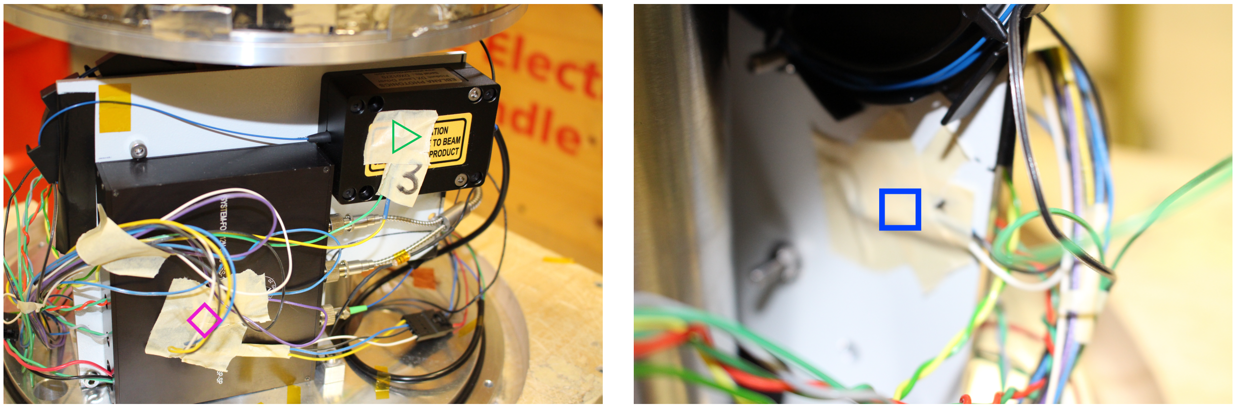

(a) (b)

Figure 3.16: Design for measuring the temperatures of the mounting plate, photonics box, and the laser. (a) The front of the mounting plate inside the room temperature chamber of the cryostat showing diodes #2 (pink diamond), and #3 (green diamond). (b) The back of the mounting plate inside the room temperature chamber of the cryostat showing diode #1 (blue square).

Preliminary testing seemed to indicate a significant thermal gradient across the apparatus as shown in Figure 3.17. At first this was believed to be the result of heat being conducted out via the armoured fibre-optic cable which runs up into the 4 K chamber. Calculating the theoretical heat transfer through the fibre showed that it would be incapable of sufficiently

Table 3.5: Details on each of the experimental setups for measuring temperature of the metrology mount.

| Date | Laser On | Mylar Sheet | Figure 3.17 Panel |
|---|---|---|---|
| October 13th | Y | N | (a) |
| October 19th | N | Y | (b) |
| October 22nd | Y | Y | (c) |

cooling the laser to create the temperature gradient observed. The lack of consistency across the trials coupled with the lack of an explanation for the significant thermal gradients indicated the problem may be with the thermometry itself. Table 3.5 accompanies Figure 3.16 and outlines the differences in experimental setup.

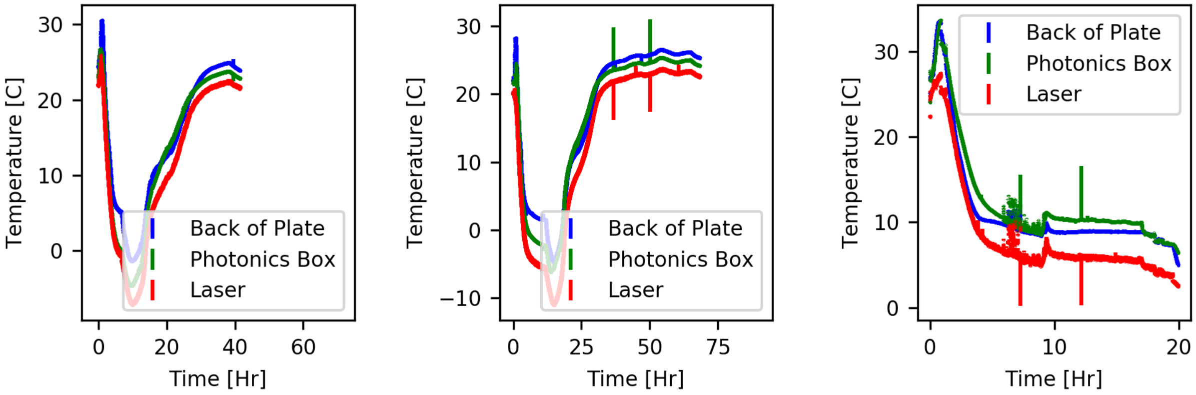

(a) (b) (c)

Figure 3.17: Three separate attempts at measuring the temperature of the mounting plate, photonics box, and laser, as shown in Figure 3.16 during cycle to 4 K. The significant differences in temperature are not expected for a thermally isolated system. (a) October 13th, 2018 with laser turned on. (b) October 19th, 2018 with the laser turned off and a sheet of mylar between the laser and the mounting plate. (c) October 22nd, 2018 with the laser turned on again and a sheet of mylar between the laser and the mounting plate. Data taken in the setup shown in Figure 3.16.

Since the thermometry was calibrated to within approximately 0.4% according to the fit in Figure 3.13 the reported temperatures were reliable to within 1° C. The significant thermal gradient with reliable thermometry raised suspicion about the efficacy of the adhesive varnish so a null test was run with two diodes mechanically clamped to the base plate, and one taped down as was the case for the trial with diodes on the mounting plate. This null test setup can be seen in Figure 3.18.

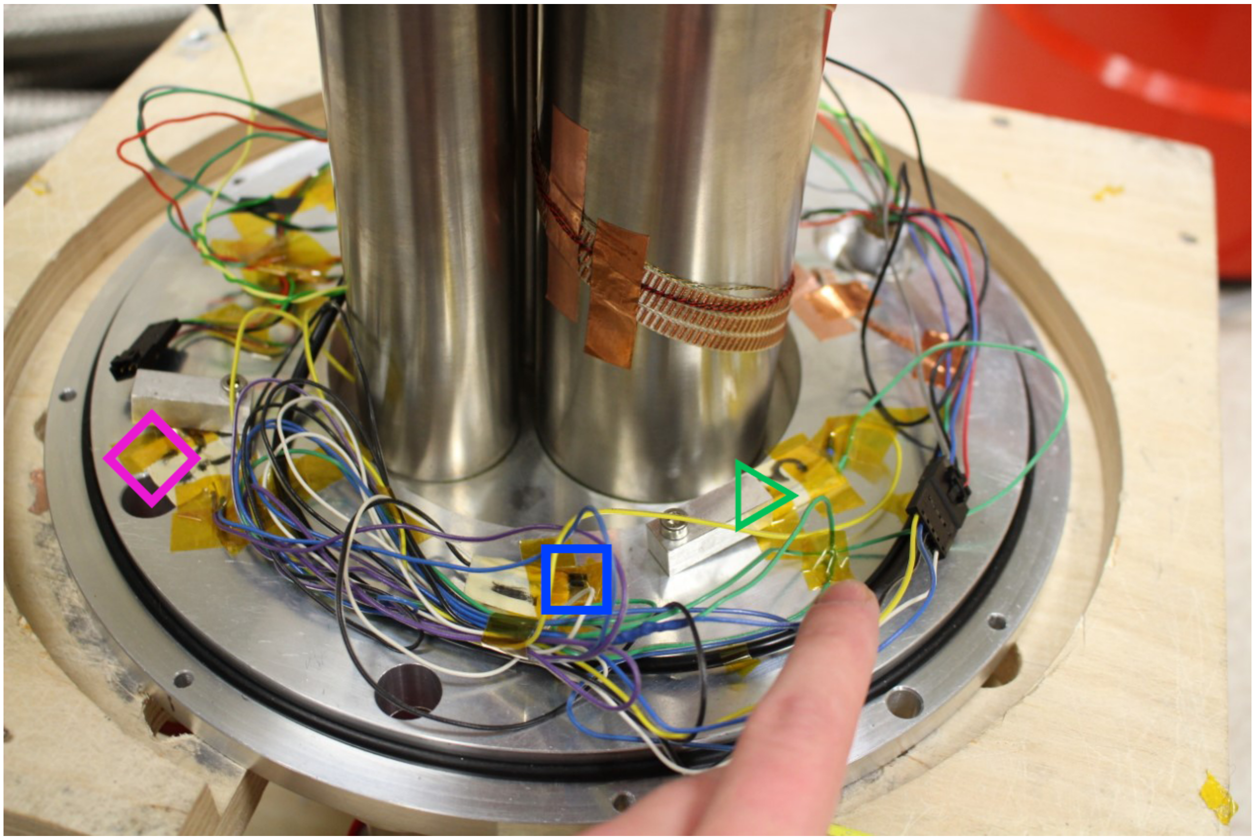

Figure 3.18: The diodes in place for testing of mechanical adhesives. Diodes #2 (pink diamond) and #3 (green triangle) are clamped under aluminium stands for the mounting plate, and diode #1 (blue square) is taped down. The mounting plate, photonics box, and laser were removed to mitigate other sources of heat such as the laser servo.

The results from this null trial are shown in panel (a) of Figure 3.19. The two diodes which were clamped were in very good agreement with one another, and the taped diode was not well-thermalized with the other two. In order to ensure this wasn't by chance, the thermometers were re-arranged and tested again and the results are shown in panel (b) of Figure 3.19. Once more, the two diodes which were clamped showed strong agreement, where the taped diode disagreed.

The results of these two experiments demonstrated that the thermal gradient observed across the mounting plate and laser was likely the result of poor thermal contact, rather than a true difference in temperature. The thermometers were held firmly with thermal varnish

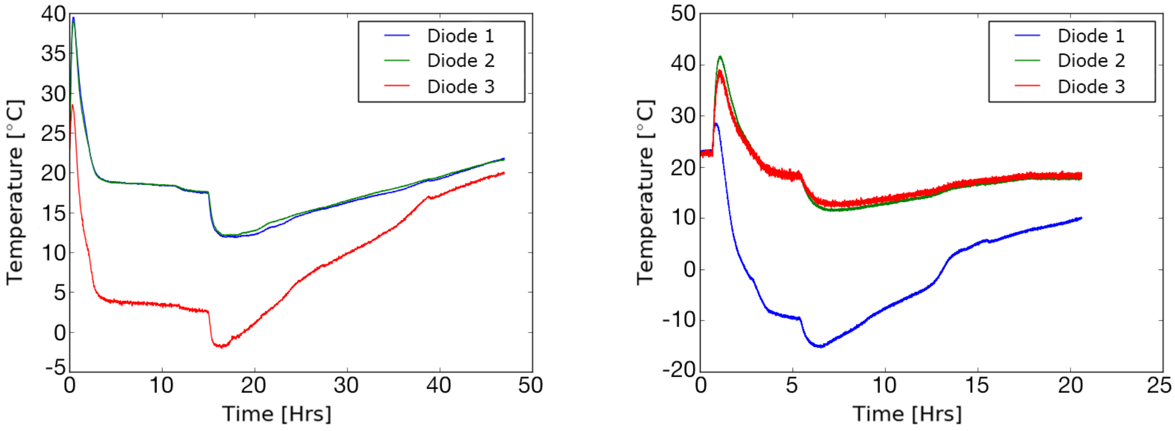

(a)

(b)

Figure 3.19: Diode temperature readings of the base plate in the room temperature chamber of the cryostat while the cryostat was thermally cycled to 4 K. (a) Diodes #2 and #3 clamped. (b) Diodes #1 and #2 clamped.

and should have thermalized. This indicates that accurate measures of the temperature for each component are possible, but depend on strong mechanical contact. These measurements also show that the ambient temperature within the room temperature volume of the cryostat is between approximately 20 C° and 40 C° during normal operation, and may cool to approximately 13 C° when the PTC compressor is turned off.

For future operation of the three-phase metrology system it is important that the temperature of the laser is monitored closely, and that it is insulated from the ambient temperature, particularly in the first few hours of operation when ambient temperature is highest. Insulating the laser from the mounting plate will help to maintain the temperature of the laser within the desired operating range.

## 3.4 Frequency-Modulated Metrology System

The issues faced with the three-phase metrology system were difficult to diagnose and it was decided that the metrology system needed to be changed. In lieu of using two separate paths to obtain a differential measurement, the frequency-modulated metrology system makes use of a modulated laser frequency and a partially reflective beam-splitting fibre tip

[80]. The two beam paths become the half of the incident light reflected back at the tip, and the half which is transmitted and travels the length of the apparatus before being reflected back to the fibre tip [80]. The schematic diagram for the metrology system can be seen in Figure 3.20.

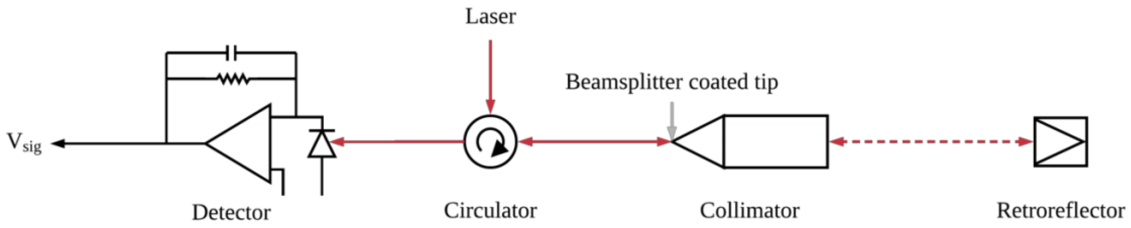

Figure 3.20: Schematic representation of the optical path within the frequency modulated metrology system. Figure Source: Christiansen et al. [80].

Comparison with the schematic diagram of the three-phase metrology system (see Figure 3.1) shows the significant simplification in circuitry. The simplification of the metrology circuit comes with a few drawbacks. The loss of differential measurements from either end of the sample means that other components in the apparatus need to be calibrated out. The modulation of the frequency also means that the optical path length is constrained and adjusting the system to measure drastically different lengths requires additional effort.

Despite the drawbacks of this frequency-modulated metrology system, preliminary results on the precision of the frequency-modulated system are promising. Figure 3.21 shows the movement of a piezo stage as tracked by the frequency-modulated system. The residual was not purely random noise and as a result the histogram of this data is not Gaussian in shape. Unfortunately, accompanying data for the piezo stage are not available, so it is not possible to determine whether these deviations are the result of a failure in the metrology system or the inadequacy of a sinusoidal oscillation to describe the true motion of the stage.

The problems of skips and the long term drift seen in the three-phase system did not appear in the short calibration trial for the frequency modulated system. An RMS value of 141.9 nm means that the precision of the system is sufficient to justify measurements of

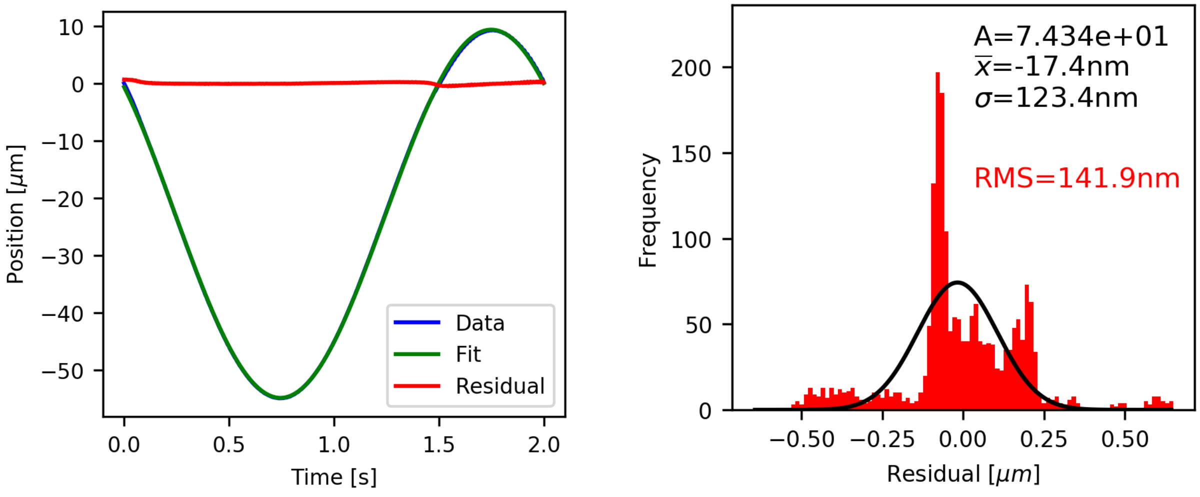

(a)

(b)

Figure 3.21: Determination of the precision of the frequency-modulated system by comparison with a piezo stage. (a) Position data recorded with the frequency-modulated laser metrology system of a sinusoidally oscillating piezo stage. A sinusoidal fit to the data and the residual are shown. (b) Histogram of the residual shown in panel (a). Parameters for the Gaussian fit to the histogram are shown in black, with the root mean square (RMS) of the residual shown in red.

CTE. Extra care will be needed to understand experimental results, however, as the fully differential measurement no longer incorporates the sample jig, meaning that contraction of the collimator and the mounting apparatus will all contribute to changes in position in the data.

## 3.5 Conclusion

The characterization of two separate nanometer precision laser metrology systems has shown that for short-distance measurements the frequency modulated system is more reliable than the three-phase system.

The three-phase system suffers from unexplained long-term drift and sudden skips in the data equivalent to integer wavelength counts. These errors make the three-phase system unpredictable. Despite the unpredictable nature of the three-phase system it is still capable of high-precision measurements provided more is done to understand the causes of the skips and drift. Temperature control measurements have been implemented to ensure the laser operates within the correct range of temperatures, but temperature itself has not been correlated with the errors.

These two systems may be used to determine the CTE of materials like CFRP, and in order to guarantee the reliability of their measurements they will first measure the CTE of a well-characterized material, aluminium. To make these measurements rapidly and effectively requires thoughtful design of a dedicated apparatus for consistent and repeatable experiments and this is expanded on in Chapter 4.

# Chapter 4

# Design of Cryogenic Experiments

To view the cold dense clouds of molecular gas in which star formation takes place requires extremely sensitive detectors, and cryogenically cooled optics. One concern about actively cooling optical components is that mounting structures for those optics will necessarily also cool. Mounting structures made of materials different from any optical components will result in differential contraction at any material interface as the system is cooled, and as a result the optics may become warped. Any significant amount of warping in the optics would constitute a critical failure as the alignment is lost and images aren't focused (as a rule of thumb, distortions about surface flatness should be less than $\frac{\lambda}{10}$ [32], or $\sim 3\,\mu$m in the FIR). Because of the differential contraction, it is crucial that cryogenically cooled imaging optics are designed to be in focus operational temperatures, which may result in poor alignment at room temperature.

The precision required for well-focused images means that the coefficient of thermal expansion must be known precisely for both the reflective surface of the mirror and the substrate to which the surface is mounted across the entire temperature range. It is also important that the optics are thermally isolated from heat loads in order to minimize the rate of cryogen use and extend the duration of telescope operation. The material also needs to be strong enough to support the weight of optics during launch, and preferably lightweight in the case of space-borne instrumentation to reduce the fuel expenditure in launching and repositioning the telescope.

To have all the desired physical qualities it is often best to use composite materials.

Composite materials consist of more than one material which are designed to have the beneficial physical properties of constituent materials when combined. One example of a class of composite materials which has been used for mounting cryogen tanks on-board spacecraft [81] are carbon-fibre reinforced polymers (CFRPs).

## 4.1 Carbon-Fibre Reinforced Polymers

CFRPs are composite materials which consist of layers of polymer resins reinforced with carbon fibres. The carbon fibres provide structural stability and their number density and orientation within the material can be used to generate anisotropic physical properties. This means the method by which these CFRP samples are manufactured will affect the physical properties of the material. For instance, carbon fibres oppose contraction such that the CTE along an axis parallel to the fibres will be smaller than that along the axis perpendicular to the fibres. If this relationship is well understood, samples could in principal be manufactured for specific behaviour. In the case of an optical substrate, an isotropic coefficient of thermal expansion (CTE) is important for symmetric distortions. For thermally isolating components, a low thermal conductivity along a given axis would be advantageous.

CFRPs represent a particularly interesting set of candidate materials for constructing optical mounts on-board spacecraft due to their manipulable physical properties. CFRPs are both structurally stable and light-weight, making them relatively cheap to transport. In addition to their structural stability CFRPs are good thermal insulators, which means they could be effective in thermally isolating optical components at cryogenic temperatures [81]. Although it is known that the CTE for CFRPs is small [82], it is not well-characterized across the entire range of temperatures from room temperature to 4 K (boiling point of liquid helium, a common cryogen) to be used reliably for optical components. Some methods for determining the CTE and thermal conductivity of CFRP more precisely have been proposed and attempted, and the results are presented in this chapter.

Experiments were performed on CFRP with three different fibre layouts which are de-

Table 4.1: Fibre orientations for the different configurations of CFRP. Table acquired from Spencer et al. 2018 [72].

| Configuration | Layer Orientation (fibre axis angle with respect to length axis) |
|---|---|
| Quasi-Isotropic | 0° / 45° / 90° / -45° / -45° / 90° / 45° / 0° |
| Orthogonal | 90° / 90° / 0° / 90° / 90° / 0° / 90° / 90° |
| Parallel | 0° / 0° / 90° / 0° / 0° / 90° / 0° / 0° |

scribed in Table 4.1. The first samples tested are 'quasi-isotropic' and may be seen in panels (a) and (b) of Figure 4.8 in Section 4.4. The next layout to be tested was one in the orthogonal configuration in order to maximize the CTE. Unfortunately length measurements for this orientation were unsuccessful, and have been omitted. The final tests were conducted using a sample of CFRP in parallel configuration. The results of these measurements are presented in Figure 4.21 in Section 4.5.

The CFRP samples of interest in this study are rectangular sheets, 140 mm long, 50 mm wide, and 1.25 mm thick. An aluminium sample of approximately the same dimensions was machined in order to compare experimental data against well documented values, allowing removal of systematics in the experiment. Measuring the physical properties of CFRPs will necessitate carefully considered experimental design, motivated by an understanding of the underlying physics which gives rise to the phenomena of interest.

## 4.2 Thermal Properties of Solids

In order to probe the physical properties of a material at cryogenic temperatures it is important to have an understanding of the phenomena which give rise to those properties, and how the phenomena relate to temperature. Thermal capacity, thermal conductance, and thermal expansion will be explored in this section. Developing an understanding of how properties like thermal conductance and the CTE manifest will help to motivate the experimental designs used to probe them. Following an introduction to the theory, an explanation of the experiments designed to probe thermal conductance and the CTE of

Table 4.2: Terminology, and units for the various expressions of specific heat.

| Term | Units |
|---|---|
| Specific heat | $\frac{J}{kg \cdot K}$ |
| Volumetric heat capacity | $\frac{J}{m^3 \cdot K}$ |
| Molar heat capacity | $\frac{J}{mol \cdot K}$ |
| Heat Capacity | $\frac{J}{K}$ |

aluminium and CFRPs will follow, along with experimental results where applicable.

### 4.2.1 Thermal Capacity of Solids

The mechanisms for heat exchange through a solid depend on the material of interest, and the dominance of each mechanism will depend on the temperature. In order to understand the means by which a solid may transfer heat, it is important to first understand how a solid stores heat, and how that heat relates to temperature. The specific heat of a material is a measure of how much thermal energy is required to induce a change in temperature. There are a number of different expressions for this quantity as seen in Table 4.2, but all are approximately equivalent since the number of moles determines the mass. Since volume is temperature dependent it is not directly determined by the number of moles, so volumetric heat capacity will depend differently on temperature than the other expressions of specific heat.

Classical models of heat capacity rely on adding up the degrees of freedom and using the equipartition theorem, which says each degree of freedom gets an average $\frac{1}{2}k_BT$ thermal energy [83]. For a typical solid the atoms have six vibrational degrees of freedom, three kinetic and three potential. Conduction electrons will also contribute to the heat capacity if present, and contribute a further three translational degrees of freedom. In this case the molar heat capacity would be given by [83]

$$C_V = \left(\frac{\partial E}{\partial T}\right)_V = 3N_a k_B + \frac{3}{2}N_e k_B \quad [\text{J K}^{-1}], \tag{4.1}$$

where $N_a$ and $N_e$ represent the number density of atoms and electrons respectively [83]. However, at low temperatures the molar heat capacity is measured to be less than the classical predictions. This disparity is due to quantum effects not accounted for by classical models. Since energy levels are quantized, many phonons are in their lowest energy state at very low temperatures, reducing the effective degrees of freedom.

An important change to the model of molar heat capacity came about with the advent of the *Debye* model, which treats phonons in the solid as a gas. A phonon is a vibration in the crystal-lattice of a solid, and it is the frequency of these vibrations which determine the amount of energy the phonon has. The effect of phonons on molar heat capacity, $C_V$, is approximately given by the Debye function [84],

$$C_V = 9\,N_A\,k_B \left(\frac{T}{\theta_D}\right)^3 \int_0^{\theta_D/T} x^4\,e^x\,(e^x-1)^{-2}dx \quad [\tfrac{J}{mol\cdot K}], \tag{4.2}$$

where $\theta_D$ is the material-dependent Debye temperature, and $x = \frac{h\,\nu}{k_B\,T}$. Equation 4.2 gives a good approximation over most of the range of temperatures from room temperature to cryogenic temperatures, and recovers the low and high temperature approximations.

The integral is often challenging to calculate at intermediate temperatures but recovers the expected values at high and low temperatures. For high temperatures the contributions from phonons dominate [84],

$$C_V = 3N_A k_B \quad [\tfrac{J}{mol\cdot K}], \tag{4.3}$$

and at low temperatures the contribution is [84]

$$C_V = K_1 T^3 \quad [\tfrac{J}{mol\cdot K}], \tag{4.4}$$

where [83] [84]

$$K_1 = \frac{12 N_A \pi^4 k_B^4}{5\epsilon_D^3} \approx 1944 \quad [\tfrac{J}{mol\cdot K^4}], \tag{4.5}$$

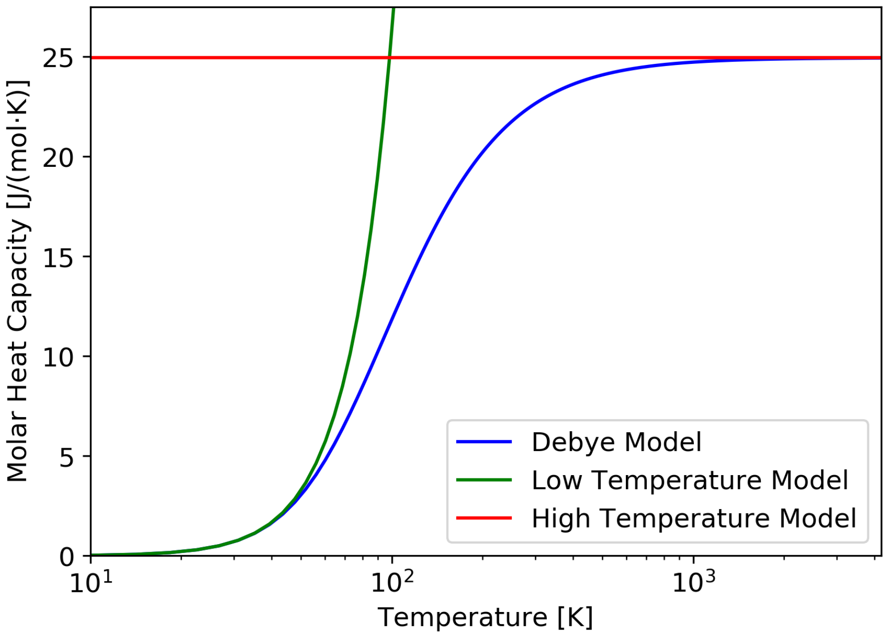

Figure 4.1: The theoretical curves in the low, high, and intermediate temperature ranges for molar heat capacity using $\theta_D$=428 K [85] for aluminium.

and $\epsilon_D$ is the Debye cutoff energy [83],

$$\epsilon_D = k_B \theta_D \quad [\mathrm{J}]. \tag{4.6}$$

The cutoff energy is a result of the minimum wavelength of two times the atomic separation in the lattice. A minimum wavelength corresponds to a maximum frequency, and in turn a maximum energy [83].

At very low temperatures the contribution from conduction electrons becomes dominant in conductors as it is linear in $T$, whereas the contribution from phonons goes to zero as $T^3$ [84]. The molar heat capacity approaches linearity at very low temperature since the electronic contribution at low-temperatures is [86]

$$C_e = c_D T \quad [\frac{J}{mol \cdot K}], \tag{4.7}$$

where $c_D$ is a material-dependent constant. The combination of all the different contributions makes it very challenging to predict thermal properties from theory, and it is best to determine experimentally rather than theoretically. The phenomena which store energy such as phonons and conduction electrons are also responsible for energy transfer through a material, and are important for the thermal conductivity of a material.

### 4.2.2 Thermal Conductivity of Solids

Thermal conductivity is an expression of how well a material conducts or transfers heat in units of $[\frac{W}{m \cdot K}]$. The amount of heat conducted through a solid depends on the dimensions of the sample, but also depends importantly on the thermal conductivity. Fourier's Law of heat conduction gives an expression for the heat flux, $q$, through a material as a function of the thermal gradient and the thermal conductivity, $\kappa$ [87],

$$\vec{q} = -\kappa \nabla T \quad [\mathrm{Wm^{-2}}], \tag{4.8}$$

where $\nabla$ is the del operator. To get from heat flux, $q$, to heat conducted through the cross-section of material, $Q$, per unit time requires integrating the flux over the area of the cross-section of the material, $A_{CS}$ [88],

$$\frac{\partial Q}{\partial t} = -\iint \kappa(T) \nabla T \cdot d\vec{A_{CS}} \quad [\mathrm{W}]. \tag{4.9}$$

In a Cartesian coordinate system the material can be imagined to be oriented along the $x$-axis, with it's cross-section in the $y$-$z$-plane. In the case of a uni-directional temperature gradient in the $x$-direction the $y$ and $z$ components of $\nabla \vec{T}$ go to zero and the equation reduces to [88]

$$\dot{Q} = -\iint \kappa(T) \frac{\partial T}{\partial x} \cdot dA_{CS} \quad [\mathrm{W}], \tag{4.10}$$

where $\dot{Q} \equiv \frac{\partial Q}{\partial t}$. Provided the material of interest is homogeneous the surface integral solves simply to [89]

$$\dot{Q} = -A_{CS} \kappa(T) \frac{\partial T}{\partial x} \quad [\mathrm{W}]. \tag{4.11}$$

If thermal conductivity were constant through the sample then the temperature gradient could be simplified to $\frac{\Delta T}{\Delta x}$, and the equation would become [90]

$$\dot{Q} = -A_{CS}\kappa\frac{\Delta T}{L} \quad [\mathrm{W}], \tag{4.12}$$

where $L = \Delta x$ is the axial length of the sample. However, since thermal conductivity is a function of temperature the thermal gradient implies that thermal conductivity will be different through the material. In this case it is convenient to define an average thermal conductivity, $\overline{\kappa}$ [89],

$$\overline{\kappa} = \frac{1}{\Delta T}\int_{T_C}^{T_H} \kappa(T)dT \quad [\mathrm{Wm^{-1}K^{-1}}]. \tag{4.13}$$

The limits of the integral correspond to the temperature at either end of the material. Replacing $\kappa$ in Equation 4.12 with the expression for $\overline{\kappa}$ in Equation 4.13 we arrive at the expression [89]

$$\dot{Q} = -\frac{A_{CS}}{L}\int_{T_C}^{T_H} \kappa(T)dT \quad [\mathrm{W}]. \tag{4.14}$$

Assuming that heat transfer obeys Equation 4.14, it is possible to solve for $\kappa$(T) by rearranging the equation and assuming that the differential element of temperature may be approximated as a simple difference as [91]

$$\kappa(T) = \frac{\dot{Q}_{Sample}L}{A_{CS}(T_{Top} - T_{Base})} \quad [\mathrm{Wm^{-1}K^{-1}}]. \tag{4.15}$$

In Equation 4.15, $\dot{Q}_{Sample}$ is the net heat flux (injected-lost) to the sample, and is taken to be flowing through the sample. If the thermal gradient is small then this provides a means of experimentally determining the thermal conductivity of a sample provided the dimensions and temperature of either end of the sample are known precisely.

The functional relationship for thermal conductivity is material-dependent and for copper and aluminium the National Institute of Standards and Technology (NIST) database [92] uses different, complicated functions for analytical expressions. For example, the functions used to describe the thermal conductivity and specific heat of 6061-T6 aluminium are of the form [92]

$$y(T) = 10^{\sum_1^9 c_i (log_{10}(T))^i}, \tag{4.16}$$

where $y(T)$ can represent either the thermal conductivity or the specific heat depending on the values of the coefficients. These approximations are useful but often fail to match the experimentally determined values and therefore it is best to measure the properties rather than try to predict them from theory.

Although the cross-sectional area and length are treated as constant with respect to temperature in Equation 4.14, it is important to recognize that the dimensions of a solid-state material are not independent of temperature. As previously mentioned the dimensions of materials will change with temperature and differential contraction occurs at the interface of different materials. Understanding the manner in which temperature affects the physical dimensions of a substance is pivotal, particularly when the material may give rise to differential contraction.

### 4.2.3 Thermal Expansion of Solids

Under the conditions of standard ambient temperature and pressure the coefficient of thermal expansion of solids is approximately constant, but this behaviour breaks down when cooling to cryogenic temperatures. Since the CFRP samples will be cooled to cryogenic temperatures if used in space-based projects the linear approximation will be of little help. Given the interplay of different components it can be difficult to predict the contraction of CFRP samples with differing fibre orientations. This means that the best method to determine the CTE is using experimental results over multiple thermal cycles to ensure consistency and repeatability Let us define the quantity of thermal contraction relative to the length at room temperature [89]

$$\frac{\Delta L}{L} = \frac{L_T - L_{293}}{L_{293}}, \tag{4.17}$$

where $L_T$ represents the length at a given temperature, and $L_{293}$ signifies the length at room temperature (293 K).

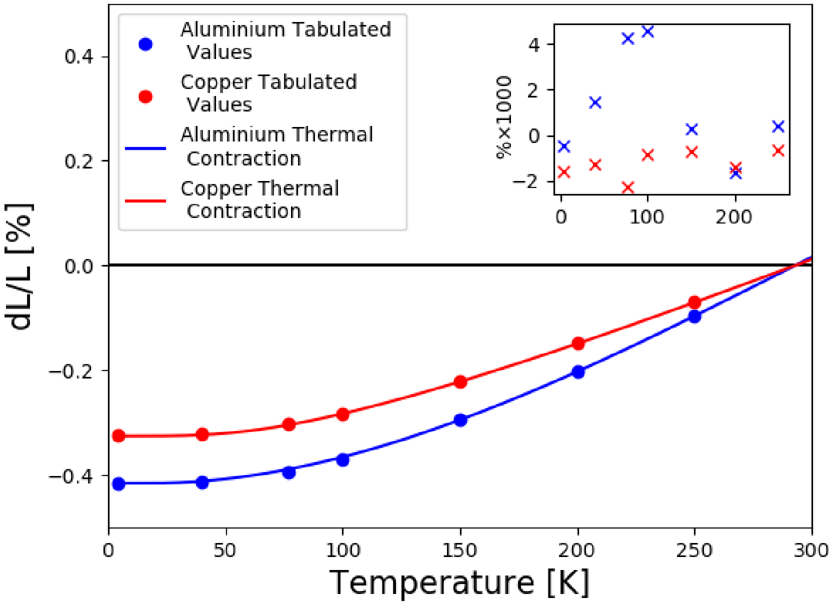

Figure 4.2: Analytical functions for predicted contraction of aluminium and copper from room temperature down to cryogenic temperatures. The inset shows the residuals between the analytical function and the experimental values. Tabulated values from Ekin [89], analytical model from NIST [92].

The analytical function in Figure 4.2 for aluminium is a fourth-order polynomial fit, and will serve as the benchmark against which experimental data are compared. The CTE, $\alpha$, is the rate of the change in length with respect to temperature [89]

$$\alpha = \left(\frac{1}{dT}\right)\left(\frac{dL}{L(T)}\right) = \left(\frac{1}{L(T)}\right)\left(\frac{dL}{dT}\right) \quad [\mathrm{K}^{-1}]. \tag{4.18}$$

Equation 4.18 is graphically represented by the slope of the curves in Figure 4.2, and it is apparent that the value is near-constant around room temperature, and approaches zero as the temperature goes to absolute zero.

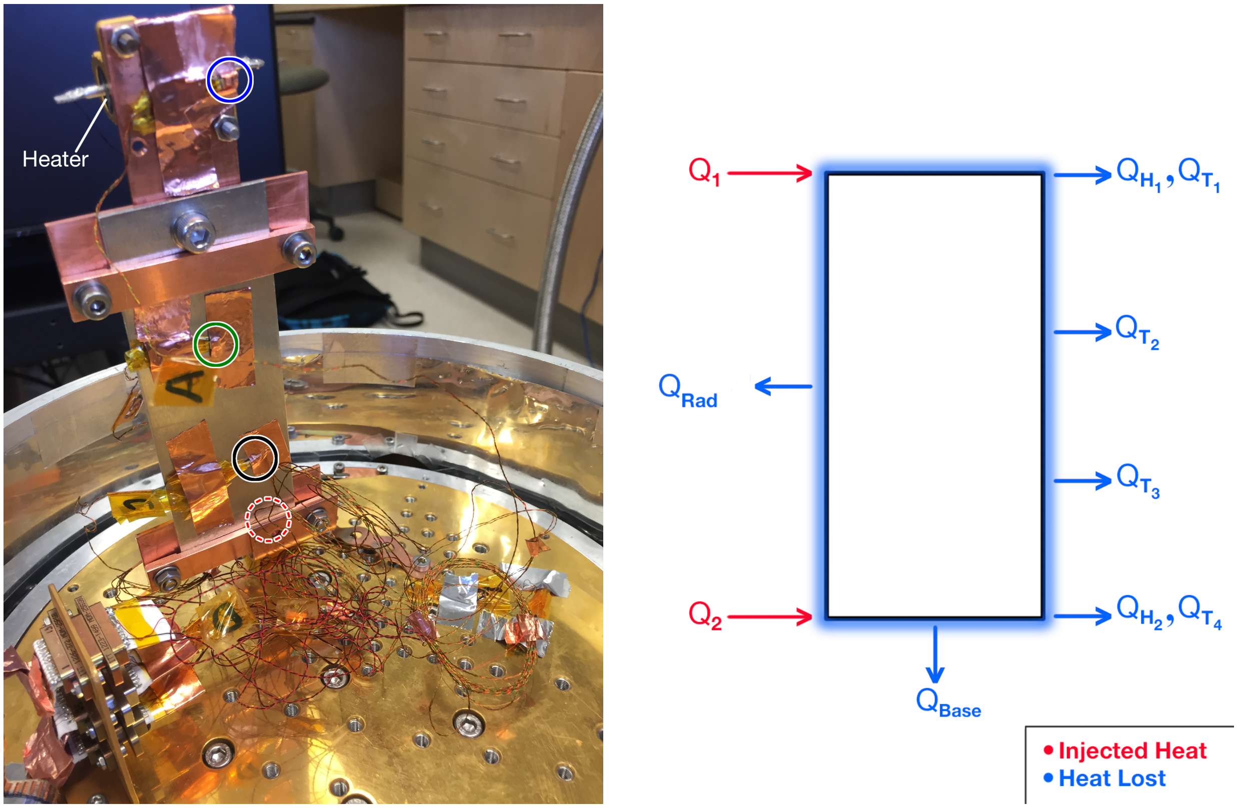

(a) (b)

Figure 4.3: Experimental and conceptual model for thermal conductivity measurement. (a) The apparatus used in measuring thermal conductivity of aluminium. Thermometers A through D are shown with circles of colours blue, green, black, and red respectively. Thermometer D is out of view, along with heater 2, and labeled with a dashed line. (b) Qualitative diagram of the thermal pathways. Heat is injected at one of the two heaters. Heat is lost to the cold plate through the base and by wiring to the two heaters and four thermometers, as well as through radiative losses.

## 4.3 Measuring Thermal Conductivity

In order to measure the thermal conductivity of any material at cryogenic temperatures it is important that the sample be thermally insulated well enough that injected heat does not sink immediately to the cold plate. Two techniques were used to measure the thermal conductivity of aluminium and CFRP. The first method is the more simple experimental setup, though less precise than the second, but easier to implement. The first method was to inject heat only into the end of the sample farthest from the cold plate (known as the ‘floating end’) and measure the temperature gradient across the sample to determine how the heat flows. The second method involved fixing the temperature at both ends of the sample at different “setpoint” temperatures by injecting heat at a constant rate into either end of the material and observing the resultant equilibrium thermal gradient across the sample (see Figure 4.3). The heat flow through the sample is easily calculated by taking the difference between the power input to the sample and the heat lost to the cold plate via the mechanical mount and by wires to heaters and thermometers. The heat conduction through the wires and base of the mount was calculated using Equation 4.14. This calculation required the cross-sectional area for each of the wires, which was calculated based upon their gauge. It also required the length of wire between the cold plate and the sample which was measured to be roughly 30 cm for each wire. The wires were allowed to hang during experimentation and may have made contact with the cold plate so this value is an upper limit. Heat transfer through the base of the mount was much easier to calculate as the dimensions of the bolt which separated the mount from the cold plate could be measured directly and was 2 cm long with a cross-sectional area of 8.8 $\text{mm}^2$. The thermal conductivities for stainless steel (bolt), phosphour bronze (thermometry), and copper (heaters) are well tabulated values so the heat conduction was solved at each instance and subtracted from the heat input by the heaters.

Unfortunately many of these experiments were unsuccessful as seen in panel (c) of Figures 4.5 and 4.6. It is believed that the difficulty in modeling the heat transfer arose due to the choice of adhesives for the thermometry. Copper tape was used to secure the thermometry and this may have modified the thermal path, particularly at cryogenic temperatures where the thermal conductivity of copper is far greater than that of aluminium as shown in panel (b) of Figure 4.4.

Copper is always a stronger thermal conductor than aluminium but once temperatures drop below 100 K the thermal conductivity of copper rises very sharply. This means that as the sample cooled, the tape would have a relatively stronger influence over the transfer of heat. This may contribute to the results of the first round of experiments. Only the heater at the floating end of the sample was active, and dynamic measurements were made as the sample warmed, the results of which are shown in Figure 4.5

Through conservation of energy we know that the heat through the sample will be the difference between the heat input, and that lost through radiation and conduction out through each of the components as

$$\dot{Q}_{Sample} = \dot{Q}_{In} - \dot{Q}_{Out} \quad [\mathrm{W}], \tag{4.19}$$

where

$$\dot{Q}_{In} = \dot{Q}_{Heat1} + \dot{Q}_{Heat2} \quad [\mathrm{W}], \tag{4.20}$$

and

$$\dot{Q}_{Out} = \dot{Q}_{Wire_{H1}} + \dot{Q}_{Wire_{H2}} + \dot{Q}_{Wire_{T1}} + \dot{Q}_{Wire_{T2}} + \dot{Q}_{Wire_{T3}} + \dot{Q}_{Wire_{T4}} + \dot{Q}_{Base} + \dot{Q}_{Rad} \quad [\mathrm{W}]. \tag{4.21}$$

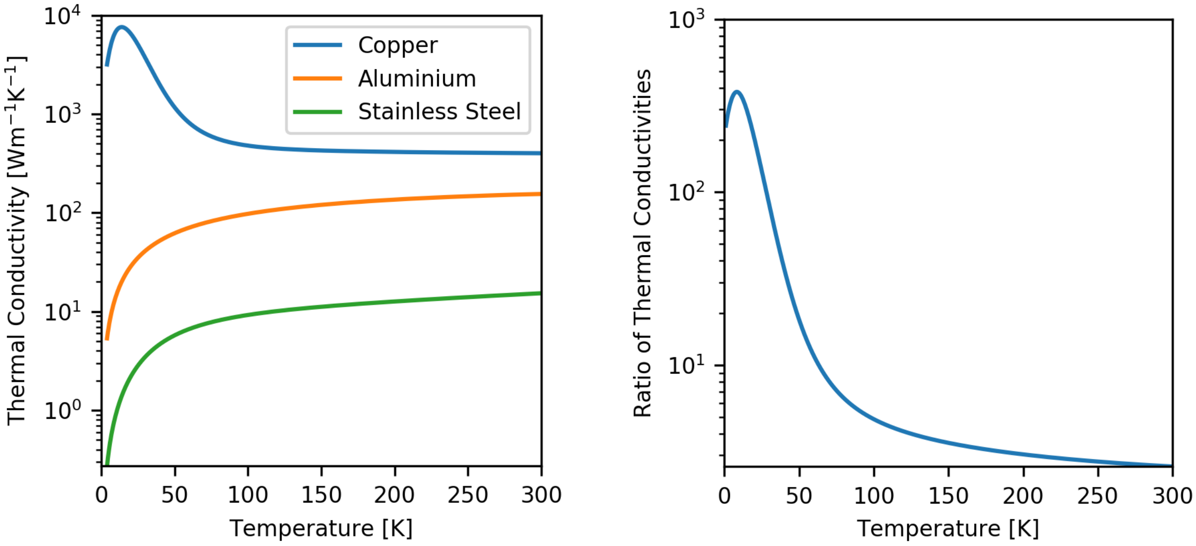

(a) (b)

Figure 4.4: Theoretical curves for thermal conductivity. The canonical curves for thermal conductivity of stainless steel, aluminium, and copper (a), as well as the relative difference between copper and aluminium (b). Functional relationships obtained from NIST [92].

To treat the radiative heat transfer the expression [88]

$$\dot{Q}_{Rad} = \mathcal{A}\frac{\varepsilon_1\varepsilon_2}{\varepsilon_1+\varepsilon_2-\varepsilon_1\varepsilon_2}\sigma_{SB}\left(T_1^4-T_2^4\right), \tag{4.22}$$

is used, where $\varepsilon$ denotes the emissivity of either surface, $\sigma_{SB}$ is the Stefan-Boltzmann constant, and $\mathcal{A}$ is the area of the emitting surface.

In the first case $Q_{Heat2}$=0, and results were fairly close to the accepted values of thermal conductivity for aluminium after the mean temperature rose above approximately 75 K, as the data show in panel (c) of Figure 4.5. Of course these results depend on the assumption that $dT$ can be treated as $(T_{Top} - T_{Base})$ which in turn depends on the difference in temperature being very small, and this isn't the case when the heat is input through only one end of the sample as seen in panel (a) of Figure 4.5.

The data in Figure 4.5 were recorded continually as the heater at the top of the sample was set to a constant input. In an effort to make more precise measurements it was decided that static measurements would be more consistent so the experiment was modified to allow control over the temperature gradient. Setpoint temperatures were defined for both of the heaters, and proportional-integral-derivative (PID) controllers modified the voltage across each heater until both temperatures were stable. Once the temperatures were stable the heaters were commanded to wait a given amount of time before stepping up to the next setpoint temperature. The objective in this procedure was that static temperatures and heat inputs make the calculation a far more dependable description of the physics, and the assumption $dT \approxeq (T_{Top} - T_{Base})$ is more likely to hold. Panels (a) and (b) of Figure 4.6 show the temperatures recorded by the four thermometers on the sample, and the heat transfer calculated with Equation 4.19.

Unfortunately, the results of setpoint experiments were inconsistent and unreliable. It can be seen in panel (a) of Figure 4.6 that although one would expect the floating end of the sample (Thermometer 'A') to be warmer than the rest, that's not always the case. It

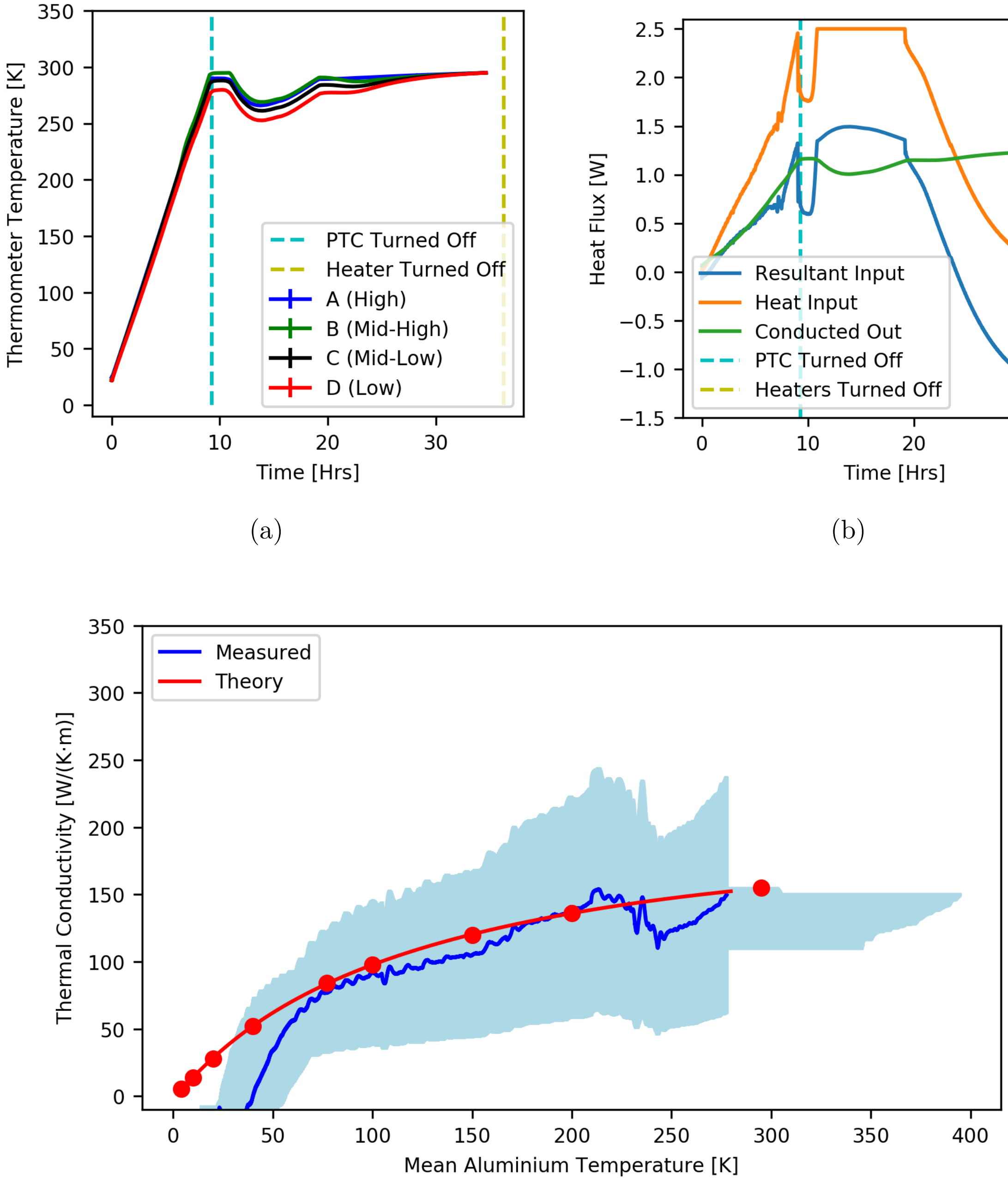

(a) (b)

(c)

Figure 4.5: The temperature (a) and heat (b) data used to calculate thermal conductivity (c) of aluminium. In this trial the sample was heated continually. Note that the agreement with theory is characteristically similar up until below 75 K where the thermal conductivity of copper becomes much stronger. The uncertainty is represented by the shaded area and is very large. The heater power steadily increases until the setpoint temperature is reached at which point the power is reduced. Once the sample cools, the heaters come back on. Note that a maximum of 2.5 W was allowed.

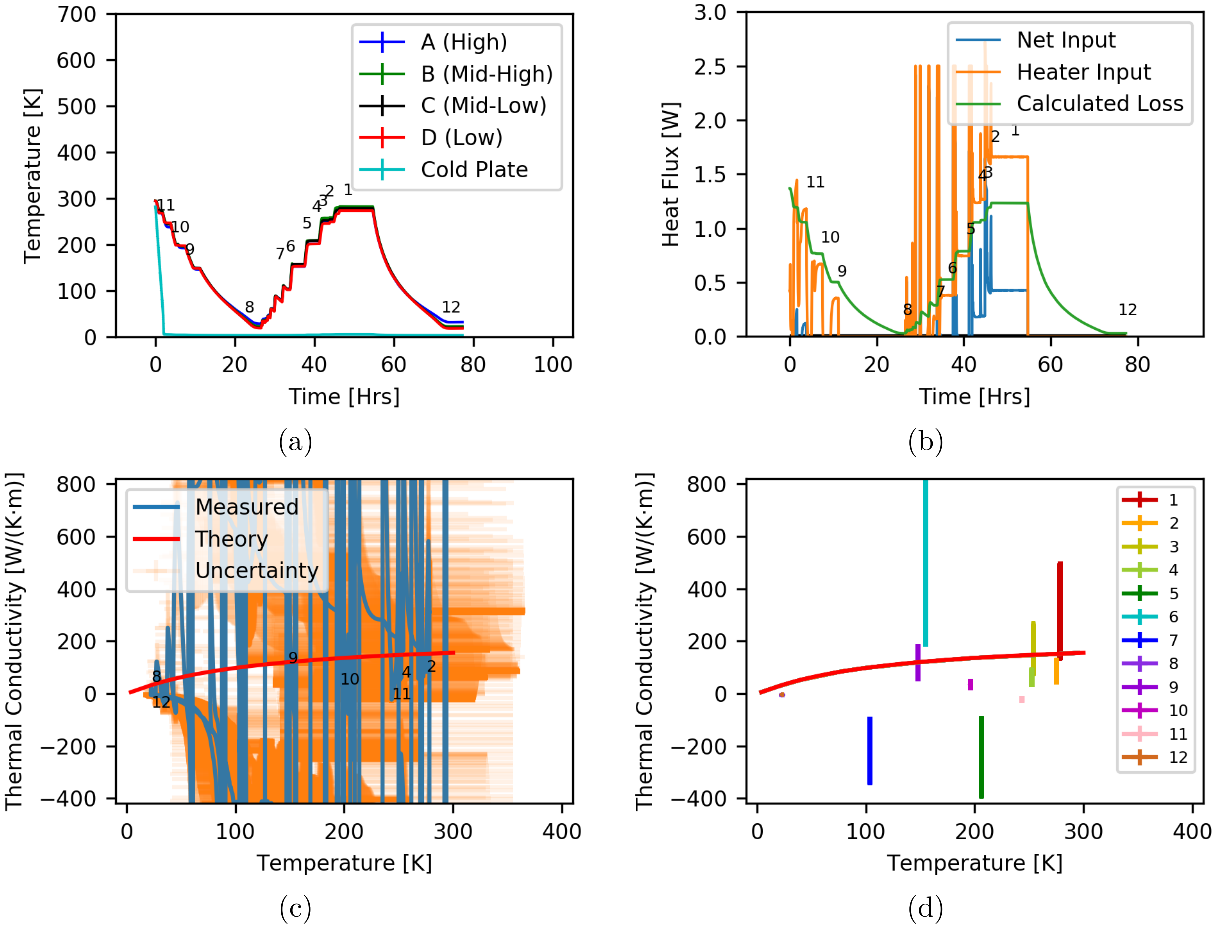

(a) (b)

(c) (d)

Figure 4.6: The thermal conductivity data taken using the setpoint method with both heaters active. Numbers 1-12 used to indicate sections which appear to be stable. Panel (a) shows the temperature data recorded, and panel (b) contains the corresponding heater data. Panel (c) shows the thermal conductivity when calculated continuously, demonstrating the unpredictable nature of the measure with uncertainty shown in orange. Panel (d) has selected for the periods of apparent stability. Even in the periods of apparent stability the thermal conductivity measurements are highly uncertain.

would also be expected that the temperatures would get progressively colder in the order A-B-C-D, as they are closer to the cold plate and this is seen during the cool-down. The order of warmest thermometer to coldest changed a great deal in the thermal cycle though, indicating that the path through which the heat is traveling may be changing.

The data on thermal conductivity are extremely imprecise as a result of the inconsistency in ordering of the thermometers from hottest to coldest and are shown in Figure 4.6. The thermometers were found to be consistent to within ∼0.5% across most the temperature range, but below 25 K their relative uncertainties increase to approximately 2%. The calibration uncertainty is not enough to explain the significant gradients in temperature observed. Panel (d) of Figure 4.6 shows the same data as panel (c), filtered to correspond to periods of thermal equilibrium as shown in panels (a) and (b). Not only do these periods of equilibrium not correspond to measures of thermal conductivity which agree with theory, they are also not self-consistent. Particularly around 150 K and 200 K there is a wide spread of data from the warmup, and these data don't agree with the measurements taken during cool-down.

The inconsistency in these experiments persisted and the poorly chosen method for adhering thermometry has been identified as the most likely explanation of the inconsistency. The copper tape not only presents an alternate path for the flow of heat, but also results in an inconsistent mechanical pressure if applied incorrectly. The inconsistent mechanical pressure may result in thermometry which is not thermalized with the sample, and this is a critical error in measurement. During other thermal cycles thermometry was adhered with kapton tape used in place of copper tape, and a third test used wooden clothespins to apply consistent mechanical pressure. The deviation in thermometry is shown in Figure 4.7 and indicates that copper tape is better than kapton, but that mechanical pressure is the most consistent method for adhering thermometry.

Due to the difficulty in measuring thermal conductivity, paired with the arrival of the three-phase metrology system and approaching deadlines, a change of focus was made to thermal contraction measurements. Thermal contraction measurements may be calculated based on mean temperature of the sample of interest rather than a thermal gradient, making the precision of thermometry less significant. Additionally, thermal pathways aren't as important for thermal contraction measurements so long as the sample is approximately isothermal. Given the limited time available it was decided pursuing measurements of CTE was a more efficient use of time than thermal conductivity measurements, so measurements of thermal conductivity were suspended.

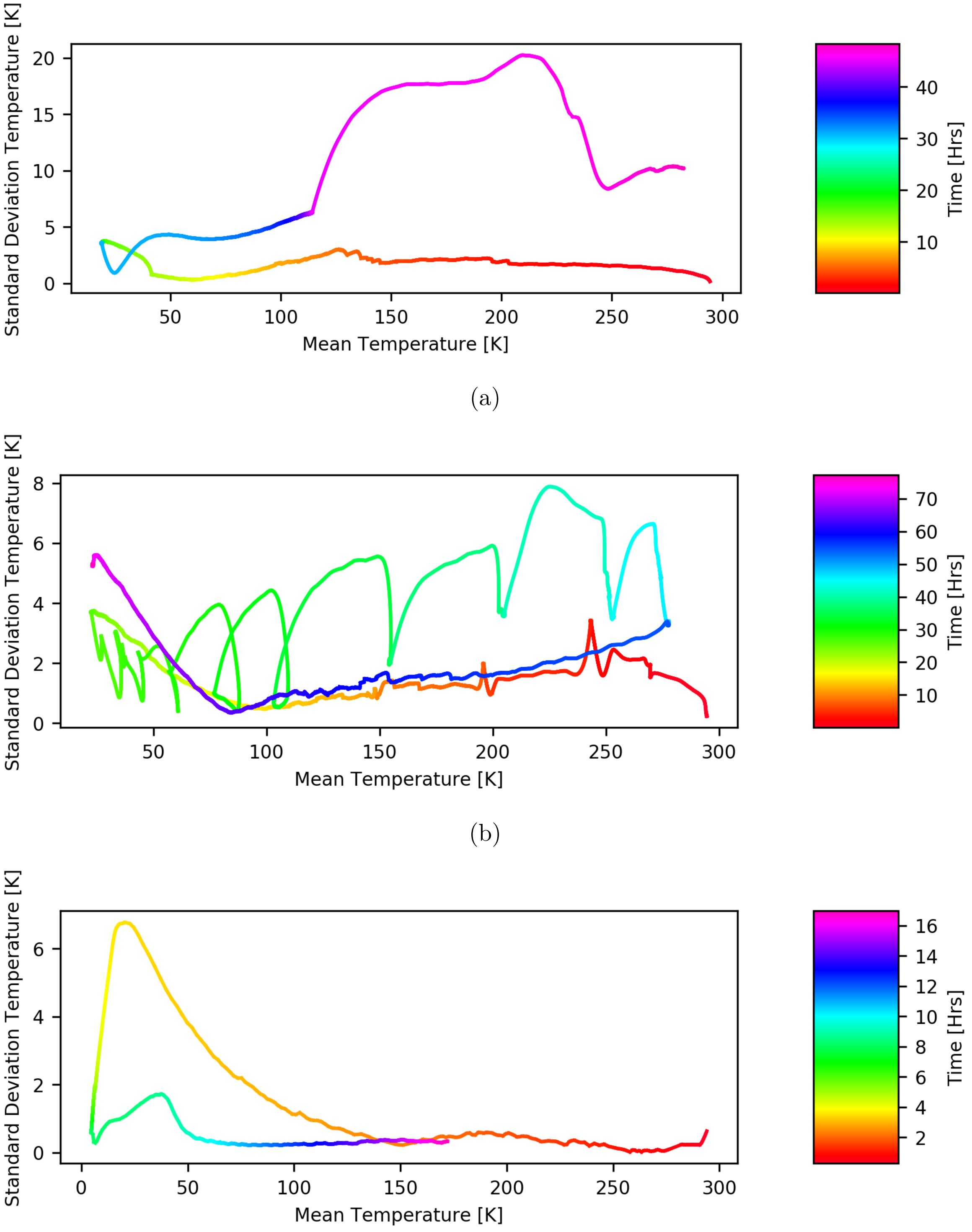

(a)

(b)

(c)

Figure 4.7: Consistency of thermometry using (a) copper tape, (b) kapton tape, and (c) wooden clothespins to apply mechanical pressure. Included is the time progression of the thermometry, as differences in temperature are expected during periods of warming and cooling.

## 4.4 Measuring Thermal Contraction

Measuring the CTE at cryogenic temperatures was first attempted using the Renishaw. A window was allowed from the 4 K chamber of the test facility cryostat (TFC) to the room, and a laser from the Renishaw was shone through the window and reflected back out off two mirrors at opposing ends of a tripod of CFRP. The setup can be seen in Figure 4.8. Measuring the contraction proved very difficult, however, as the Renishaw system is very sensitive to alignment and the differential contraction between clamps and the bolts resulted in slipping of the mount.

Another problem arising from this design was the radiative loading from the room through the cryostat window. The cold plate of the cryostat, which normally cools to 4 K, only reached 10 K. The samples measured were approximately 50 K during the first cool-down prompting use of a thermal braid from the floating end of the sample to the cold plate. Implementing the use of a copper braid brought the temperature of the sample down to 20 K, however due to the radiative loading this was the coldest the sample got. The thermometry data before and after a thermal braid was implemented are shown in Figure 4.9.

Not only did the thermal braid help to ensure the sample was able to cool more efficiently, but it also minimized the thermal gradient across the CFRP sample. The gradient across the CFRP sample is shown in Figure 4.10, and it is obvious that the thermal braid did a good job of keeping the three thermometers relatively thermalized, particularly at the coldest temperatures.

The data from Figure 4.10 show both that the thermal gradient was very large before the floating end of the apparatus was sunk to the 4 K plate, but also that radiative loading played a significant role in preventing the samples of CFRP from cooling below 10 K as evidenced by later trials in which CFRP did cool below 10 K, shown in Figure 4.20. Using these data with the length measurements taken by the Renishaw system it was possible to determine the relative change in length as a function of temperature.

The data for the two trials may be seen in Figure 4.11. The Renishaw lost alignment and

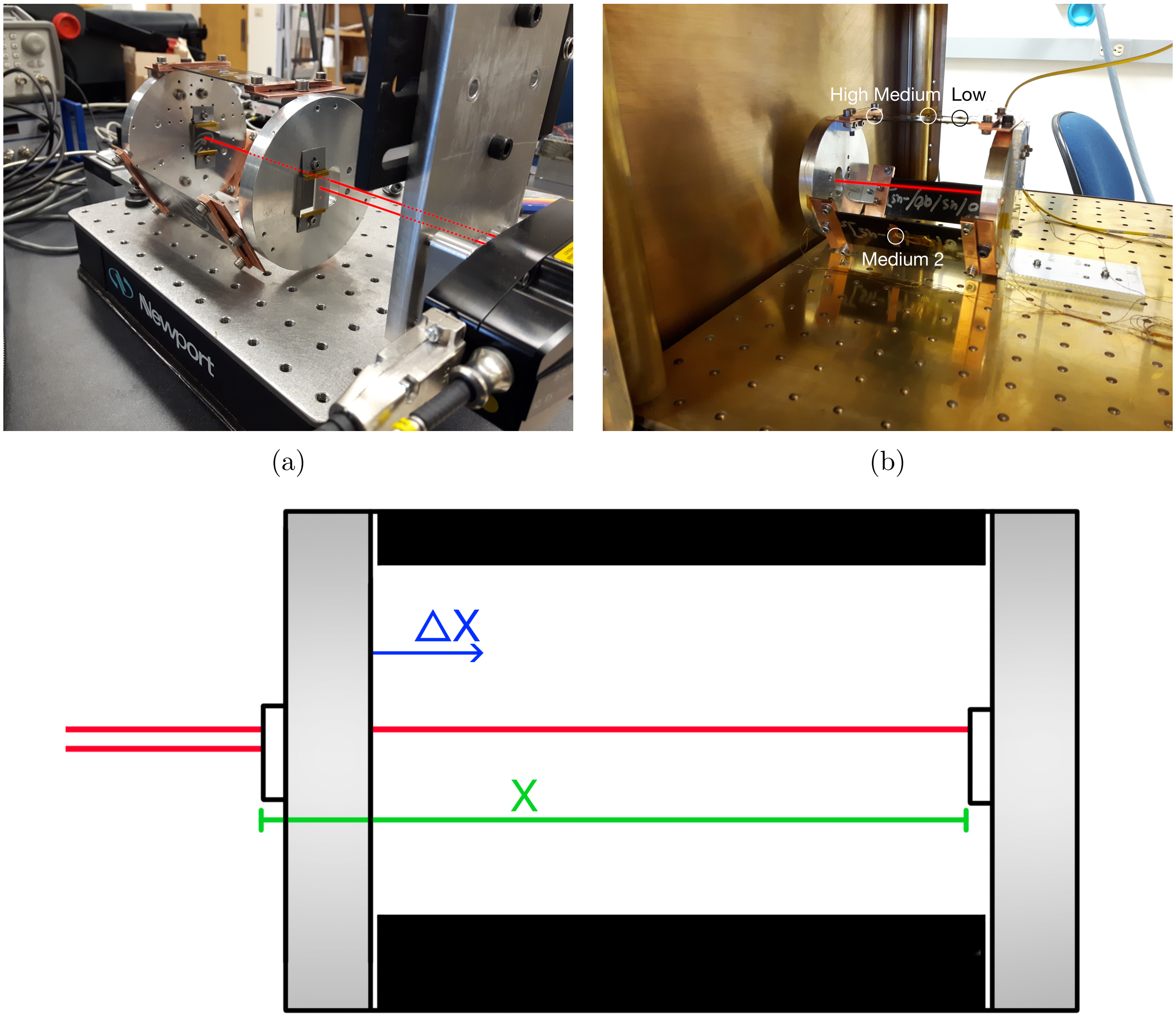

(a)

(b)

(c)

Figure 4.8: Experimental apparatus and diagram for measuring thermal contraction of CFRP in tripod arrangement. (a) View of the Renishaw beams reflecting off both mirrors on the tripod. The interference of these beams is determined by the changing length of the apparatus. (b) View of the 4 K chamber of the TFC with the tripod aligned with the external window. Note the three thermometers along the upper sample of CFRP, and the one thermometer on the sample of CFRP nearest to the camera. (c) Model of how thermal contraction measurements were made within the TFC. The two red beams reflect off opposing ends of the tripod. Contraction (Δx) will be measured by the differential laser system.

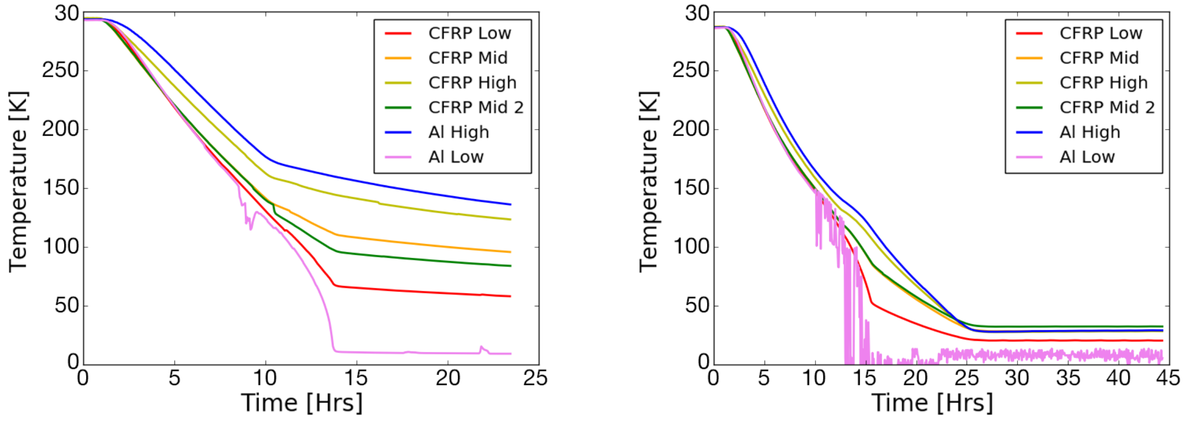

(a)

(b)

Figure 4.9: The temperature profile of each component in the tripod thermal contraction apparatus. (a) Shows the temperature before, and (b) after the implementation of a thermal braid from the floating end of the tripod to the 4 K plate. It can be seen that the 'Al Low' thermometer stopped working in the second trial.

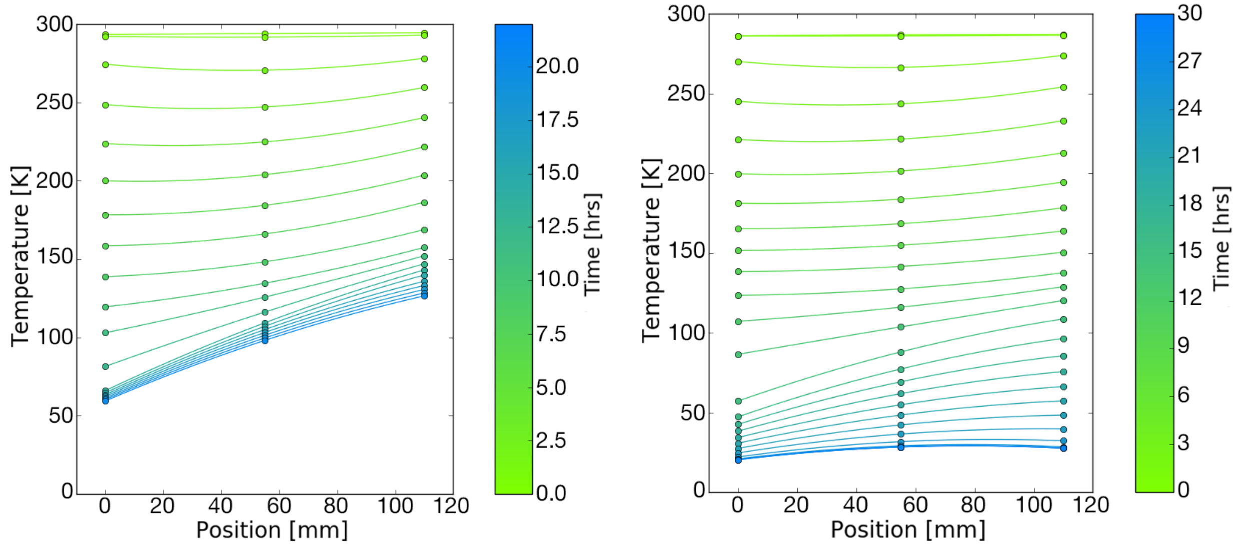

(a)

(b)

Figure 4.10: The temperature gradient during cool-down across the sample of CFRP before (a) and after (b) the implementation of a thermal braid.

lost track of the length many times resulting in discontinuous data. There is a systematic loss of alignment at approximately 200 K in both the ‘Cooldown’ trials, and in ‘Warmup 1’ which was attributed to slipping of the sample within the tripod with thermal cycling.

As the mis-alignment of the Renishaw proved a critical error it was necessary to redesign the mounting apparatus for the CFRP. Thermal loading through the window would also need to be addressed as it prevented the sample from reaching cryogenic temperatures. A new experimental design was needed with metrology internal to the cryostat which reduced the possibility of mis-alignment during thermal cycling, and a mounting apparatus more robust against a loss in alignment.

## 4.5 Designing a new Apparatus

The new experimental design involved a laser metrology system completely housed within the vacuum chamber of the cryostat which solved the problem of radiative loading and helped the sample cool to <5K. The new apparatus also needed to facilitate both thermal conductivity and thermal contraction measurements. The following experiments were performed within a different cryostat with a cylindrical geometry which also affected the design of the experiment.

In order to facilitate both measurements, an apparatus would need to satisfy a number of conditions. It would need to thermally isolate a sample material for measurements of thermal conductivity, and have clearance for fibre-optic cables to be mounted along the axis of contraction for thermal expansion measurements. Since the sample must already be thermally isolated it is sensible to utilize the existing mechanical clearance for routing the fibre-optic cables. The following section describes the apparatuses designed to facilitate both thermal conductivity and thermal contraction measurements at cryogenic temperatures.

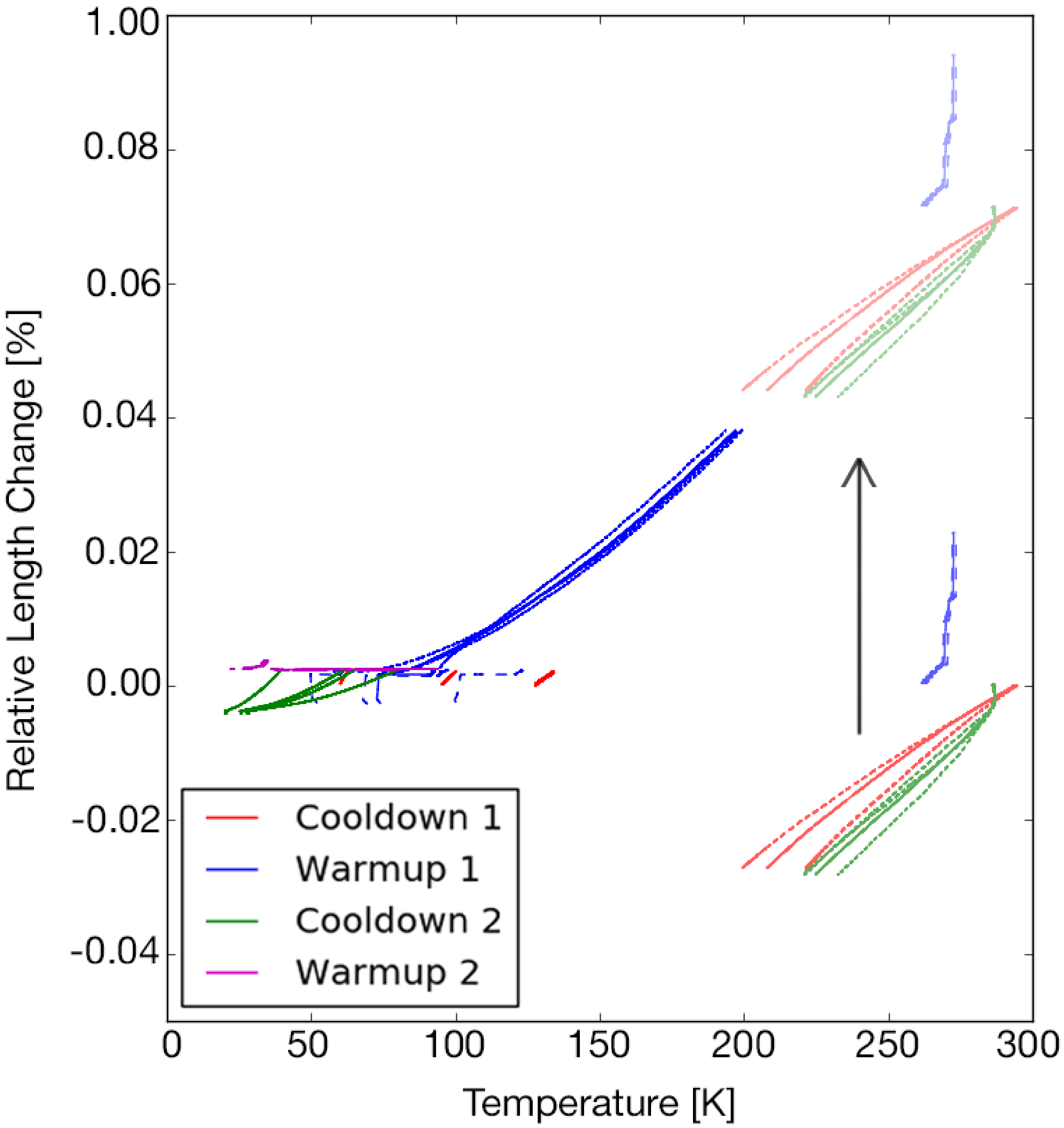

Figure 4.11: Thermal contraction of CFRP measured in the TFC. The consistency of the mis-alignment around 200 K is likely due to slipping in the apparatus due to differential contraction of components. Correcting the discontinuity by eye shows how the data may have come together. Contraction plotted as a function of mean temperature (solid lines), and also as a function of each individual thermometer (dashed lines).

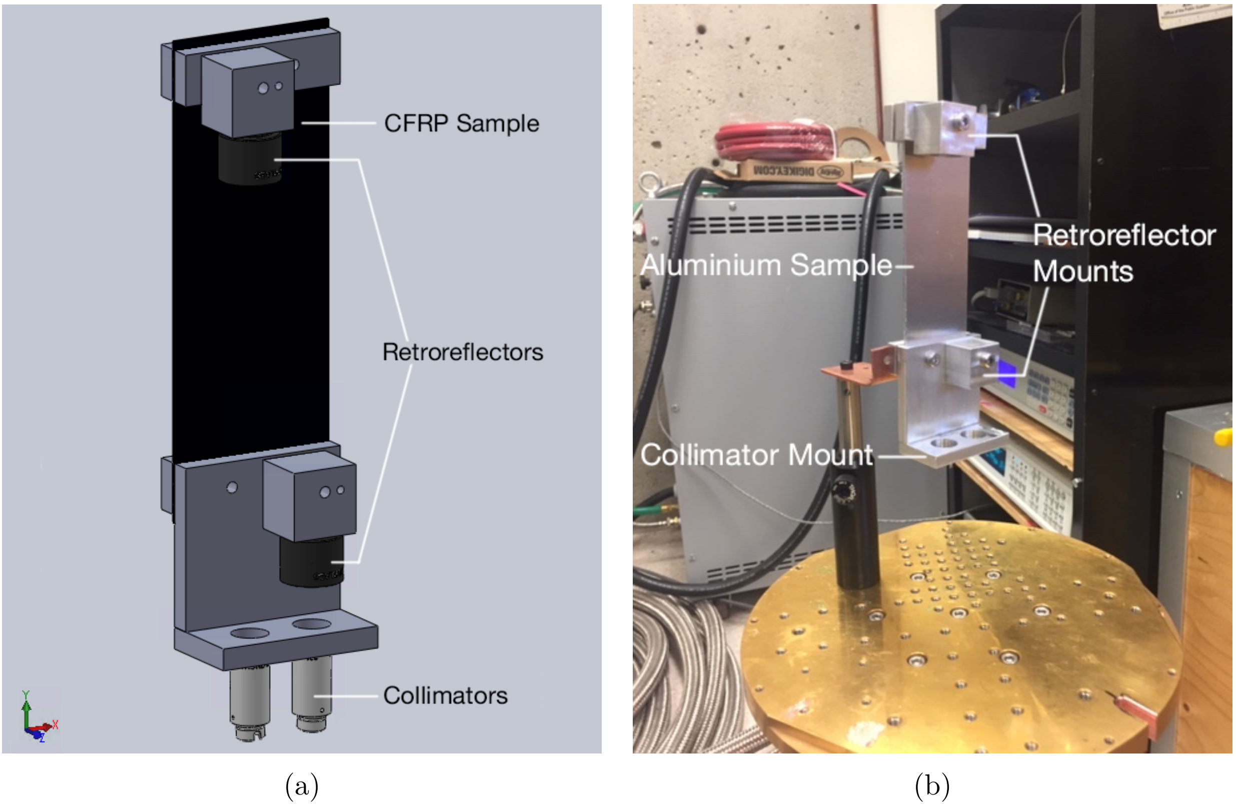

(a) (b)

Figure 4.12: CAD model of the first metrology mount design (a), and final product after manufacturing (b).

### 4.5.1 First Metrology Mount

Whilst awaiting finalization of a comprehensive design (dubbed a “cryogenic thermal isolation chamber” (CTIC) for its relatively simple geometry), a preliminary apparatus was designed for measuring thermal contraction alone. A few small pieces which bolt together effectively reproduce the properties necessary for thermal contraction measurements, so the pieces were machined and preliminary CTE testing took place in advance of completion of a more comprehensive apparatus. The temporary mount holds the sample vertically within the cryostat, mounted with retro-reflectors and attached to a collimator mount, as seen in Figure 4.12. The collimators are aligned with the retro-reflectors by design for ease of alignment.

The two major obstacles in the previous experiment were a loss of alignment due to plane-parallel mirrors and distortion of the mount during cooling, and the radiative loading which prevented the sample cooling to cryogenic temperatures. The loss of alignment in cooling may have been corrected by using retro-reflectors rather than plane-parallel mirrors, but the issue of radiative loading was critically limiting the experiment. The solution to radiative loading was to get rid of the need for a window with a laser-interferometry system mounted within the cryostat. This also enabled a reduction in the optical path length and reducing environmental variability for the metrology system as the laser was no longer traveling through air or the cryostat window.

Housing the laser, photonics, and fibre-optics within the cryostat required some modification to the cryostat components. The laser's operational temperature is constrained so it must be mounted in the room temperature component of the cryostat. The photonics must be mounted closely to the laser in the room temperature volume and this imposes strict restrictions on dimensions for a mounting plate. A few iterations of the plate were considered before it was decided that the best method was to mount the spool of fibre-optic cable on the reverse side of the plate. The final design of the plate for co-mounting the laser, photonics box, and fibre-spool is shown in panel (a) of Figure 4.13 below, and the final product is shown in panel (b). The unarmoured portions of the fibre-optic cable were taped to the mounting plate and allowed to have some slack to avoid any unnecessary strain. Mounting the spool on the reverse side liberated just enough space for the plate to house all three components within the room temperature volume, as shown in panel (c) of Figure 4.13.

With the laser mounted inside the room temperature volume, and the measurements taking place within the 4 K volume it was necessary to create a physical path for the fibre-optic cable which didn't jeopardize the thermal isolation of the 4 K volume. The armoring on the fibre-optic cable is made of stainless steel and is therefore a strong thermal insulator (See Figure 4.4). The 44 K and 4 K plates act as physical barriers between the different sections of the cryostat and in order to route the fibre from one end to the other the plates had to be altered. One suggestion was to simply bore holes large enough to pass the fibre-optic cable through them, however these holes would need to be large enough to pass the

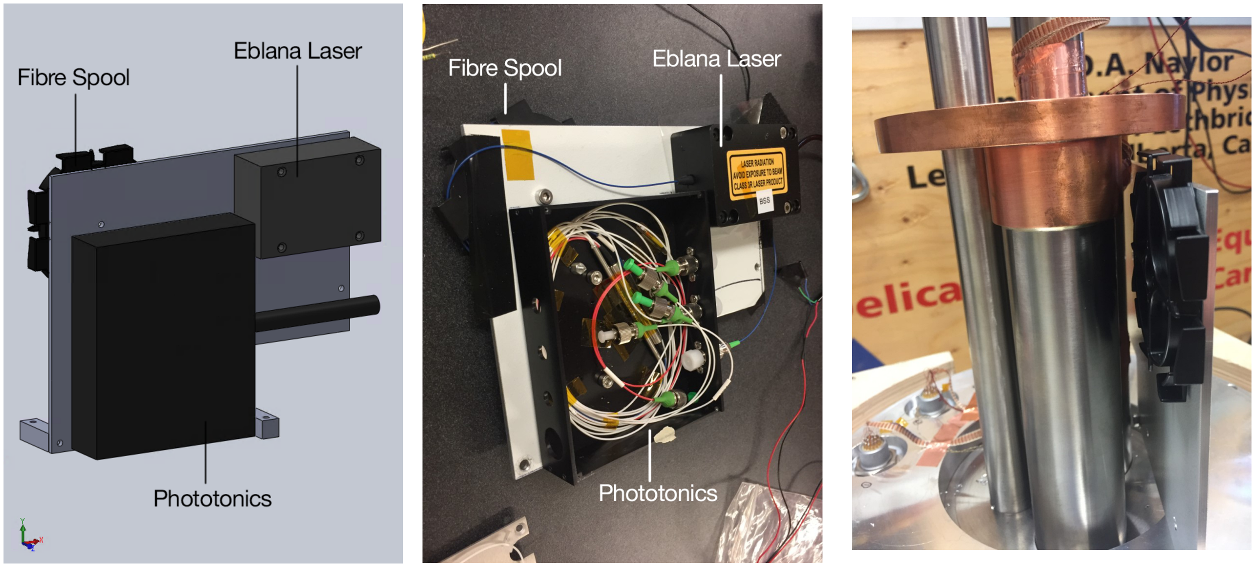

(a) (b) (c)

Figure 4.13: The design and final product of the room temperature mounting plate. (a) Finalized design of the plate for mounting laser, photonics, and fibre-optic spool within the room temperature volume of the cryostat. (b) Actual plate used for mounting laser, photonics, and fibre-optic spool. (c) Clearance between the tubes of the cryostat and the fibre-spool showing the tight volumetric constraints.

terminal connectors which are wider than the cable itself. Because of this complication, it was decided that the best option was to cut slots in the side of the plate through which the fibre could be routed, and then closed when the shield is placed over top. The CAD model of this modification is shown in panel (a) of Figure 4.14. A picture of the completed setup with the armoured cable, metrology mount, and room temperature mounting plate is shown in panel (b) of Figure 4.14. On top of the 4 K plate the retro-reflectors and collimators can be seen in the metrology mount.

The relative contraction of an aluminium sample measured using the three-phase metrology system (described in Chapter 3) internal to the cryostat agreed well with the accepted values and the results are shown in Figure 4.15. While promising, these results were not repeatable and therefore did not warrant continuing with CFRP samples. In the trial shown in Figure 4.15 the absolute difference in length between experiment and theory was at most $\sim 20\,\mu$m so it was believed to have been the result of components shifting, particularly the

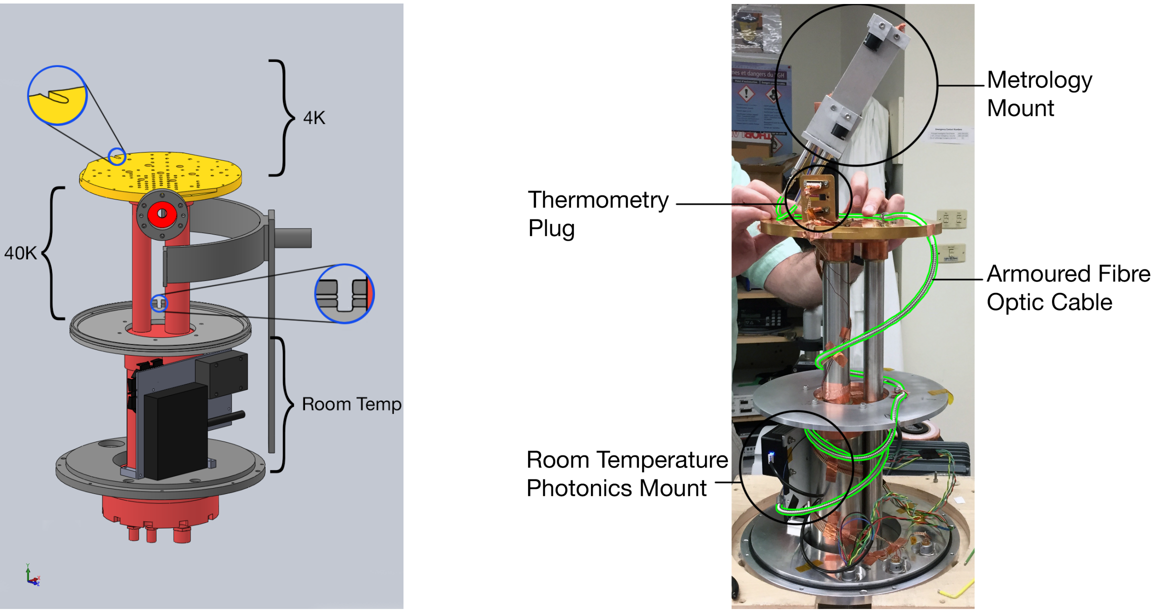

(a)

(b)

Figure 4.14: Proposed modifications to the cryostat and final result. (a) The two finalized locations for the slots are highlighted here. The sections of the cryostat are labeled for clarity. (b) The exposed cryostat with 4 K plate at top, 40 K plate below, and room temperature volume at the bottom. Wiring in room temperature component connects via plugs to a computer external to the cryostat. The armoured fibre-optic cable can be seen highlighted in green winding from the room temperature volume up to where it is clamped to the 4 K plate, and mounted into the metrology mount for recording change in length.

retro-reflectors contracting less than the aluminium mounts into which they were screwed and slipping in the threads. It was later discovered that the two collimating optics were mis-aligned and this may have contributed a cosine effect in one of the beam paths.

Although these components facilitated preliminary measurements of thermal expansion and could be minimally modified for thermal conductivity experiments, additional problems necessitated the use of a more sophisticated apparatus.

### 4.5.2 Monolithic Metrology Mount

In attempting to setup the laser metrology for length contraction measurements it was discovered that alignment of the optics was a significant challenge. As the laser metrology system operates in infrared wavelengths it is not visible so alignment was done by maximizing the power output at a detector. However, when the collimators were inserted into their mount

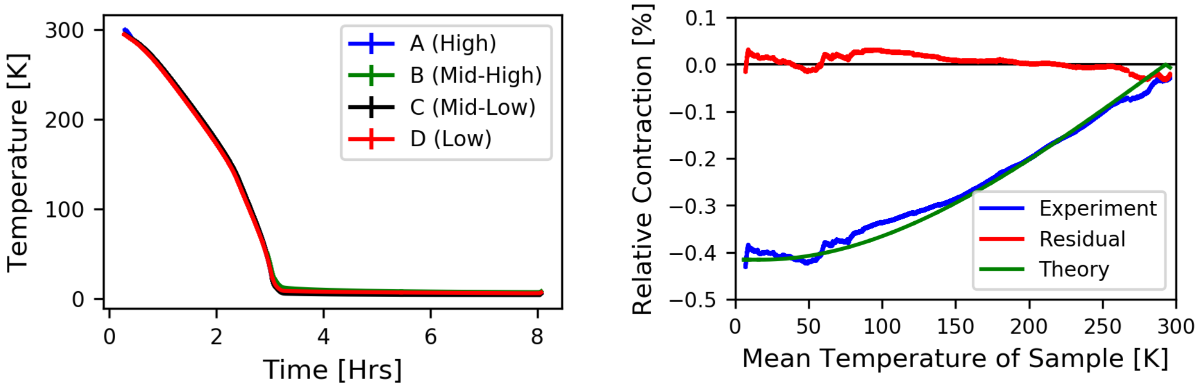

(a)

(b)

Figure 4.15: The temperatures (a) and relative contraction (b) of a sample of aluminium cooled to cryogenic temperatures. While the experimental data agree with theory for the most part, there is still a non-negligible mis-match and this may correspond to mis-alignment of the optics or slipping as components of the mounting apparatus contract differentially.

and the beam traced out with an infrared viewing card, it was discovered that there was an angular displacement between the two beams of ∼3.6°. This angular displacement was sharp enough to be visible to the naked eye, at maximum detected power the collimator appeared to be off-axis as shown in Figure 4.16 below.

The mount had been machined such that the two beams should be parallel, but also had many small pieces which bolt together. In the hopes to eliminate this angular displacement a secondary mount was machined out of a single piece of aluminium. In this way the holes for the collimator and the retro-reflector could be machined in parallel and guarantee axial alignment in the mount. Although it was later discovered that the mis-alignment was the result of using collimators which were mis-matched to the fibre-optic connectors, the secondary mount was still chosen for its robustness against differential contractions.

At the same time as this new mount was being designed our lab received posts constructed from a metal alloy with negative CTE in the axial direction. The mount was designed to be able to handle both the measurements of our CFRP samples and the new negative CTE posts. The CAD model of the mount design is shown in panel (a) of Figure 4.17 with the negative CTE posts shown in cyan to differentiate from the rest of the mount since the

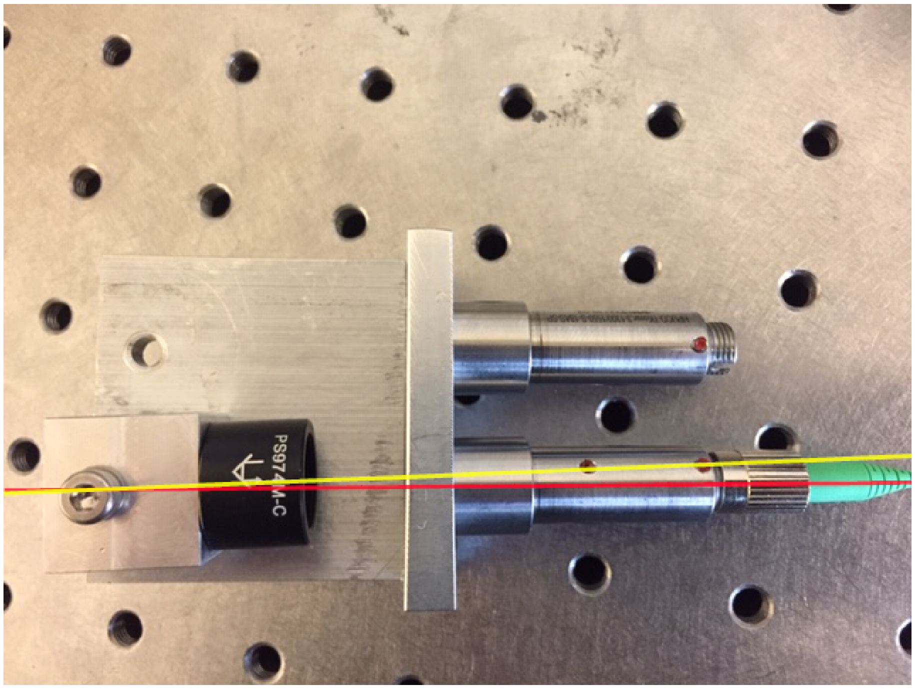

Figure 4.16: Image showing the direction of the retro-reflector for maximum signal. There is a slight angular displacement (∼3°) between the axis of the collimator, shown in red, and the axis of the retro-reflector shown in yellow.

true colour of the posts is quite comparable to that of aluminium. The final product for the “U-bar” mount is shown in panel (b) Figure 4.17 without the presence of the negative CTE post, which attaches via an axial bolt which penetrates the retro-reflector mount in the center.

The monolithic metrology mount was used in conjunction with a new frequency-modulated laser metrology system, described in Section 3.4. This new metrology system was used to measure the length contraction for the same aluminium sample that was measured by the three-phase metrology system, the results of which are shown in Figure 4.15. Only one beam path is needed for the frequency modulated system, so the measurements are no longer completely differential. The loss of differential lengths means that care must be taken to calibrate out contraction from other components, such as the collimators and fibre.

Measuring the temperature of every component whose differential contraction will contribute to measured changes is unfeasible, particularly since components such as the fibre

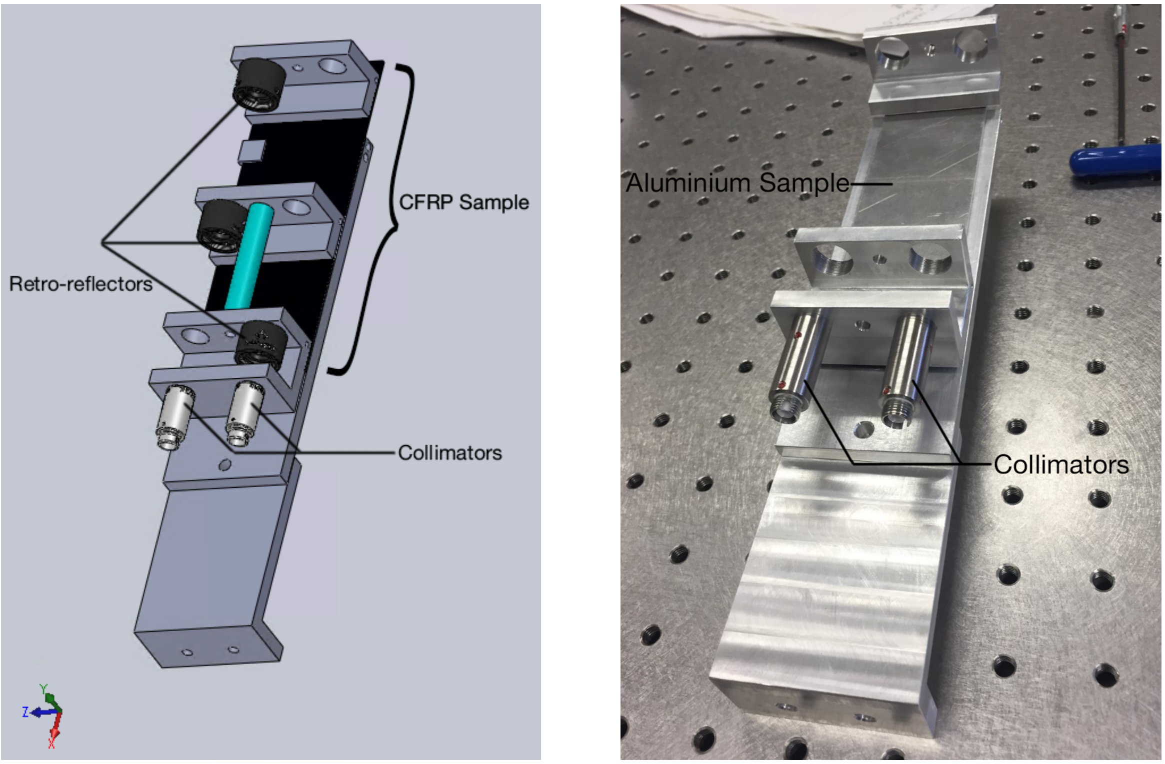

(a) (b)

Figure 4.17: The design and final product of the “U-bar” mount. (a) CAD model of the second mount design. The U-bar holds both the collimators and one retro-reflector. The second retro-reflector is held by a mount which can attach to either the sample of CFRP, or the post of negative CTE material enabling use for both measurements. (b) Machined components of the “U-bar” mount with aluminium sample in place.

tip contribute to the differential contraction but are isolated from thermometry. To isolate contraction in the sample alone measurements were taken of the aluminium sample, with two different lengths. The two trials had effective lengths of 105.125(40) mm and 78.125(40) mm respectively, as measured with calipers. The reason for choosing two lengths of the same sample is that both datasets will include contraction from the other components of the apparatus. The difference between them should only be due to the contraction of the 27.000(50) mm difference in aluminium length. The experimental setup is shown in Figure 4.18, the apparatus is in place inside the test facility cryostat again, so it has been laid horizontally which helps to prevent resonance vibrations in the sample. A suggestion from Brad Gom of the astronomical instrumentation group was to use a roller, which can be seen underneath the floating end of the sample. The roller allows the sample to contract and expand with minimal frictional forces. The roller also helps to prevent resonant vibrations in the sample and helps to cool the sample faster.

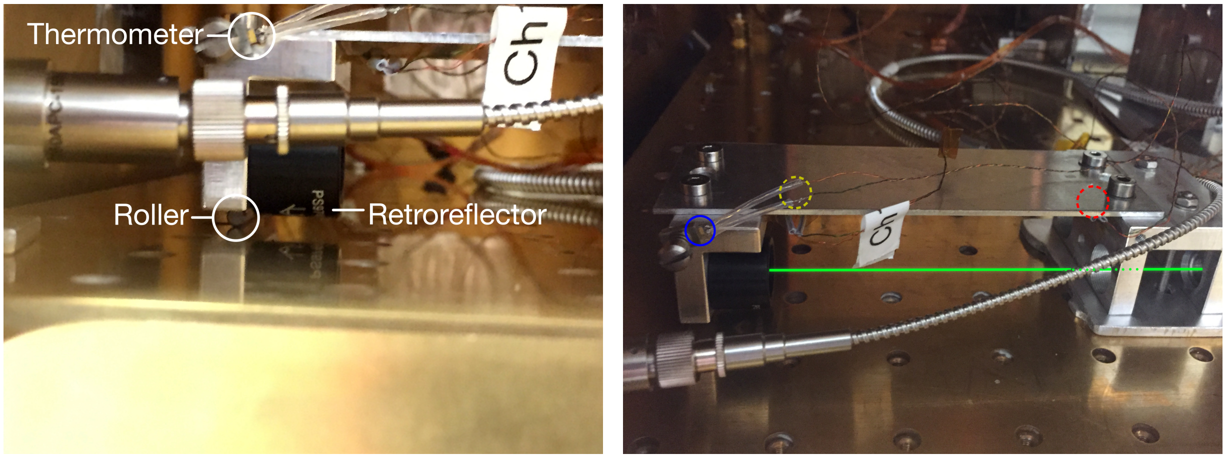

(a) (b)

Figure 4.18: Experimental setup for measuring the CTE of aluminium using the frequency modulated metrology system. (a) Roller under the floating end of the sample. (b) Beam path and thermometry on the apparatus. Dashed yellow and red lines indicate thermometry on the reverse side of the sample, used to determine the mean temperature.

In order to account for systematic effects the data have been separated into warmup and cool-down segments. The difference in recorded length between the two data sets is shown for both the warmup and cool-down data and compared against the theoretical contraction of 27 mm of aluminium in Figure 4.19.

The results, though not perfect, are promising and show a residual of less than 10 $\mu$m across the entire temperature range. It is possible that some of this difference is due to deviations from theory, as the tabulated values in Figure 4.2 show. This result is a significant improvement over previous results, and is reliable enough to justify the same measurement with CFRP samples. Using these results it was possible to determine the contraction from the mount itself. The raw data show that the absolute contraction is greater than that predicted by theory, and the excess is due to contraction in the mount. The average of two aluminium trials, with a warmup and a cool-down each, gave four unique curves for the contraction in the mount. These four trials can be seen in Figure 4.20, and their average

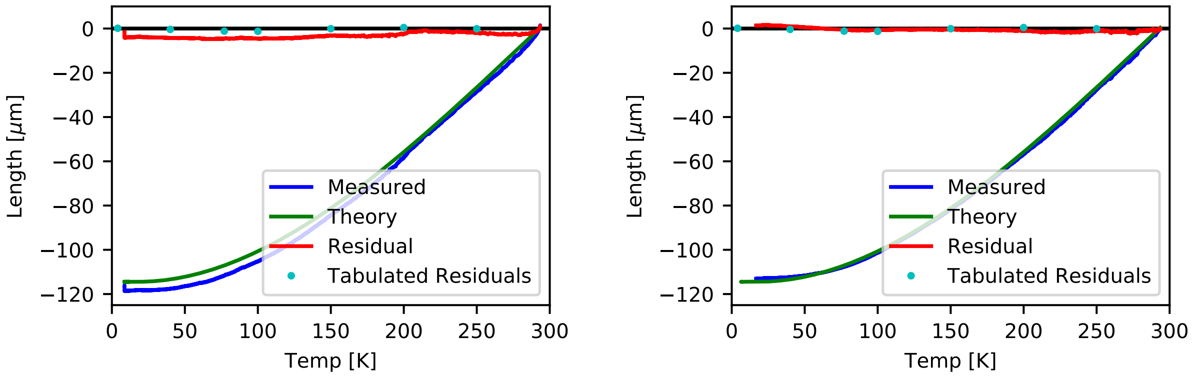

(a)

(b)

Figure 4.19: Comparison between measured contraction of 27 mm of aluminium and theory for the cool-down (a) and warmup (b) of the sample. Shows fairly reliable agreement, particularly in the warmup data.

can be subtracted from measurements to find the contraction in the sample itself.

A test run with a sample of CFRP with fibres running perpendicular to the axis of contraction (perpendicular CFRP) resulted in measurements of length contraction up to 20 mm on the cool-down and 1.75 mm on the warmup. Both of these values are far greater than the anticipated contraction and are believed to be the result of micro-fracturing in the sample which causes length changes in excess of that prescribed by the sampling rate of the system. Since a phase change of magnitude $>\pi$ in either direction results in degeneracy, the system can only afford a change in optical path length of $\lambda/2$ in a sampling period $\Delta$t. The change in optical path length is twice that of physical path length and therefore the system can only track changes at speeds up to

$$v = \frac{\lambda/4}{\Delta t} \quad [\tfrac{\mu m}{s}]. \tag{4.23}$$

Currently the metrology data requires intensive post-processing to calculate the position based on the detector signal. This has led to an extension of the sampling period by a factor of 200 and a corresponding reduction in the tolerable speed of contraction. The system is currently being updated with a field programmable gate array (FPGA) which will be able

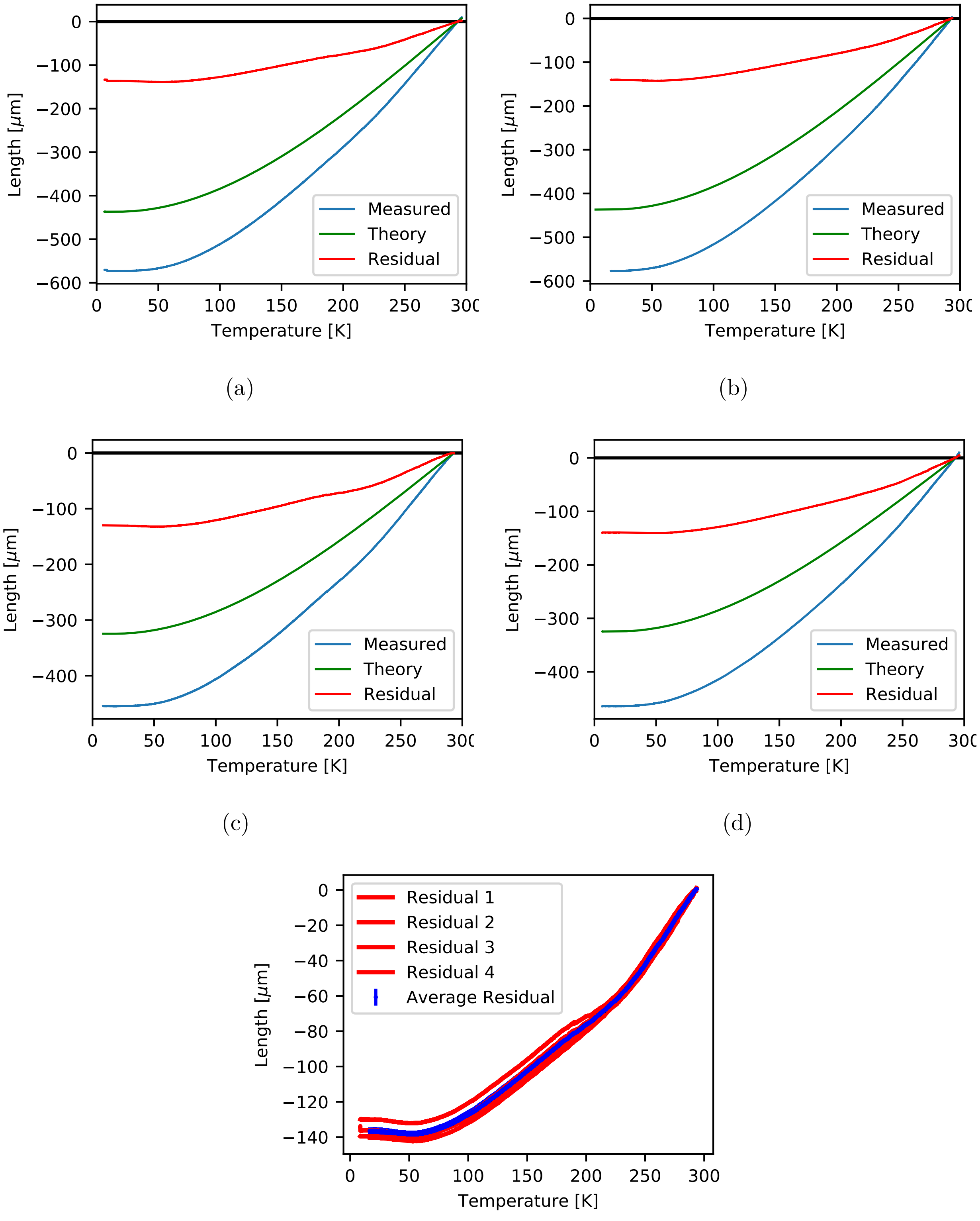

(a)

(b)

(c)

(d)

(e)

Figure 4.20: Aluminium trials used to determine the contraction in the mount. (a) First set of cool-down data. (b) First set of warmup data. (c) Second set of cool-down data. (d) Second set of warmup data. (e) The determination of contraction in the mount using the residuals from panels (a) through (d).

to process the raw signal into position data at 1 KHz ($\Delta t = 1\,\mathrm{ms}$) and enable the system to be far more robust against issues like micro-fracturing.

A measurement of the contraction in a sample of CFRP which had fibres running parallel to the axis (parallel CFRP) of contraction did not suffer from the drift seen in the results of the perpendicular sample. The data from this trial can be seen in Figure 4.21.

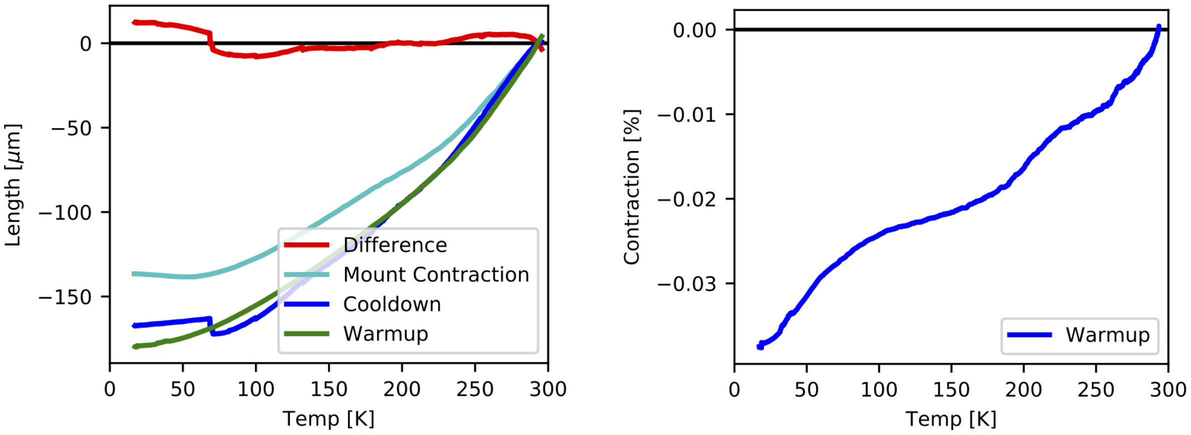

(a)

(b)

Figure 4.21: Determination of the relative contraction in a sample of CFRP with fibres laid parallel to the axis of contraction. (a) The absolute contraction measured by the frequency modulated system in the cool-down and warmup of a sample of CFRP. Also included is the average contraction in the mount. (b) The length change after accounting for the contraction in the mount.

Unfortunately, the cool-down data displayed drifting and skipping in the data. If these issues are the result of micro-fracturing in the fibres it makes sense that the effects are manifesting in the cool-down data more substantially than the warmup data as was also the case with the perpendicular CFRP. The warmup data for parallel CFRP show no obvious signs of drift and are shown in Figure 4.21.

Successful measurements of the CTE of aluminium and CFRP may be performed with the monolithic metrology mount, but it is still not as robust an apparatus as ultimately desired. In order to conduct thermal conductivity measurements as well, a better experimental setup is needed.

### 4.5.3 Cryogenic Thermal Isolation Chamber Design

The ultimate end of the experimental design was always to have a semi-permanent setup in which measurements of both thermal conductivity, and thermal contraction could be made. We opted to use the model of Tuttle et al. [93] shown in Figure 4.22, which was designed for measurements of thermal conductivity. The design of Tuttle et al. [93] works well for measurements of thermal conductivity because of the ability to thermally isolate the sample of interest, and with very little work the design can be manipulated to facilitate measurements of thermal contraction as well.

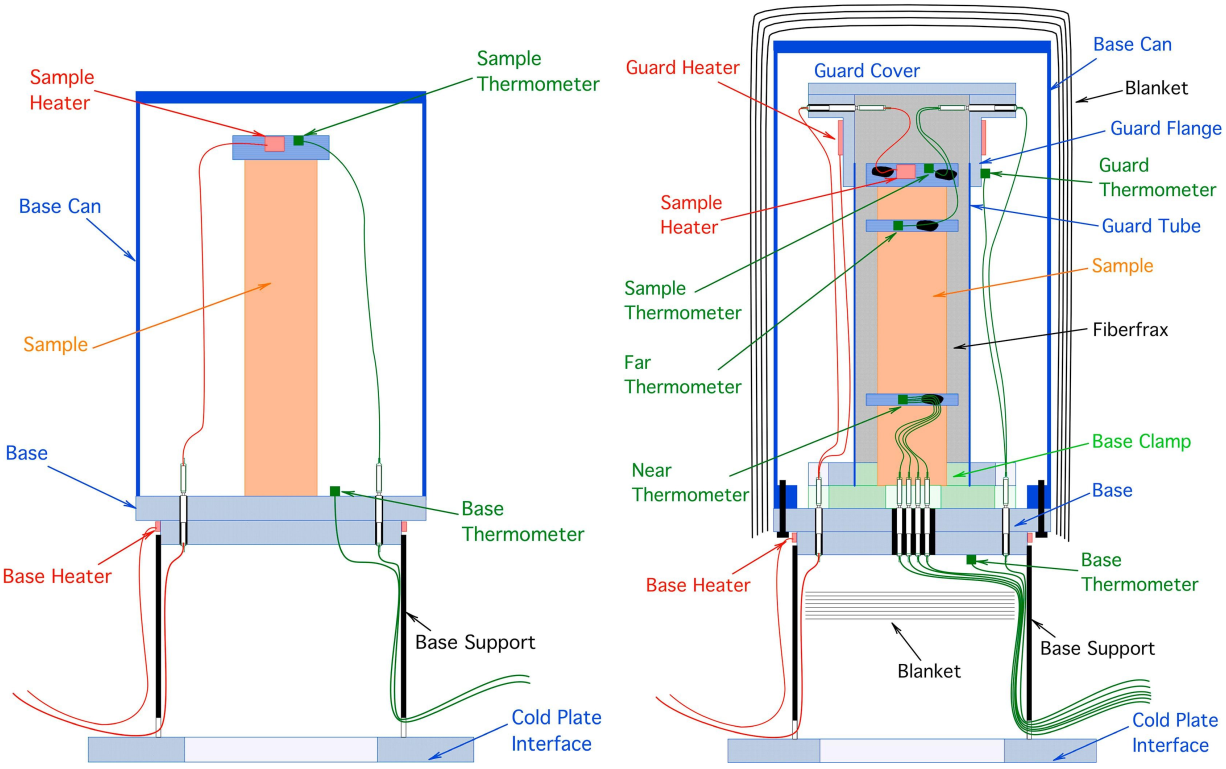

(a) (b)

Figure 4.22: The design of a basic (a) and a more advanced (b) experiment for measurements of thermal conductivity. Source: Tuttle et al. [93].

Though the more involved design of Tuttle et al. [93] is more appropriate for high-precision measurements, the added complexity meant that this sort of design would take far longer to implement. The blanket which surrounds the box would need to be damaged in order to pass fibre-optic cable through the base and the intricacy of the apparatus would make it challenging to swap out samples. Because of the need to measure thermal contraction the simpler design in panel (a) of Figure 4.22 was used as the starting point and modified to suit the specific needs of the experiment.

In designing a comparable box for local experiments it was important to be aware of volumetric constraints. Though a cylindrical chamber would be more space-effective in the cryostat the difficulty of machining cylinders meant a more-easily constructed rectangular design was chosen. Any design utilized for precision measurements would need to satisfy a number of conditions before it could be approved. The CTIC must:

1. Fit within the existing 4 K chamber which is 200.20(25) mm diameter by 292.0(5) mm tall.
2. Be large enough that the sample material, thermometry, and optics may all be contained within (samples are ∼110 mm long current metrology mount has a 60 by 50 mm footprint).
3. Isolate the sample from the cold plate to enable measurements of thermal conductivity for $4\,\mathrm{K} \lesssim \mathrm{T} \lesssim 300\,\mathrm{K}$.
4. Have clearance for the fibre-optics used to measure thermal contraction.
5. Facilitate quick turnaround on thermal cycles by minimizing the mass and thermal loading in the 4 K chamber.

Assuring that the CTIC is capable of all these thing is not a trivial task. Points 1 & 2 are interdependent as increasing the size of the CTIC reduces clearance in the 4 K chamber. Likewise points 3 & 4 work together as the clearance for the fibre-optics can be created by mechanically isolating the box from the cold plate. Point 5 effectively amounts to using as little material in the construction of components as possible, which poses a challenge to mechanical stability.

To ensure that points 1 & 2 were satisfied the CTIC was designed to have a square cross-section which shares a common area centroid with the circular face of the 4 K plate. In order to minimize thermal mass (point 5), whilst maximizing working volume, the CTIC was designed to be made of aluminium with two quarter-inch (6.25 mm) thick faces, and two sixteenth-inch (1.5625 mm) faces for the sides. A quarter-inch thick base for mounting the thicker faces, and a sixteenth-inch thick lid give the box the necessary mechanical stability whilst minimizing thermal mass. The thicker faces of the box act as mechanical support for the two thinner faces and the lid of the box. The two thinner faces bolt into the two thicker faces of the box as well as into the base. The lid also bolts into the two thicker faces. The thinner faces and the lid are in place only to seal the box from light and will not be responsible for any significant structural support. Figure 4.23 shows the base of the CTIC once it has been assembled and with all the pieces in place the external cross-section is square with side lengths of 5 in (127 mm).

For points 3 & 4 careful consideration of the thermal transfer from the box to the cold plate is needed. The tolerance limit for the bend radius in the fibre-optics was set to be 9 cm to ensure no significant stress was put on the fibre and to avoid losses in the signal. By threading the collimators directly into the base of the CTIC a small amount of space could be salvaged, but roughly 9 cm clearance is needed between the base of the CTIC and the 4 K plate. This mechanical isolation can be translated into thermal isolation, and it is important to strike the correct balance of heat transfer such that the sample is sufficiently isolated during measurements, but also that the CTIC is still able to cool in a reasonable amount of time.

### 4.5.4 Standoff Struts

To thermally isolate the CTIC from the cold plate, hollow stainless steel tubes with small cross-sectional areas were chosen. These ‘struts’ need special consideration as they will be subjected to large thermal gradients, support the weight of the entire CTIC apparatus and

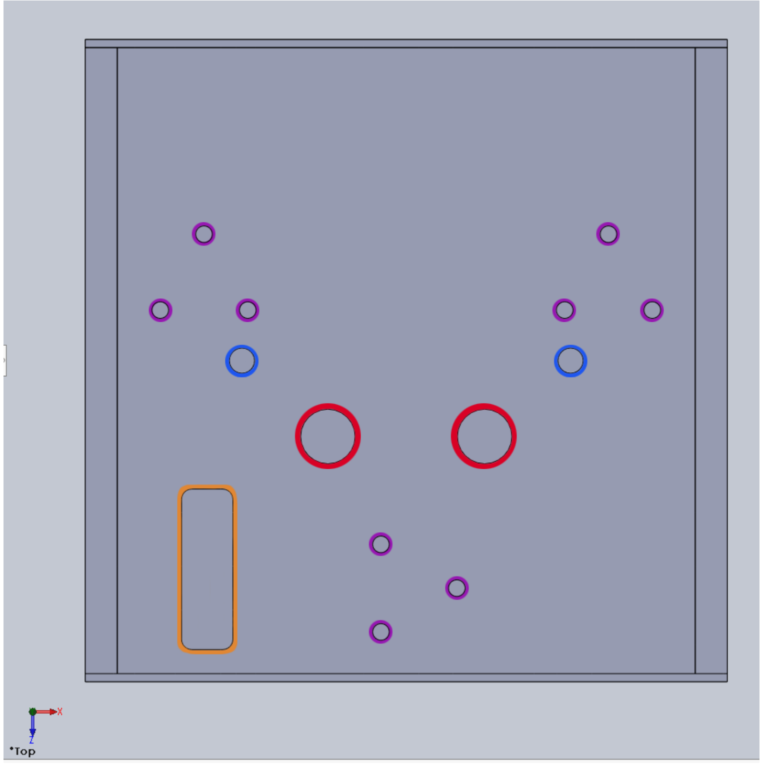

Figure 4.23: Base plate of the proposed CTIC, with holes for the three struts (purple), as well as the fibre-optic collimators (red). The rectangular slot at bottom left (orange) is in place to wire in thermometry and heaters. The two holes along the central x-axis of the base (blue) are for mounting the sample inside the CTIC.

internal components, and need to be immune to effects of differential contraction. The struts also need to mate the rectangular face of the CTIC to the cylindrical face of the 4 K plate, and be sufficiently balanced about the center of mass of the box to minimize internal moments, stresses, and strains.

Because the struts need to thermally isolate the CTIC from the cold plate, they were modeled using stainless steel which is a readily available material and a thermal insulator. The heat transfer from the CTIC to the 4 K plate will be primarily in the form of conduction through the standoff struts, and as Equation 4.14 shows, the cross-sectional area and length of the struts may be adjusted to tune the amount of heat transferred. While the length of the struts is somewhat restrained, the cross-sectional area may be altered through more than an order of magnitude, depending on diameter and wall thickness of the tube [94].

Attaching the struts to the base of the CTIC as well as the 4 K plate also requires careful attention. Unique feet for the struts were designed to bolt into the 4 K plate and have bolts through the wall of the strut as seen in panels (a) and (b) of Figure 4.24 respectively.

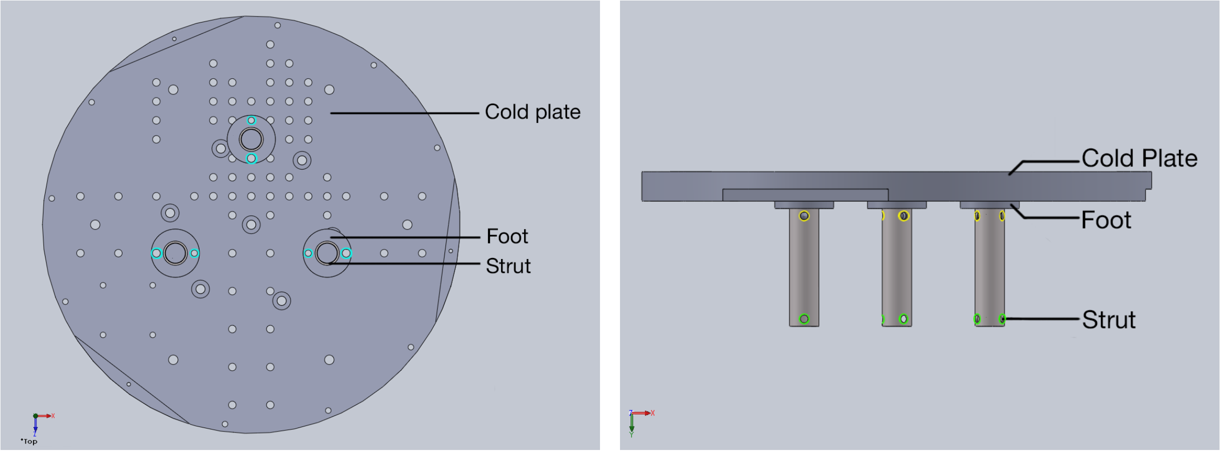

(a) (b)

Figure 4.24: CAD models of the standoff struts, and the feet which affix them to the cold plate. One of the holes in each foot, and two of the three holes on each end of the strut are over-sized to allow for thermal contraction. (a) Top-down view of the cold plate with three struts, each with two bolt holes for fixing to the plate (cyan). Holes in one strut are along an orthogonal axis for rotational stability. (b) Profile of cold plate with three struts, each with two bolt holes for fixing to the plate. Holes in the walls of the strut allow for bolting through to the feet. The yellow holes are used to attach to the feet shown in panel (a) of Figure 4.25 and the green holes attach to those shown in panel (b) of the same figure.

Using a different model of foot with three holes the struts are then attached to the base of the CTIC via the sets of three holes offset from one another by 120° seen in Figure 4.23 and panel (b) of Figure 4.25. The models of feet for the plate and the CTIC are shown in panels (a) and (b) of Figure 4.25 respectively. Once the base of the CTIC is secured to the 4 K plate the interior may be accessed with only partial removal of the 40 K and 4 K shields of the cryostat. This will greatly improve ease of use and enable the sample to be changed without affecting any other aspects of the cryostat. The assembled CTIC is shown in panel (a) of Figure 4.26, and panel (b) of the same figure shows a model of how the CTIC, sample, and optics will fit inside the 4 K chamber.

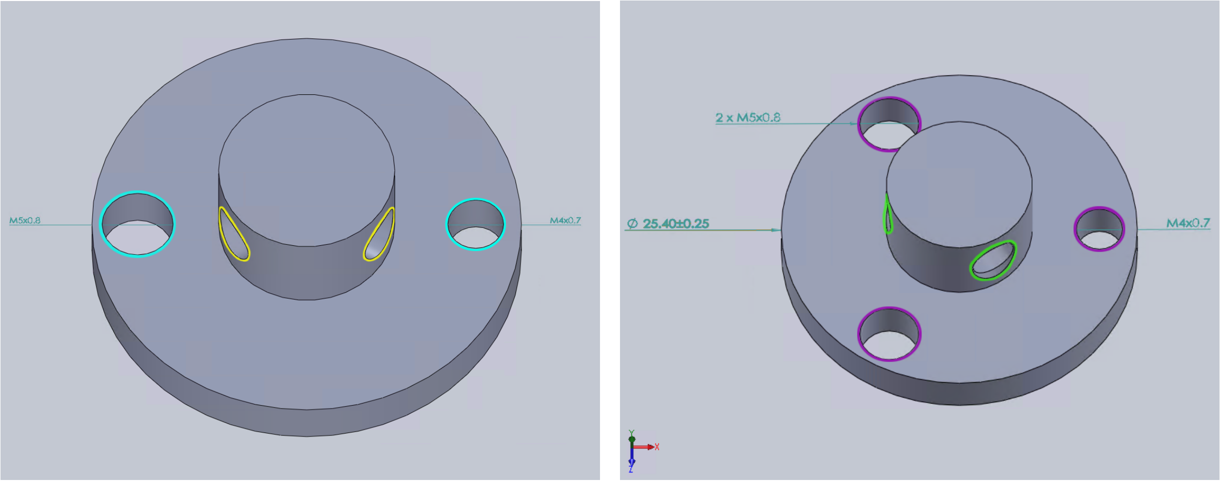

(a) (b)

Figure 4.25: CAD models of the feet for connecting the struts to the cold plate (a) and the base of the CTIC (b). The same circular pattern of three holes in the middle cylinders, shown in yellow and green respectively, allows for connection to the strut itself. Note that only one hole is exactly sized in each case, the other holes are oversized to allow differential contraction.

### 4.5.5 Completed Apparatus

The CTIC apparatus will significantly improve the precision of thermal conductivity measurements of aluminium and CFRP as it will enable isolation of the sample at cryogenic temperatures. It will also function to enable cryogenic measurements of the CTE for different samples. The isolation of the CTIC also means that the thermal cycle will be extended. Consideration must be paid for the thermal transfer in order to facilitate quick turn around. The technical drawings for the CTIC are shown in Appendix C.

The total mass of the current CTIC model and mounting components is 1.43 kg of aluminium. The mass of the sample is 19.5 g for the aluminium sample and 8.19 g for the CFRP, and there are 60 g of stainless steel in the struts. The two retro-reflectors which weigh 5.86 g each put the total weight of the apparatus at approximately 1.5 kg which should be easily supported by the three feet. The thermal mass means that cool-down time will be greatly increased, particularly because of the thermal isolation.

If one assumes that the cold plate is already at 4 K when the CTIC begins to cool (rather

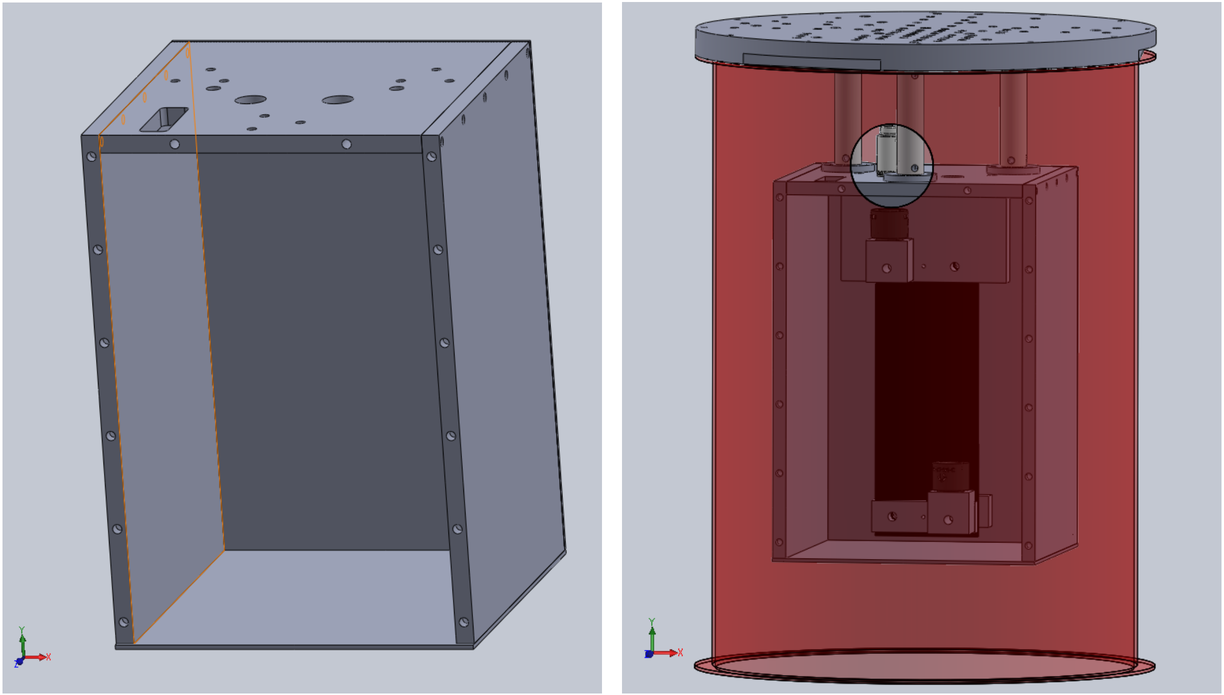

(a) (b)

Figure 4.26: The finalized assembly with the front face made transparent for visibility. Wires and fibre optic cables have been omitted for simplicity. (a) The assembled CTIC with the front face made transparent. (b) The CTIC within the 4 K chamber of the cryostat. Mount and optics are visible within. Note the clearance between the lid of the CTIC and that of the cryostat, this extra clearance can be utilized if longer struts are necessary.

than cooling in tandem) then the integral for cooling time can be expressed as

$$t = \int_4^{T'} \frac{C_V(T)}{\dot{Q}(T)} dT \quad [\tfrac{s}{mol}], \tag{4.24}$$

where $C_V(T)$ is the molar heat capacity, and $\dot{Q}(T)$ is the heat transferred. The units of $Q$ are $\frac{J}{s}$ and the units of $C_V(T)$ are $\frac{J}{mol \cdot K}$ so their quotient has units of $\frac{s}{mol \cdot K}$ and the integral yields the total number of seconds to cool per mol of material. Using Equations 4.2 and 4.14 we can express the cooling time in the form

$$t = \int_4^{T'} \frac{9\, N\, k_B \left(\frac{T}{\theta_D}\right)^3 \int_0^{\theta_D/T'} x^4\, e^x\, (e^x - 1)^{-2} dx}{\frac{A}{L} \int_4^{T'} \kappa(T) dT} dT \quad [\tfrac{s}{mol}]. \tag{4.25}$$

Assuming the struts are 9 cm long and 12.7 mm in outer diameter with an inner diameter

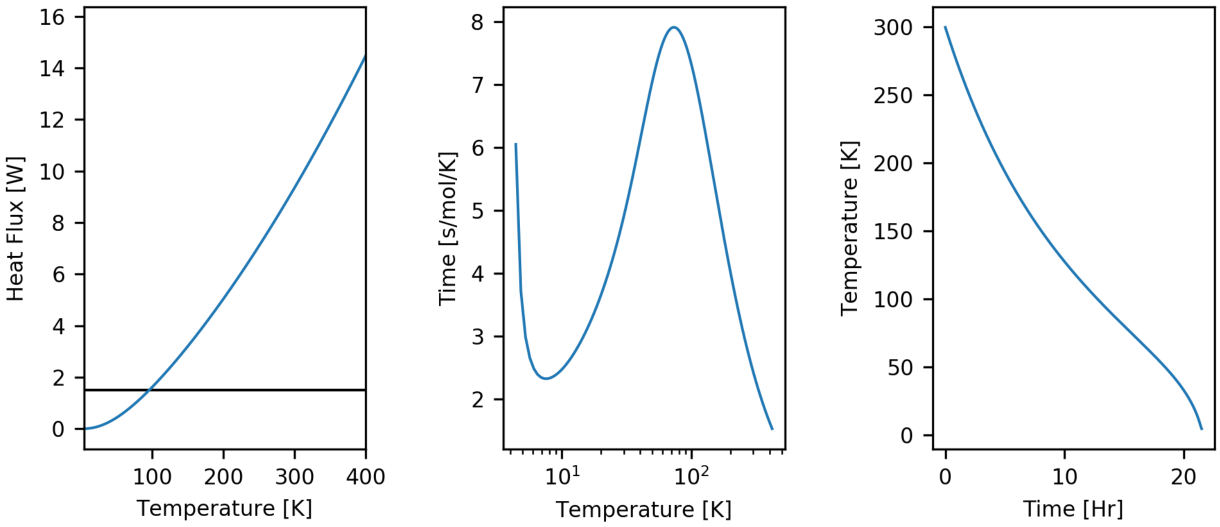

(a) (b) (c)

Figure 4.27: Thermal modeling of the cool-down time for the CTIC. (a) The heat conducted through all three struts as a function of CTIC temperature. The horizontal black line represents the cooling power of the PTC at 4.2K. (b) Time required to change the temperature of a CTIC made of aluminium by one degree Kelvin. Calculated as a combination of the heat conduction through the struts and the heat capacitance of an aluminium block with the mass of the CTIC. (c) Predicted temperature as a function of time for the CTIC.

of 6.604 mm the heat transfer time can be determined. Using trapezoidal integration on the two inner integrals in Equation 4.25 and assuming the entire apparatus is made of aluminium with a Debye temperature of 428 K, the time required to cool a single mol of aluminium by 1 K at each temperature from room temperature to 4 K is shown in Figure 4.27. As the heat transfer becomes greater than the cooling power at 4.2 K the cold plate will warm, and the cooling power of the cryostat increases with temperature. This means that the equilibrium temperature of the cold plate will rise, but the CTIC will remain thermally isolated.

The integral of this function is the cooling time per mole of aluminium, and using the molar mass of aluminium the number of moles of aluminium in the CTIC is [95]

$$n = \frac{m_{Al}}{M_{Mol}} = \frac{1.43kg}{26.9g/mol} = 53.16 \quad [\text{mol}]. \tag{4.26}$$

In Equation 4.26, $m$ represents the mass of the apparatus and the molar mass of aluminium is $M_{Mol}$. The rectangular integration of Equation 4.25 results in a cooling time of 1305 $\frac{s}{mol}$ and therefore the CTIC should cool to 4 K in approximately 21.5 hours. The change of temperature with respect to time is shown in panel (c) of Figure 4.27. This is ∼5 times longer than the current cool-down time for the cryostat, and assumes the CTIC is sunk to a surface constantly held at 4 K, rather than being cooled down simultaneously.

The cool-down period of the cryostat is approximately six times faster than the warmup in general, and a ∼20 hr cool-down would take many days to warmup without the aid of heaters. For quicker turnaround, either the struts could be shortened or widened, or the heaters in place for thermal conductivity measurements need to be used. Alternatively, the trade-off between thermal isolation and cool-down time is one which can be easily altered by use of a thermal braid between the cold plate and the CTIC. This issue is easily resolved and best addressed as experimental data on the turn around time is available.

## 4.6 Conclusions

This experimental design has led to a dedicated materials testing cryostat. The dedicated materials testing cryostat coupled with a nanometer precision laser metrology system has been used to measure the thermal contraction of aluminium and CFRP.

The designs for a thermal isolation box have been presented and preliminary calculations show that despite long cool-down times the current design of the struts can isolate the box from the coldplate without up to ∼100 K before the coldplate will begin to warm. This setup could in principle be used to measure thermal conductivity and CTE simultaneously, though one must be careful in calculation of the mean temperature of the sample for CTE measurements.

The dedicated materials testing cryostat will enable high-precision measurements of materials at cryogenic temperatures in a consistent and reliable manner. An improved sampling rate in the frequency modulated system will enable the tracking of micro-fractures in CFRP samples and the evolution of fracturing may be tracked over many thermal cycles. The repeatability of these experiments will streamline data collection and focus efforts on analyzing and interpreting data rather than the more cumbersome job of experimental setup.

# Chapter 5

# Conclusions and Future Work

The questions faced by modern cosmologists and astronomers require more detailed information about the universe and its constituents both now and through all of cosmic time, and FIR astronomy can make significant contributions to this gap in knowledge. Theoretical models assist astronomers in predicting what may be seen, and consequently what to look for and how to detect it. The feedback of experimental data to theoretical models is an iterative process and astronomers continually seek to improve their understanding by refinements to the theory and improved scientific data. Significant improvements to the scientific data available in the FIR will require cryogenically cooled optics to reduce thermal noise which can dominate the source emission at FIR frequencies, particularly when trying to detect faint signals. Composite materials like CFRP may be used in mechanical and optical instrument assemblies in future space-borne missions. It is therefore important to understand the material properties of CFRP at cryogenic temperatures in order to determine their practical uses, limitations, and to further develop this technology.

In addition to better comprehending the physics of star formation and thermodynamics, the work in this thesis has led to a furthered understanding and appreciation of the rigorous methodologies and procedures involved in collecting, processing, and analyzing experimental data. Many unpredicted problems delayed the progress of these experiments, but in doing so contributed to a more comprehensive design (e.g., temperature monitoring of laser and photonics which was introduced to probe the cause of skips in metrology data). Despite occasional setbacks a more holistic understanding of the theories that motivate the experiments was fostered through painstakingly probing each aspect of the design. Outlined in each of the following sections are summary remarks about the work, including any conclusive results and suggestions for how it can be improved in the future.

## 5.1 Metrology Characterization

Further characterization of the three-phase metrology system may enable it to be utilized for future CTE experiments, but preliminary results using the frequency modulated metrology system indicate more consistency over long periods of time. The three-phase system may still be used for differential measurements, and its operation would enable the frequency modulated system to be used in other experiments. The differential nature of the measurement would also negate the contributions to uncertainty arising from contraction in the mount. However, the problems of long-term drift of the measurements, and the discrete skips in integer wavelengths have not been properly diagnosed, and further use of this prototype system needs to be justified with reliable calibration trials.

Although the first results from the frequency modulated system have been promising, it was run in a sub-optimal configuration and further calibration will be necessary as the configuration is optimized. The system should be verified using similar methods to the three-phase, by comparison against other reliable metrics. Once the processing is done on an FPGA in real time the system should be able to monitor micro-fracturing in the CFRP samples provided their instantaneous velocity is below 387.5 $\frac{\mu m}{s}$. This will enable observation of how the fracturing evolves over numerous thermal cycles.

### 5.1.1 Laser Temperature Control

Understanding the temperature control of the Eblana laser, and the conditions within the room temperature chamber of the dedicated materials cryostat will ensure that the metrology system may be used consistently within the cryostat. Thermally modeling the mounting plate, photonics box, and laser will enable derivation of a way to maintain the laser at a consistent temperature. This may be difficult as Figure 3.19 shows that the plate gets very hot initially which may be problematic, but later helps to insulate from the cold. The laser needs to be isolated during the initial cool-down period and then strongly linked later to keep it from getting too cold. One possible solution would be only to use the metrology system during warmup, but the redundancy of cool-down measurements is useful and thermally cycling CFRPs will alter their properties so it may prove necessary to get continuous data for the entire cycle. Alternatively it is possible that thermally isolating the laser may enable it to remain in operational temperature range, but further testing is needed to determine the effect thermal isolation will have. Modeling the heat transfer through the room temperature apparatus will be necessary for the development of any technique to ensure the laser is consistently within its operable range.

## 5.2 Experimental Design Work

Using modeling software to visualize changes involved a large number of iterations before implementing those changes on the real cryostat. The process of incremental changes to design is critical for a functional setup, and ensured that everything went to plan. The PTC cryostat had minor modifications made to allow for the passing of an armoured fibre-optic cable from the room temperature volume of the cryostat up to the 4 K chamber, thereby enabling measurements of CTE at cryogenic temperatures. A mounting apparatus for the collimators of the fibre-optic cable was designed, machined, and used to demonstrate the possibility of these measurements.

The room temperature volume of the cryostat had two small threaded cavities drilled for mounting the laser, photonics, and fibre-optic cable. Through design of a circuit and programming a micro-controller, room temperature thermometry for the PTC cryostat is now in place and can continue to be used with whatever metrology system is chosen for future trials. This will enable the monitoring of ambient, laser, and photonics temperatures inside the room temperature volume. In the event the laser is operating outside of the prescribed range of temperatures, researchers will be able to monitor this effect and correlate it to any resultant issues in the data.

Most of the mechanical design work has been completed, but the final CTIC product was not manufactured prior to completion of this thesis. The current design of the CTIC and struts is ready to be implemented, though it would be wise to perform more rigorous calculations of cool-down and warmup times before the standoff struts are constructed as they are the most significant design element with respect to thermal modeling. It would also be advisable to do some nominal testing of the heat transfer through a strut of known thermal conductivity to ensure that the measured heat transfer matches theoretical predictions. If there are effects which aren't well approximated with theory it is important to identify and address them before a design is finalized.

The plug for electrical components internal to the CTIC will also need greater consideration to ensure that there are enough ports present for all required thermometry and heaters. Experimenters will need to be conservative with the lengths of wire and path for the wires inside the CTIC as excessive dangling wires may give rise to emf, electrical pickup, thermal shorts, and certainly become an obstruction in swapping samples.

### 5.2.1 Measuring CTE of CFRPs

The CTE of aluminium was successfully measured by both the three-phase and the frequency modulated metrology systems. Though the residuals indicate a slight deviation from analytical models, Figure 4.2 shows that tabulated experimental results also deviate from analytical predictions. The RMS of the residuals between expected contraction of 27 mm of aluminium and the contraction measured by the frequency modulated system were 3.45 and 1.09 $\mu$m for the warmup and cool-down data respectively. This level of precision is nearly at the level required for reliable interferometric results. Static measurements with the system have shown it to be accurate to within ∼50 nm [96], and Figure 3.21 shows an RMS of ∼150 nm for dynamic measurements. Since deviations about zero in the residual are to be expected based on tabulated experimental values [89] the true uncertainty is likely smaller than the RMS of the aluminium contraction residuals.

### 5.2.2 Measuring Thermal Conductivity of CFRPs

No efforts were made to measure the thermal conductivity of CFRPs as time constraints meant thermal contraction measurements were prioritized. Attempts to determine the thermal conductivity of aluminium failed to replicate the canonical values. This is believed to be the result of excess copper tape meant to improve mechanical contact between the thermometers and the sample, which instead modified the thermal pathway and acted as a poor mechanical contact for the thermometers. The poor mechanical contact resulted in unreliable temperature measurements and the heat transfer model did not match observation.

In future the thermometry must be mechanically clamped to the sample to ensure strong thermal contact. The use of the CTIC mount will enable researchers to swap samples out more easily and lead to a dedicated materials testing site with consistent and reliable methods. This will enable researchers to measure both the CTE and the thermal conductivity of samples up to approximately 11 cm long.

## 5.3 Concluding Remarks

Much of the work presented herein has resulted in a better understanding of the experiments conducted and the tools and techniques implemented. Though the progress has often been incremental it is through this process that measurements of the CTE of CFRP were eventually obtained. The experience of working with the equipment has resulted in a greater appreciation of the practical challenges in experimental work, and that knowledge has gone into the design for the CTIC apparatus. The work in this thesis has contributed towards a cryogenic materials testing site which will enable the University of Lethbridge to reliably determine the properties of prospective candidates for space-borne telescope materials.

# References

[1] M. A. Hoskin. The 'great debate': What really happened. *Journal for the History of Astronomy*, 7(3):169–182, October 1976.

[2] Planck Collaboration. Planck 2015 results. XIII. Cosmological parameters. *Astronomy & Astrophysics*, 594:A13, September 2016. Full author list available at: https://arxiv.org/abs/1502.01589.

[3] M. G. G. T. Taylor, N. Altobelli, B. J. Buratti, and M. Choukroun. The Rosetta mission orbiter science overview: the comet phase. *Philosophical Transactions of the Royal Society A: Mathematical, Physical and Engineering Sciences*, 375(2097), May 2017.

[4] D. Hestroffer, P. Sánchez, L. Staron, A. Campo Bagatin, S. Eggl, W. Losert, N. Murdoch, E. Opsomer, F. Radjai, D. C. Richardson, M. Salazar, D. J. Scheeres, S. Schwartz, N. Taberlet, and H. Yano. Small solar system bodies as granular media. *The Astronomy and Astrophysics Review*, 27(1), June 2019.

[5] LIGO Scientific Collaboration and Virgo Collaboration. Observation of gravitational waves from a binary black hole merger. *Physical Review Letters*, 116(6), February 2016. Full author list available at: https://arxiv.org/abs/1602.03837.

[6] European Space Agency. Cosmic vision. *ESA Brochure*, BR-247(1):1–111, 2005.

[7] G. L. Pilbratt, J. R. Riedinger, T. Passvogel, G. Crone, D. Doyle, U. Gageur, A. M. Heras, C. Jewell, L. Metcalfe, S. Ott, and M. Schmidt. Herschel space observatory. *Astronomy and Astrophysics*, 518:L1, July 2010.

[8] J. A. Fernández-Ontiveros, L. Armus, M. Baes, J. Bernard-Salas, A. D. Bolatto, J. Braine, L. Ciesla, I. De Looze, E. Egami, J. Fischer, M. Giard, E. González-Alfonso, G. L. Granato, C. Gruppioni, M. Imanishi, D. Ishihara, H. Kaneda, S. Madden, M. Malkan, H. Matsuhara, M. Matsuura, T. Nagao, F. Najarro, T. Nakagawa, T. Onaka, S. Oyabu, M. Pereira-Santaella, I. Pérez Fournon, P. Roelfsema, P. Santini, L. Silva, J.-D. T. Smith, L. Spinoglio, F. van der Tak, T. Wada, and R. Wu. SPICA and the chemical evolution of galaxies: The rise of metals and dust. *Publications of the Astronomical Society of Australia*, 34, 2017.

[9] NASA Infrared Processing and Analysis Center (IPAC). Near, mid, and far-infrared. `http://www.icc.dur.ac.uk/~tt/Lectures/Galaxies/Images/Infrared/Regions/irregions.html` Accessed: 2019-02-05.

[10] P. R. Roelfsema, H. Shibai, L. Armus, D. Arrazola, M. Audard, M. D. Audley, C.M. Bradford, I. Charles, P. Dieleman, Y. Doi, L. Duband, M. Eggens, J. Evers, I. Funaki, J. R. Gao, M. Giard, A. di Giorgio, L. M. González Fernández, M. Griffin, F. P. Helmich, R. Hijmering, R. Huisman, D. Ishihara, N. Isobe, B. Jackson, H. Jacobs, W. Jellema, I. Kamp, H. Kaneda, M. Kawada, F. Kemper, F. Kerschbaum, P. Khosropanah, K. Kohno, P. P. Kooijman, O. Krause, J. van der Kuur, J. Kwon, W. M. Laauwen, G. de Lange, B. Larsson, D. van Loon, S. C. Madden, H. Matsuhara, F. Najarro, T. Nakagawa, D. Naylor, H. Ogawa, T. Onaka, S. Oyabu, A. Poglitsch, V. Reveret, L. Rodriguez, L. Spinoglio, I. Sakon, Y. Sato, K. Shinozaki, R. Shipman, H. Sugita, T. Suzuki, F. F. S. van der Tak, J. Torres Redondo, T. Wada, S. Y. Wang, C. K. Wafelbakker, H. van Weers, S. Withington, B. Vandenbussche, T. Yamada, and I. Yamamura. SPICA—a large cryogenic infrared space telescope: Unveiling the obscured universe. *Publications of the Astronomical Society of Australia*, 35, 2018.

[11] Marc L. Kutner. *Astronomy: A Physical Perspective*. Cambridge University Press, 2003.

[12] John V. Lindner. SHIFTS: Simulator for the Herschel Imaging Fourier Transform Spectrometer, 2006.

[13] H. Dole, G. Lagache, J.-L. Puget, K. I. Caputi, N. Fernández-Conde, E. Le Floc'h, C. Papovich, P. G. Pérez-González, G. H. Rieke, and M. Blaylock. The cosmic infrared background resolved by Spitzer. *Astronomy & Astrophysics*, 451(2):417–429, May 2006.

[14] Mark H. Jones, Robert J. A. Lambourne, and Stephen Serjeant, editors. *An Introduction to Galaxies and Cosmology*. Cambridge University Press, 2004.

[15] Takao Nakagawa and Hiroshi Murakami. Mid- and far-infrared astronomy mission SPICA. *Advances in Space Research*, 40(5):679–683, January 2007.

[16] SOFIA Team. Stratospheric observatory for infrared astronomy technical information. `https://www.sofia.usra.edu/sites/default/files/SOFIAtech2016.pdf` Accessed: 2019-01-11.

[17] NASA. Hubble's mirror flaw, 2017. `https://www.nasa.gov/content/hubbles-mirror-flaw` Accessed: 2019-08-28.

[18] NASA Infrared Processing and Analysis Center (IPAC). IR atmospheric windows. `http://coolcosmos.ipac.caltech.edu/cosmic_classroom/ir_tutorial/irwindows.html` Accessed: 2019-01-06.

[19] G. Neugebauer, H. J. Habing, R. van Duinen, H. H. Aumann, B. Baud, C. A. Beichman, D. A. Beintema, N. Boggess, P. E. Clegg, T. de Jong, J. P. Emerson, T. N. Gautier, F. C. Gillett, S. Harris, M. G. Hauser, J. R. Houck, R. E. Jennings, F. J. Low, P. L. Marsden, G. Miley, F. M. Olnon, S. R. Pottasch, E. Raimond, M. Rowan-Robinson, B. T. Soifer, R. G. Walker, P. R. Wesselius, and E. Young. The Infrared Astronomical Satellite (IRAS) mission. *The Astrophysical Journal*, 278:L1, March 1984.

[20] N. W. Boggess, J. C. Mather, R. Weiss, C. L. Bennett, E. S. Cheng, E. Dwek, S. Gulkis, M. G. Hauser, M. A. Janssen, T. Kelsall, S. S. Meyer, S. H. Moseley, T. L. Murdock, R. A. Shafer, R. F. Silverberg, G. F. Smoot, D. T. Wilkinson, and E. L. Wright. The COBE mission - its design and performance two years after launch. *The Astrophysical Journal*, 397:420, October 1992.

[21] M. F. Kessler, J. A. Steinz, M. E. Anderegg, J. Clavel, G. Drechsel, P. Estaria, J. Faelker, J. R. Riedinger, A. Robson, B. G. Taylor, and S. Ximénez de Ferrán. The infrared space observatory (ISO) mission. *Astronomy and Astrophysics*, 315(2):L27–L31, 11 1996.

[22] The WMAP Science Working Group. Wilikinson Microwave Anisotropy Probe (WMAP) explanatory supplement, 2003. `https://lambda.gsfc.nasa.gov/product/map/dr1/pub_papers/firstyear/supplement/WMAP_supplement.pdf` Accessed: 2019-08-29.

[23] M. W. Werner, T. L. Roellig, F. J. Low, G. H. Rieke, M. Rieke, W. F. Hoffmann, E. Young, J. R. Houck, B. Brandl, G. G. Fazio, J. L. Hora, R. D. Gehrz, G. Helou, B. T. Soifer, J. Stauffer, J. Keene, P. Eisenhardt, D. Gallagher, T. N. Gautier, W. Irace, C. R. Lawrence, L. Simmons, J. E. Van Cleve, M. Jura, E. L. Wright, and D. P. Cruikshank. The Spitzer space telescope mission. *The Astrophysical Journal*, 154(1):1–9, 9 2004.

[24] Hiroshi Murakami, Hajime Baba, Peter Barthel, David L. Clements, Martin Cohen, Yasuo Doi, Keigo Enya, Elysandra Figueredo, Naofumi Fujishiro, Hideaki Fujiwara, Mikio Fujiwara, Pedro Garcia-Lario, Tomotsugu Goto, Sunao Hasegawa, Yasunori Hibi, Takanori Hirao, Norihisa Hiromoto, Seung Soo Hong, Koji Imai, Miho Ishigaki, Masateru Ishiguro, Daisuke Ishihara, Yoshifusa Ita, Woong-Seob Jeong, Kyung Sook Jeong, Hidehiro Kaneda, Hirokazu Kataza, Mitsunobu Kawada, Toshihide Kawai, Akiko Kawamura, Martin F. Kessler, Do Kester, Tsuneo Kii, Dong Chan Kim, Woojung Kim, Hisato Kobayashi, Bon Chul Koo, Suk Minn Kwon, Hyung Mok Lee, Rosario Lorente, Sin'itirou Makiuti, Hideo Matsuhara, Toshio Matsumoto, Hiroshi Matsuo, Shuji Matsuura, Thomas G. MÜller, Noriko Murakami, Hirohisa Nagata, Takao Nakagawa, Takahiro Naoi, Masanao Narita, Manabu Noda, Sang Hoon Oh, Akira Ohnishi, Youichi Ohyama, Yoko Okada, Haruyuki Okuda, Sebastian Oliver, Takashi Onaka, Takafumi Ootsubo, Shinki Oyabu, Soojong Pak, Yong-Sun Park, Chris P. Pearson, Michael Rowan-Robinson, Toshinobu Saito, Itsuki Sakon, Alberto Salama, Shinji Sato, Richard S. Savage, Stephen Serjeant, Hiroshi Shibai, Mai Shirahata, Jungjoo Sohn, Toyoaki Suzuki, Toshinobu Takagi, Hidenori Takahashi, Toshihiko TanabÉ, Tsutomu T. Takeuchi, Satoshi Takita, Matthew Thomson, Kazunori Uemizu, Munetaka Ueno, Fumihiko Usui, Eva Verdugo, Takehiko Wada, Lingyu Wang, Toyoki Watabe, Hidenori Watarai, Glenn J. White, Issei Yamamura, Chisato Yamauchi, and Akiko Yasuda. The infrared astronomical mission AKARI. *Publications of the Astronomical Society of Japan*, 59(sp2):S369–S376, October 2007.

[25] Edward L. Wright, Peter R. M. Eisenhardt, Amy K. Mainzer, Michael E. Ressler, Roc M. Cutri, Thomas Jarrett, J. Davy Kirkpatrick, Deborah Padgett, Robert S. McMillan, Michael Skrutskie, S. A. Stanford, Martin Cohen, Russell G. Walker, John C. Mather, David Leisawitz, Thomas N. Gautier, Ian McLean, Dominic Benford, Carol J. Lonsdale, Andrew Blain, Bryan Mendez, William R. Irace, Valerie Duval, Fengchuan Liu,

Don Royer, Ingolf Heinrichsen, Joan Howard, Mark Shannon, Martha Kendall, Amy L. Walsh, Mark Larsen, Joel G. Cardon, Scott Schick, Mark Schwalm, Mohamed Abid, Beth Fabinsky, Larry Naes, and Chao-Wei Tsai. The wide-field infrared survey explorer (WISE): Mission description and initial on-orbit performance. *The Astronomical Journal*, 140(6):1868–1881, November 2010.

[26] S. Clark & G. Pilbratt. Herschel science and legacy brochure, 2019. http://sci.esa.int/herschel/61336-herschel-science-and-legacy-brochure/ Accessed: 2019-08-29.

[27] European Space Agency. Planck: The scientific programme, 2005. https://www.cosmos.esa.int/documents/387566/387653/Bluebook-ESA-SCI%282005%291_V2.pdf/d364e30e-f85f-4191-a989-fa6b7527ba55 Accessed: 2019-08-29.

[28] European Space Agency. Planck fact sheet, 2015. http://sci.esa.int/planck/47365-fact-sheet/ Accessed: 2019-05-09.

[29] JWST Team. Webb vital facts. https://jwst.nasa.gov/facts.html Accessed: 2019-02-05.

[30] The Editors of Encyclopaedia Brittanica. Cryogenics. *Encyclopaedia Brittanica*, 2017. https://www.britannica.com/science/cryogenics Accessed March 21, 2019.

[31] William F. Grainger, Roser Juanola-Parramon, Peter A. R. Ade, Matt Griffin, Flo Liggins, Enzo Pascale, Giorgio Savini, and Bruce Swinyard. Demonstration of spectral and spatial interferometry at THz frequencies. *Applied Optics*, 51(12):2202, April 2012.

[32] Eugene Hecht. *Optics (4th Edition)*. Addison-Wesley, 2001.

[33] Andreas Glindemann. Introduction to spatial interferometry. https://www.eso.org/sci/facilities/paranal/telescopes/vlti/tuto/tutorial_spatial_interferometry.pdf Accessed: 2019-08-29.

[34] Frank P. Helmich and R. J. Ivison. FIRI—A Far-Infrared Interferometer. *Experimental Astronomy*, 23(1):245–276, July 2008.

[35] Ulrich Papenburg, Wilhelm Pfrang, G. S. Kutter, Claus E. Mueller, Bernd P. Kunkel, Michael Deyerler, and Stefan Bauereisen. Optical and optomechanical ultralightweight C/SiC components. *SPIE Proceedings: Optical Manufacturing and Testing III*, 3782, November 1999.

[36] J.T. Atkinson and M.J. Lalor. The effect of surface roughness on fringe visibility in optical interferometry. *Optics and Lasers in Engineering*, 1(2):131–146, October 1980.

[37] Alwyn Wootten and A. Richard Thompson. The Atacama large millimeter/submillimeter array. *Proceedings of the IEEE*, 97:1463 – 1471, 8 2009.

[38] Aerotech. Aerotech: Mechanical-bearing direct-drive linear stage (ALS20000 series). https://www.e-motionsupply.com/product_p/als20000.htm Accessed: 2019-02-05.

[39] Renishaw. RLD10 differential interferometer. `https://www.renishaw.com/en/rld10-differential-interferometer--6492` Accessed: 2019-01-11.

[40] Christopher F. McKee and Eve C. Ostriker. Theory of star formation. *Annual Review of Astronomy and Astrophysics*, 45(1):565–687, September 2007.

[41] Richard B. Larson. The physics of star formation. *Reports on Progress in Physics*, 66(10):1651–1697, September 2003.

[42] Derek Ward-Thompson and Anthony P. Whitworth. *An Introduction to Star Formation*. Cambridge University Press, 2011.

[43] James Lequeux. *The Interstellar Medium*. Springer Berlin Heidelberg, 2006.

[44] Howard E. Bond, Edmund P. Nelan, Don A. VandenBerg, Gail H. Schaefer, and Dianne Harmer. HD 140283: A star in the solar neighborhood that formed shortly after the big bang. *The Astrophysical Journal*, 765(1):L12, February 2013.

[45] Dimitris Stamatellos, Simon Goodwin, and Derek Ward-Thompson, editors. *The Labyrinth of Star Formation*.

[46] J. E. Dyson and D. A. Williams. *The Physics of the Interstellar Medium, Second Edition*. Taylor & Francis, 1997.

[47] A. Heger, C. L. Fryer, S. E. Woosley, N. Langer, and D. H. Hartmann. How massive single stars end their life. *The Astrophysical Journal*, 591(1):288–300, July 2003.

[48] Frank H. Shu, Fred C. Adams, and Susana Lizano. Star Formation in Molecular Clouds: Observation and Theory. *Annual Review of Astronomy and Astrophysics*, 25(1):23–81, September 1987.

[49] Gibion Makiwa. *A Study of the Physics of the Interstellar Medium using the Herschel-SPIRE Instrument*. Phd, 2014.

[50] Bastiaan Johan Jonkheid. *Chemistry in Evolving Protoplanetary Disks*. PhD thesis, Leiden University, 2006.

[51] Donald E. Osterbrock. *Astrophysics of gaseous nebulae (A Series of books in astronomy and astrophysics)*. W. H. Freeman, 1974.

[52] Frederick M. Walter. A primer on quantum numbers and spectroscopic notation, 1998. `http://www.astro.sunysb.edu/fwalter/AST341/qn.html` Accessed: August 8th, 2019-08-08.

[53] National Radio Astronomy Observatory. Splatalogue. `https://www.cv.nrao.edu/php/splat/` Accessed: 2019-06-02.

[54] Paul F. Goldsmith and William D. Langer. Population diagram analysis of molecular line emission. *The Astrophysical Journal*, 517(1):209–225, May 1999.

[55] F. F. S. van der Tak, J. H. Black, F. L. Schöier, D. J. Jansen, and E. F. van Dishoeck. A computer program for fast non-LTE analysis of interstellar line spectra. *Astronomy & Astrophysics*, 468(2):627–635, April 2007.

[56] Jr. Harry Y. McSween and Gary R. Huss. *Cosmochemistry*. Cambridge University Press, 2017.

[57] Valerie Illingworth. *Penguin Dictionary of Physics*. Penguin Books Ltd, 2009.

[58] Encyclopædia Britannica Britannica Academic. Stellar classification., 2011. `https://www.britannica.com/science/stellar-classification` Accessed: 2019-08-08.

[59] C. J. Cyganowski, B. A. Whitney, E. Holden, E. Braden, C. L. Brogan, E. Churchwell, R. Indebetouw, D. F. Watson, B. L. Babler, R. Benjamin, M. Gomez, M. R. Meade, M. S. Povich, T. P. Robitaille, and C. Watson. A catalog of extended green objects in the glimpse survey: A new sample of massive young stellar object outflow candidates. *The Astronomical Journal*, 136(6):2391–2412, November 2008.

[60] Robert A. Benjamin, E. Churchwell, Brian L. Babler, T. M. Bania, Dan P. Clemens, Martin Cohen, John M. Dickey, Rémy Indebetouw, James M. Jackson, Henry A. Kobulnicky, Alex Lazarian, A. P. Marston, John S. Mathis, Marilyn R. Meade, Sara Seager, S. R. Stolovy, C. Watson, Barbara A. Whitney, Michael J. Wolff, and Mark G. Wolfire. GLIMPSE. I. an SIRTF legacy project to map the inner galaxy. *Publications of the Astronomical Society of the Pacific*, 115(810):953–964, August 2003.

[61] Ed Churchwell, Brian L. Babler, Marilyn R. Meade, Barbara A. Whitney, Robert Benjamin, Remy Indebetouw, Claudia Cyganowski, Thomas P. Robitaille, Matthew Povich, Christer Watson, and Steve Bracker. The Spitzer/GLIMPSE surveys: A new view of the milky way. *Publications of the Astronomical Society of the Pacific*, 121(877):213–230, March 2009.

[62] C. J. Cyganowski, C. L. Brogan, T. R. Hunter, and E. Churchwell. A Class I and Class II CH3OH maser survey of EGOs from the GLIMPSE survey. *The Astrophysical Journal*, 702(2):1615–1647, August 2009.

[63] C. J. Cyganowski, C. L. Brogan, T. R. Hunter, R. Smith, J. M. D. Kruijssen, I. A. Bonnell, and Q. Zhang. Simultaneous low- and high-mass star formation in a massive protocluster: Alma observations of g11.92-0.61. *Monthly Notices of the Royal Astronomical Society*, 468(3):1–17, February 2017.

[64] J. D. Ilee, C. J. Cyganowski, C. L. Brogan, T. R. Hunter, D. H. Forgan, T. J. Haworth, C. J. Clarke, and T. J. Harries. G11.92–0.61 MM 1: A fragmented Keplerian disk surrounding a proto-O star. *The Astrophysical Journal*, 869(2):L24, December 2018.

[65] Allison P. M. Towner, Crystal L. Brogan, Todd R. Hunter, Claudia J. Cyganowski, and Rachel K. Friesen. SOFIA *FORCAST* photometry of 12 extended green objects in the milky way.

[66] Canadian Astronomy Data Center. JCMT science archive, 2019. http://www.cadc-ccda.hia-iha.nrc-cnrc.gc.ca/en/search/?collection=JCMT&noexec=true Accessed: 2019-08-28.

[67] Locke D. Spencer. Spectral characterization of the Herschel SPIRE photometer, 2005.

[68] J. D. Ilee, C. J. Cyganowski, P. Nazari, T. R. Hunter, C. L. Brogan, D. H. Forgan, and Q. Zhang. G11.92-0.61 MM1: a Keplerian disc around a massive young proto-O star. *Monthly Notices of the Royal Astronomical Society*, 462(4):4386–4401, August 2016.

[69] Andrew J. Fleming. A review of nanometer resolution position sensors: Operation and performance. *Sensors and Actuators A: Physical*, 190:106–126, February 2013.

[70] David Naylor, Ian Veenendaal, Brad Gom, and Adam Christiansen. A fibre-fed laser interferometer for optical metrology at cryogenic temperatures. *SPIE Proceedings: Photonic Instrumentation Engineering V*, 10539, February 2018.

[71] Ian Veenendaal, David Naylor, Brad Gom, Trevor Fulton, Adam Christiansen, Willem Jellema, Martin Eggens, and Peter Ade. A novel design for a cryogenic, angle-scanned, fabry-pérot interferometer. *SPIE Proceedings: Advances in Optical and Mechanical Technologies for Telescopes and Instrumentation III*, 10706, July 2018.

[72] Locke D. Spencer; Ian T. Veenendaal; David A. Naylor; Brad G. Gom; Geoffrey R. H. Sitwell; Anthony I. Huber; Adam Christiansen; Chris S. Benson; Sudhakar Gunuganti; Martyn Jones; Richard Day; David Walker; Navid Zobeiry; Anoush Poursartip. Composite material evaluation at cryogenic temperatures for applications in space-based far-infrared astronomical instrumentation. *SPIE Proceedings: Advances in Optical and Mechanical Technologies for Telescopes and Instrumentation III*, 10706, July 2018.

[73] Eblana Photonics. DX1-DM laser module with current and TEC control user manual, 2018. http://www.cybel-llc.com/wp-content/uploads/2016/01/DX-1-Manual-3.pdf Accessed: 2019-08-30.

[74] Lori Stover. Mounted retroreflector prisms, 2013. https://www.thorlabs.com/newgrouppage9.cfm?objectgroup_id=4265&pn=PS974M-C Accessed: 2019-05-14.

[75] Renishaw. Rpi20 parallel interface user's guide, 2017. https://resources.renishaw.com/en/details/installation-users-guide-rpi20-parallel-interface--96288 Accessed: 2019-08-30.

[76] Newport. Actively damped smarttables® with IQ damping technology®. https://www.newport.com/f/smarttable-active-damped-optical-tables Accessed: 2019-08-28.

[77] Eblana Photonics. DX1 - sensing EP1550-DM-DX1, 2013. https://rpmclasers.com/wp-content/uploads/products/EP1550-DM-DX1.pdf Accessed: 2019-08-28.

[78] PJRC Electronic Projects. Teensy LC - low cost. https://www.pjrc.com/teensy/teensyLC.html#specs Accessed: 2019-08-29.

[79] CMR-Direct. GE varnish. `http://www.cmr-direct.com/en/ge-varnish-2` Accessed: 2019-05-15.

[80] Adam J. Christiansen, David A. Naylor, Ian T. Veenendaal, and Brad G. Gom. A frequency-modulated laser interferometer for nanometer-scale position sensing at cryogenic temperatures. *SPIE Proceedings: Photonic Instrumentation Engineering VI*, 10925, March 2019.

[81] P.C. McDonald, E. Jaramillo, and B. Baudouy. Thermal design of the CFRP support struts for the spatial framework of the Herschel space observatory. *Cryogenics*, 46(4):298–304, April 2006.

[82] Ian Veenendaal. A cryogenic test facility, 2016.

[83] Keith Stowe. *An Introduction to Thermodynamics and Statistical Mechanics*. Cambridge University Press, 2012.

[84] Walter Greiner. *Thermodynamics and statistical mechanics (Classical theoretical physics)*. Springer-Verlag, 1995.

[85] D. R. Chipman. Temperature dependence of the Debye temperatures of aluminum, lead, and beta brass by an x-ray method. *Journal of Applied Physics*, 31(11):2012–2015, 1960.

[86] Herbert B. Callen. *Thermodynamics*. John Wiley & Sons Inc, 1963.

[87] Hai-Dong Wang. *Theoretical and Experimental Studies on Non-Fourier Heat Conduction Based on Thermomass Theory*. Springer-Verlag GmbH, 2014.

[88] Alan J. Chapman. *Fundamentals of Heat Transfer*. Pearson, 1987.

[89] Jack W. Ekin. *Experimental Techniques for Low-Temperature Measurements*. Oxford University Press, 2006.

[90] Frank Kreith and Mark S. Bohn. *Principles of Heat Transfer*. CL Engineering, 2000.

[91] M. W. Zemansky and Richard H. Dittman. *Heat and Thermodynamics*. McGraw-Hill College, 1996.

[92] National Institute for Standards and Technology. Index of material properties. `https://trc.nist.gov/cryogenics/materials/materialproperties.htm` Accessed: 2019-08-28.

[93] James Tuttle, Edgar Canavan, and Amir Jahromi. Cryogenic thermal conductivity measurements on candidate materials for space missions. *Cryogenics*, 88:36–43, December 2017.

[94] McMaster Carr. Stainless steel tubing. `https://www.mcmaster.com/standard-metal-tubing` Accessed: 2019-08-28.

[95] Gordon M. Barrow. *Physical chemistry*. McGraw-Hill, 1979.

[96] Locke D. Spencer, Adam Christiansen, Ian T. Veenendaal, Sudhakar Gunuganti, David A. Naylor, Brad G. Gom, Geoffrey R. H. Sitwell, Navid Zobeiry, and Anoush Poursartip. Evaluation of composite materials at cryogenic temperatures, 2019. In press.

# Appendix A

# Brief Overview of Position Metrology Systems

## Resistive Strain Sensors

The first detectors listed in Table 3.1 are resistive strain sensors which use a metal foil formed in a zig-zag pattern between two insulating surfaces. Strains applied to the detector cause deformations in the foil which in turn result in a change of resistance. Measuring the change in resistance thereby enables a determination of the change in length between the two insulating surfaces [69].

## Capacitive Sensors

Capacitive devices may also be used for displacement measurements. The capacitance of a parallel plate capacitor is given by [69]

$$C = \frac{\epsilon_0 \epsilon_r A_{Cap}}{d}, \tag{A.1}$$

with $\epsilon_0$ and $\epsilon_r$ the permittivity of free space and the relative permittivity of the dielectric respsectively, $A_{Cap}$, the overlapping area of the sensors, and $d$ is the distance between them. The capacitance can therefore be altered by changing the separation between the plates, or moving them laterally to change the effective area. Alternatively, a moving dielectric could also be used to affect the relative permittivity. In these ways the displacement of the plates is measurable through changes in capacitance, which in turn may be determined by measuring the voltage between the plates [69].

## Eddy-Current Sensors

Eddy-current sensors operate on the principle of electromagnetic induction. An alternating current run through a coil of wire will give rise to a changing magnetic field, which in turn induces circulating eddy-currents in the target. The distance between the probe and the target will determine the strength of the induced eddy currents [69].

## LVDT Sensors

The operating principle of a linear variable displacement transformer (LVDT) relies on a permeable material which couples the magnetic flux from a coil of wire driven by an alternating current, to one of two other coils. If the three coils are centered about the same axis, then the fraction of the permeable core along that axis will determine the coupling between the central coil, and either one of the other two coils. By monitoring the induced voltage on the two sensor coils, the position of the core may be determined [69].

## Optical Encoders

Optical encoders consist of a scale and a read-head. The scale uses bands of reflective and non-reflective materials, and light from a laser-diode is scanned along the scale. The amount of light reflected back and detected at the head will depend on whether the scanned portion of the scale is reflective or not. The correspondance between power received and distance along the scale enables measurements of position [69].

## Laser Interferometers

Finally, and most pertinently to this work, laser interferometers use the wave-like nature of light to determine displacement. The interference between two coherent beams of light is determined by the phase difference between the two beams. The phase difference is in turn determined by the relative difference in path traveled by the two beams, and may therefore be used to determine the displacement along one path [69].

Each of these devices may work in a number of configurations with their own benefits and drawbacks. For a more comprehensive overview of these devices please see Fleming 2013 [69] and references contained therein.

# Appendix B

# Experiment Logs

This appendix is a work journal documenting the trials for thermal conductivity and thermal contraction which didn't make into the main body of the thesis. The errors made here may lend insight into future experiments, and I felt it worthwhile to document the failures in experimentation so that they may be avoided in future.

## May 12th, 2018

The most promising trial run so far is from May 12th, when only the upper heater was used. Setpoint temperature was steadily increased and the heater warmed the sample smoothly. Unfortunately the 4K plate temperature wasn't recorded for this trial so all heat conduction equations assume the plate to be at 4K.

The PTC was switched off, but the program continued to take data and so only the portion up until the blue dotted line is of particular interest. Eventually the heater was also turned off but data went out of range for the calibration before this happened so we do not see the effect in the data.

The heat supplied is merely the power through the heater, and the heat conducted out was calculated for each of the four thermometers (each has four phosphour bronze wires), the two heaters (each has two copper wires), and the bolt (stainless steel) which affixes the sample to the 4K plate.

The data for May 12th are shown in the body of the thesis in Figure 4.5.

## May 15th, 2018

The second trial was the first in which both heaters were used. Run on May 15th, the test involved monitoring the temperatures on cool-down with no setpoints at all. The subsequent trial on May 16th was the warmup and setpoints were used, however not enough wait time was used to ensure thermal equilibrium of the sample. Unfortunately temperature recording was only started after the sample had cooled to $\sim$145 K.

The net heat flux supplied is necessarily negative since heat is conducted out of the system as it cools.

Of the thermometers, X53022 is mounted on the 40K plate, and both of X63595 and X72808 were both mounted to the 4K plate. The disagreement between X63595 and X72808 indicates that one of them is mis-calibrated or has poor thermal contact with the plate it is assumed to be X72808, since X63595 reads  3.7K which is closer to what we expect than the 6K that X72808 reads.

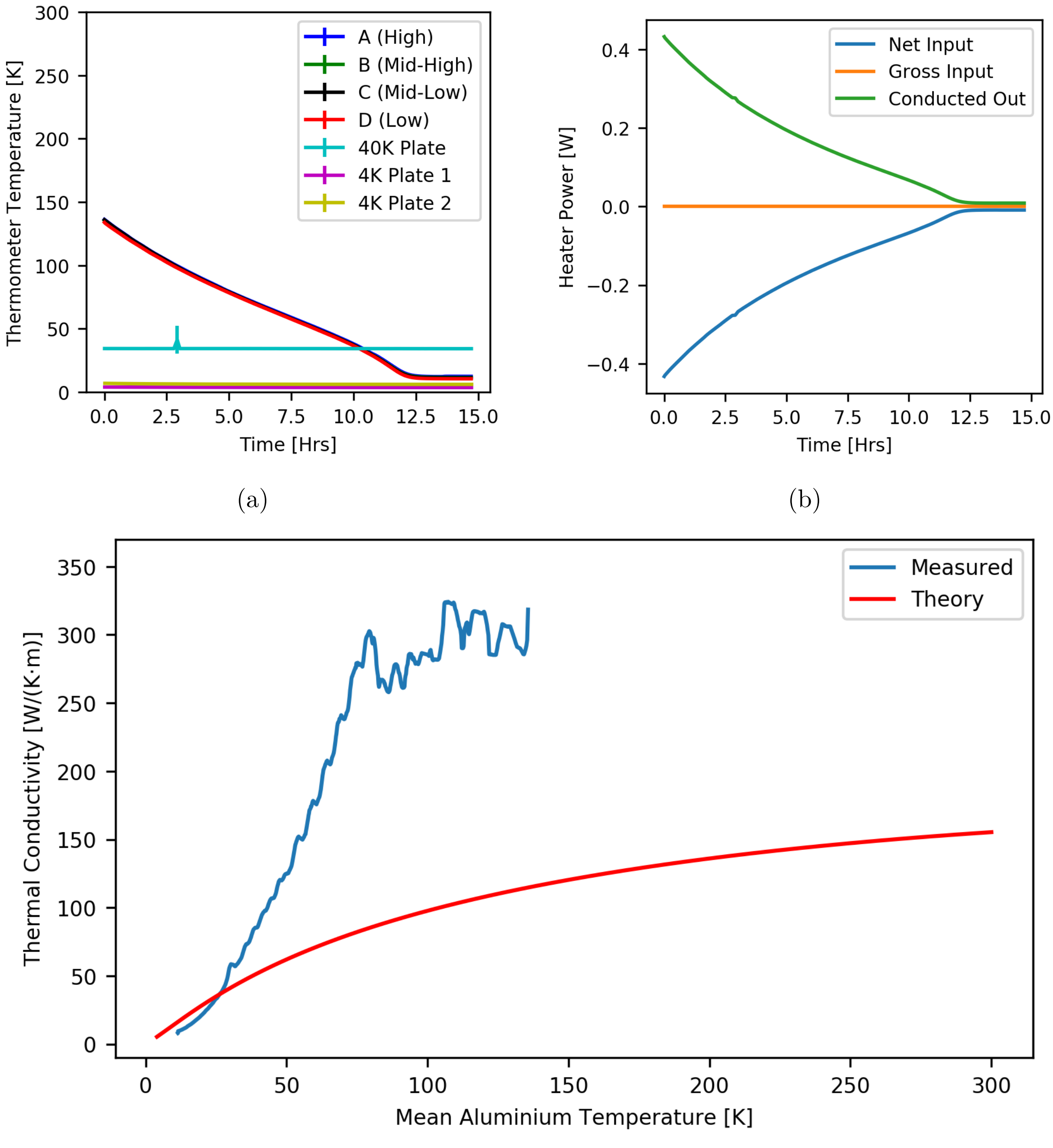

(a)

(b)

(c)

Figure B.1: Thermal conductivity experimental data for May 15th, 2018. (a) Temperature data for cryogenic thermal conductivity measurements on May 15th, 2018. (b) Supplied power from the heater and calculated heat dissipation in the cryogenic thermal conductivity measurements on May 15th, 2018. (c) Calculated thermal conductivity from experiments on May 15th, 2018.

## May 16th, 2018

The warmup data from the trial run over May 15th. Setpoint temperatures are identifiable in the temperature data.

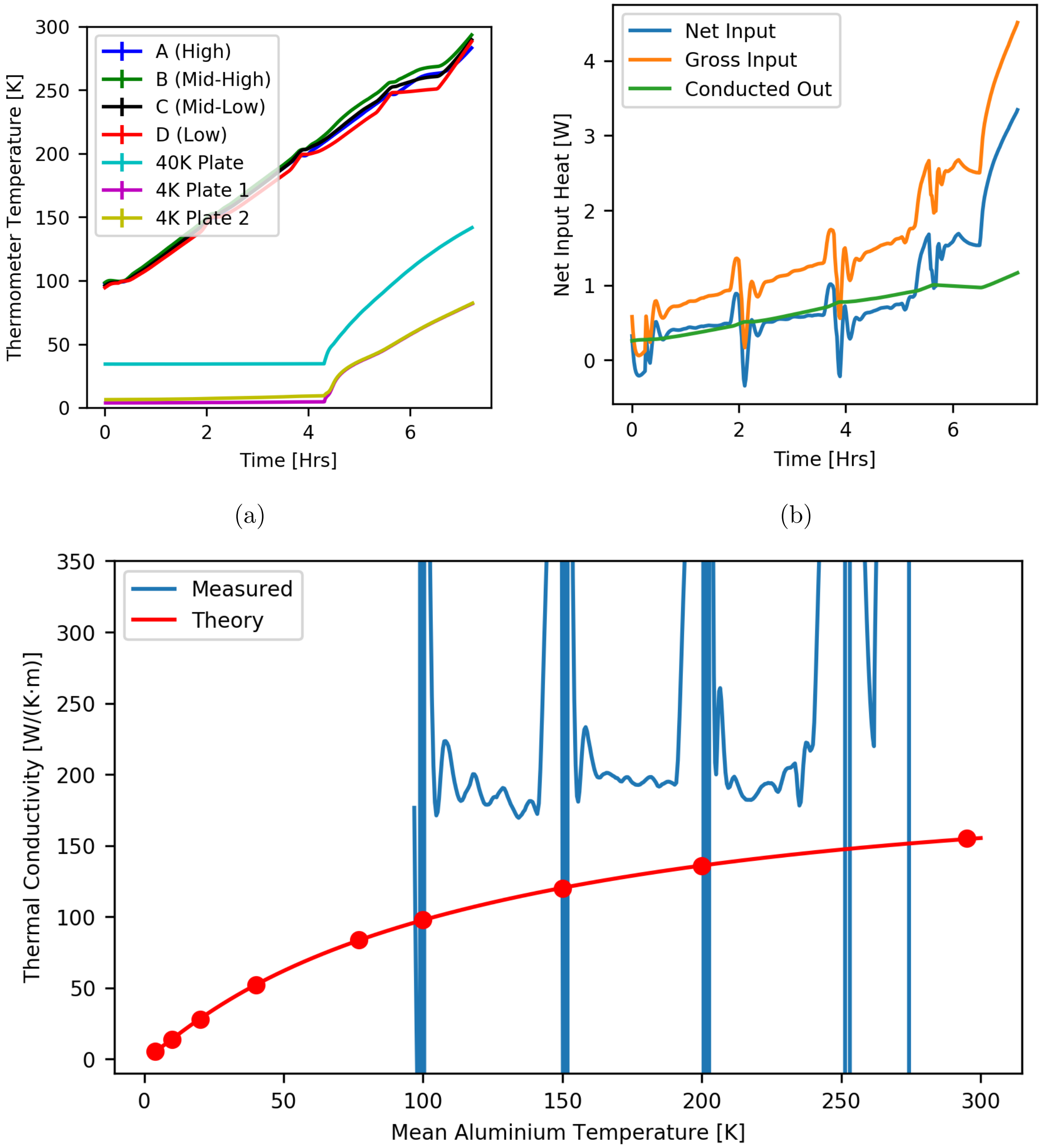

(a)

(b)

(c)

Figure B.2: Thermal conductivity experimental data for May 16th, 2018. (a) Temperature data for cryogenic thermal conductivity measurements on May 16th, 2018. (b) Supplied power from the heater and calculated heat dissipation in the cryogenic thermal conductivity measurements on May 16th, 2018. (c) Calculated thermal conductivity from experiments on May 16th, 2018.

## May 17th, 2018

On May 17th the sample was cooled, using setpoints on the way down (a negative in the code meant that setpoints were reversed i.e. Temp A $<$ Temp D). Using setpoints on the way down extends cool-down time from 70000s to 90000s ( 19.4hrs to 25hrs). Because this trial was begun on a Thursday, the warmup setpoints were begun on Friday the 18th. Once getting warm the system was allowed to cool once more so that a final test could be run with just the top heater again (to compare against results from May 12th), but I panicked about the compressor pressures and shut down the system.

The results here are quite messy given the number of times we cycled through any given temperature. It's perhaps worth noting the curve from 20K - 75K matches closely (qualitatively at least) to the same range of data from May 15th, and May 22nd.

Because the data for May 17th were often near to steady-state, I chopped out pieces of the data where the temperatures and heater inputs were near-constant and assumed then that the whole sample was in thermal equilibrium. However, even with this "Cherry-Picked" data the results were less than encouraging.

The heat input to the system was not generally as consistent as the temperature, however in a few cases it remained quite steady for an extended period.

Note that even in the 25K and 275K where the system is in equilibrium for an extended period of time, we still do not match the canonical values for thermal conductivity.

The data for May 17th are shown in the body of the thesis in Figure 4.6.

## May 21st, 2018

On May 21st the heater was set to have a high setpoint, merely as a means by which to bring the whole system back to room temperature more quickly.

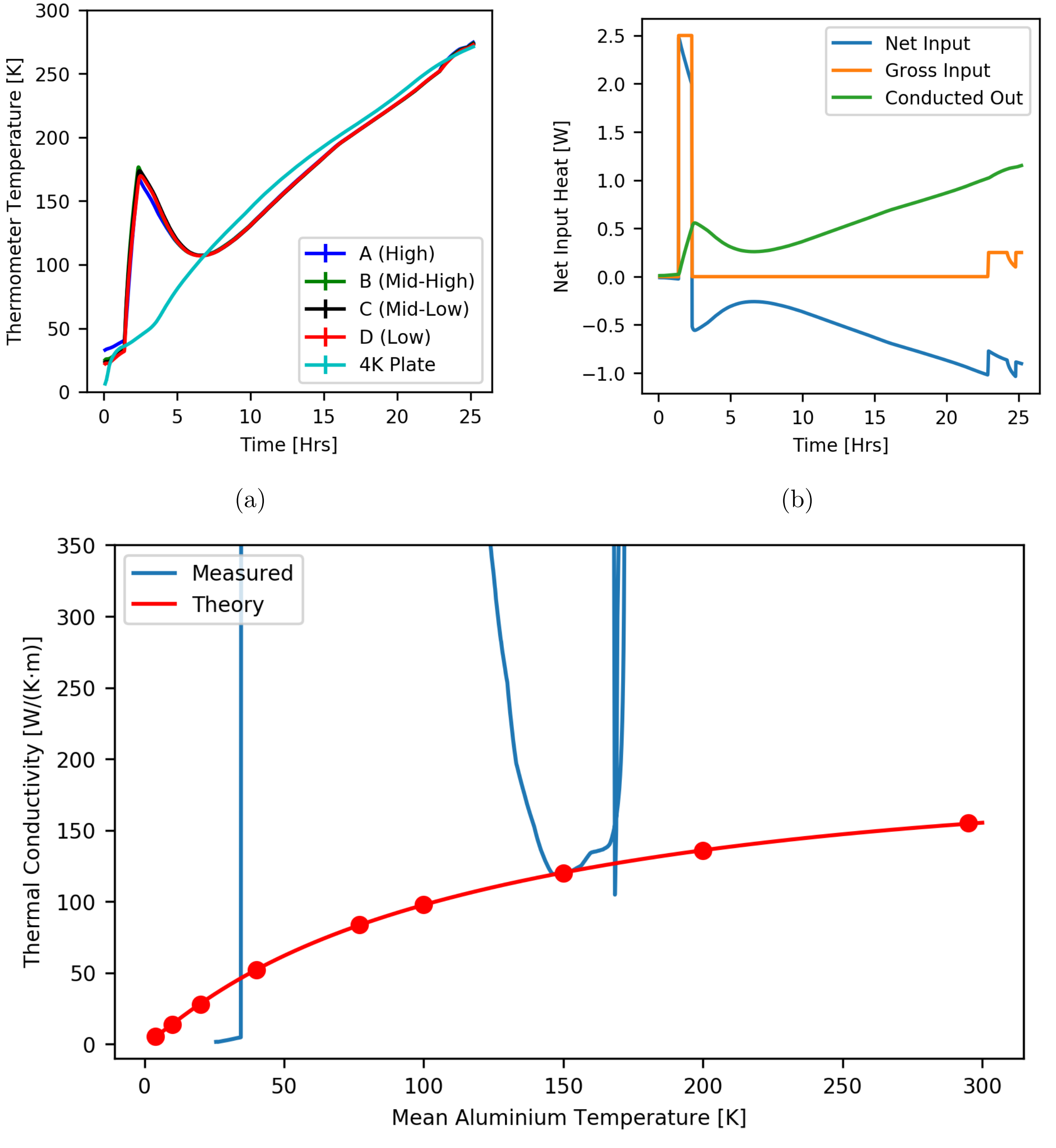

(a)

(b)

(c)

Figure B.3: Thermal conductivity experimental data for May 21st, 2018. (a) Temperature data for cryogenic thermal conductivity measurements on May 21st, 2018. (b) Supplied power from the heater and calculated heat dissipation in the cryogenic thermal conductivity measurements on May 21st, 2018. (c) Calculated thermal conductivity from experiments on May 21st, 2018.

## May 22nd, 2018

On May 22nd, rather than opening up the cryostat we opted to cool back down (nullifying the warmup through May 21st) for the final test that never was completed on the 20th.

It's rather interesting to note that through the first few hours of the cool-down Thermometer A was the quickest to cool. This indicates that there must be a rather significant thermal link between the floating end of our sample, where A is mounted, and the 4K plate that we aren't accounting for. It may be the case that the lengths of wire used to calculate heat conduction out of the sample are over-stated.

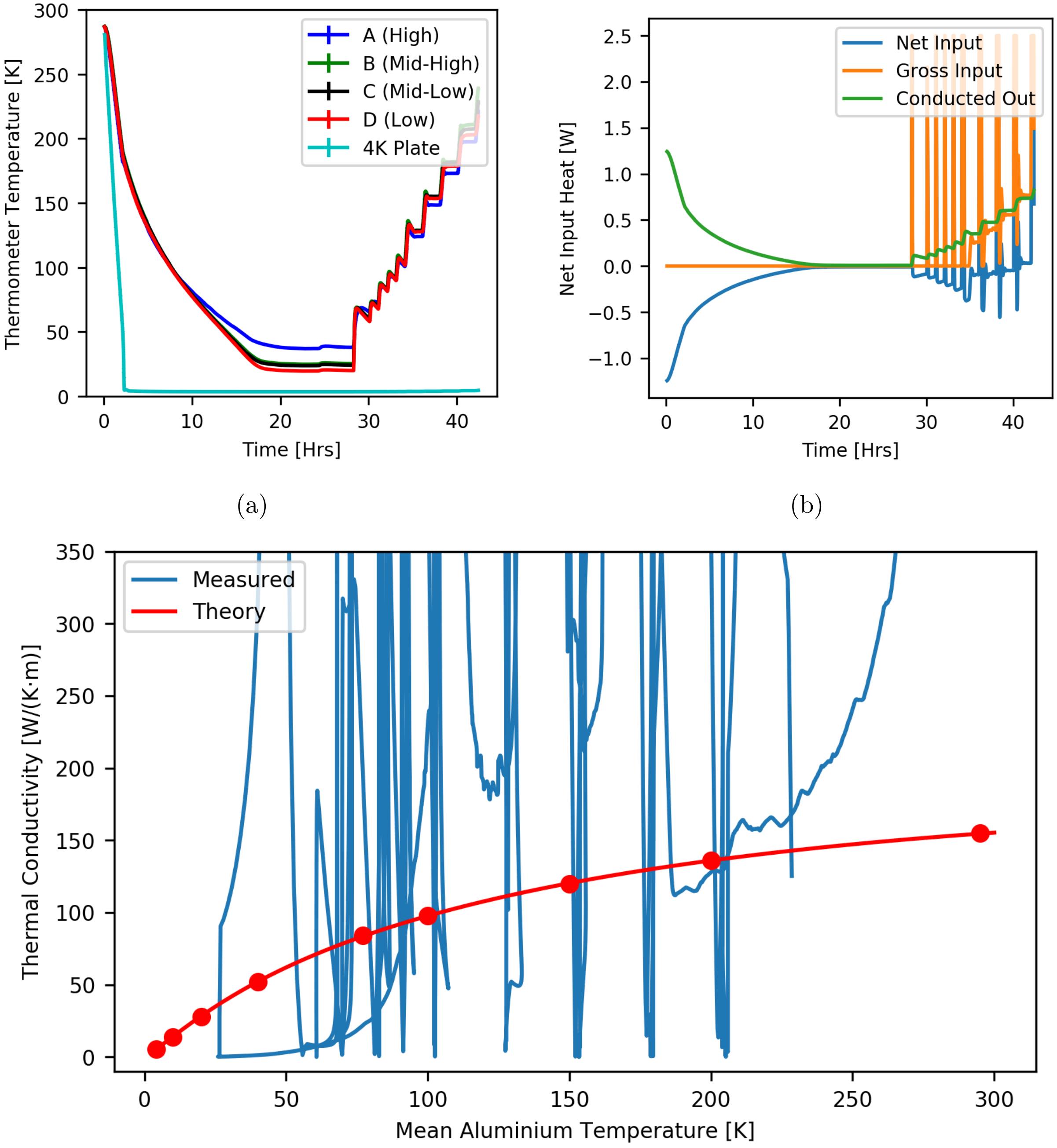

(a)

(b)

(c)

Figure B.4: Thermal conductivity experimental data for May 22nd, 2018. (a) Temperature data for cryogenic thermal conductivity measurements on May 22nd, 2018. (b) Supplied power from the heater and calculated heat dissipation in the cryogenic thermal conductivity measurements on May 22nd, 2018. (c) Calculated thermal conductivity from experiments on May 22nd, 2018.

## May 25th, 2018

On May 25th the final trial for thermal conductivity of Aluminium was run. The copper tape was replaced with kapton to avoid shortening thermal path lengths, and the profile of the tape was minimized.

Note that once thermalized at low temperature the thermometers read in a peculiar order. The warmest is D, which resides closest to the cold plate. This is possibly an indication of low thermal contact.

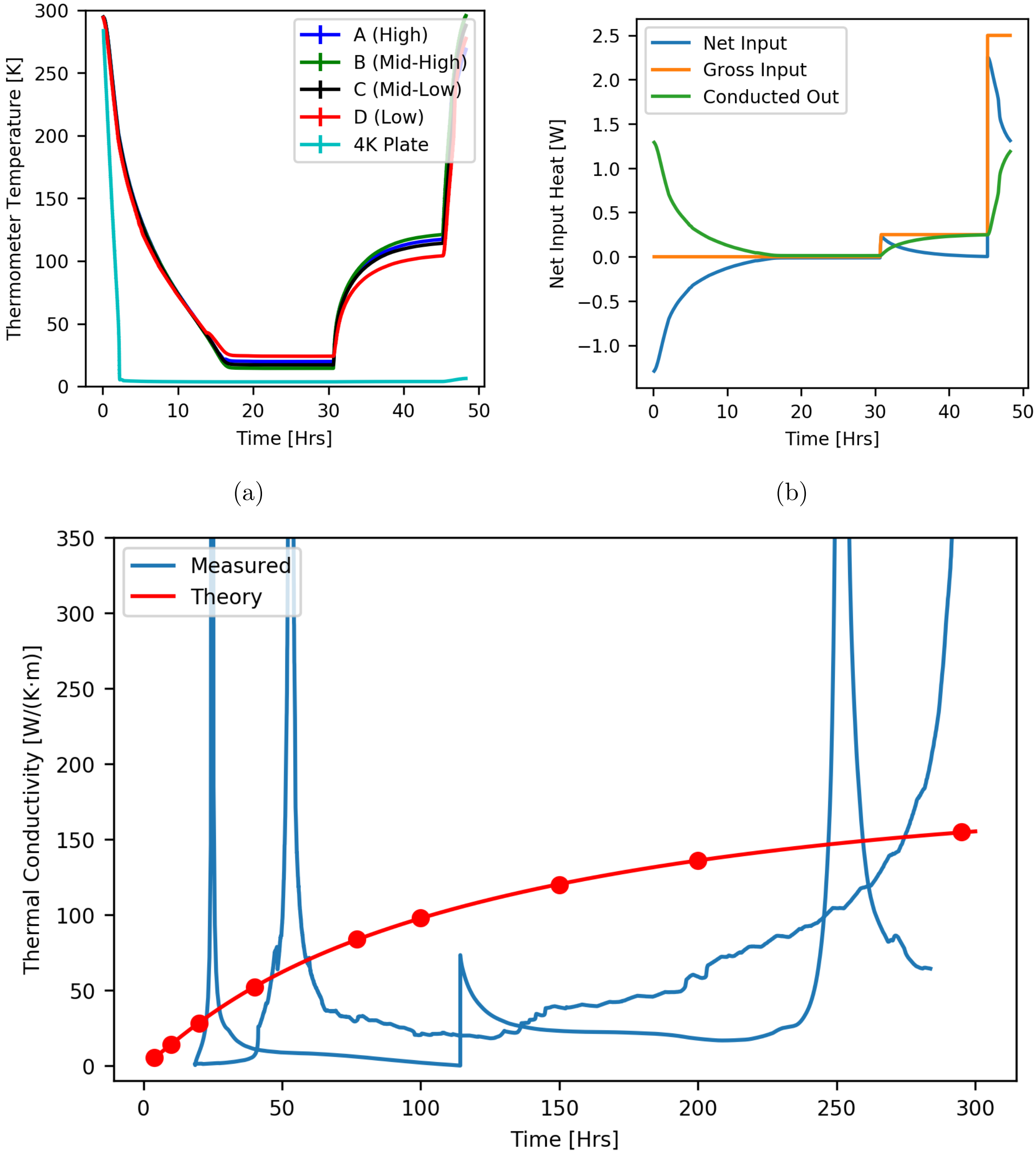

(a)

(b)

(c)

Figure B.5: Thermal conductivity experimental data for May 25th, 2018. (a) Temperature data for cryogenic thermal conductivity measurements on May 25th, 2018. (b) Supplied power from the heater and calculated heat dissipation in the cryogenic thermal conductivity measurements on May 25th, 2018. (c) Calculated thermal conductivity from experiments on May 25th, 2018.

## June 9th, 2018

Given the relative success of our first cool-down we decided to go ahead with a CFRP measurement. Unfortunately the holes bored in the CFRP sample were for M3 bolts, and no M3 bolts were long enough to penetrate all necessary components (retrorefoector mount, front clamp, CFRP, back clamp, spring washer, and nut). Since the CFRP couldn't be analyzed the sample of aluminium was used again.

The large 'skips' in data which were previously observed again manifested in these data.

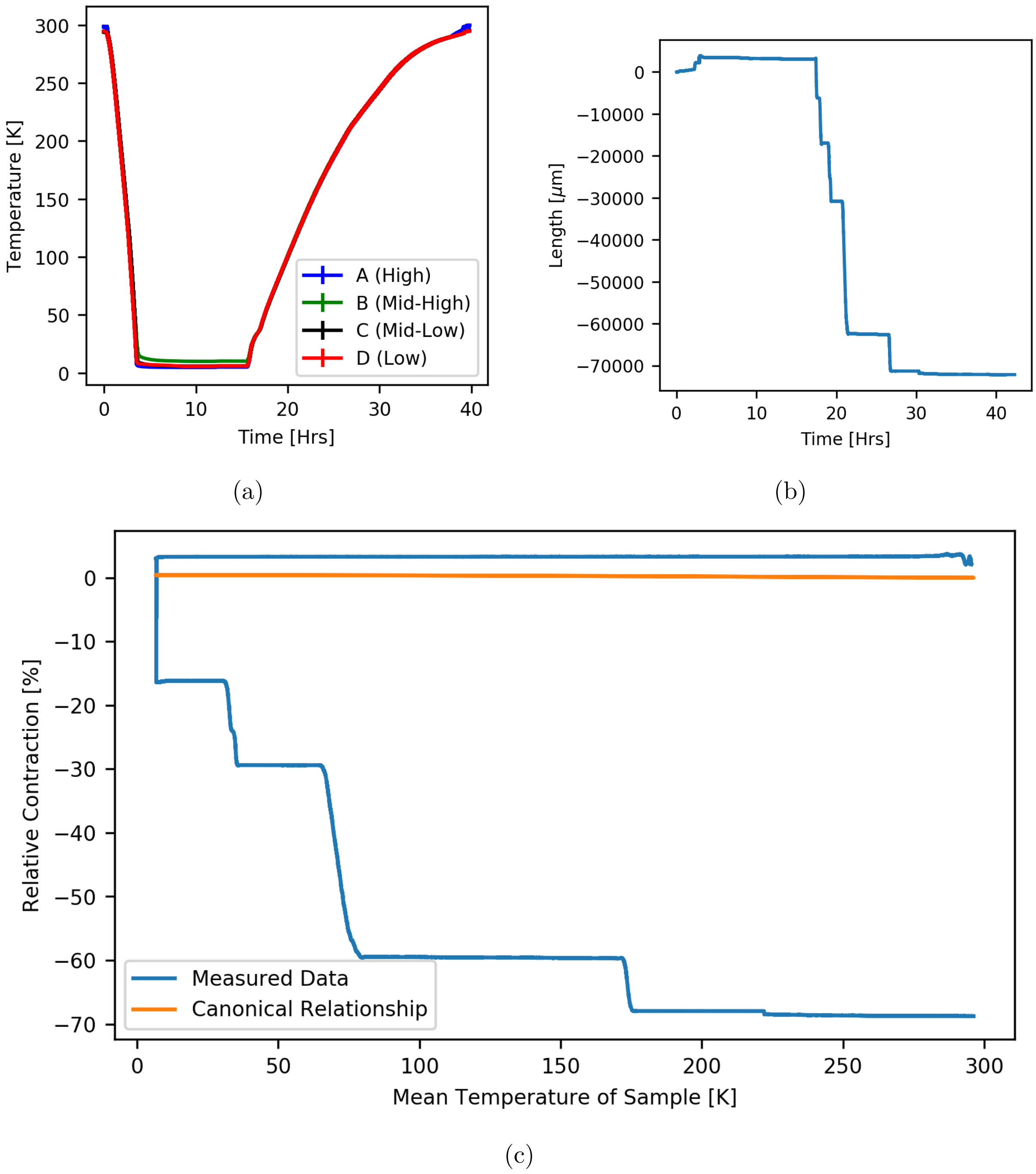

(a)

(b)

(c)

Figure B.6: Data for cryogenic thermal length contraction experiment on June 9th, 2018. (a) Temperature data for cryogenic thermal contraction measurements on June 9th, 2018. (b) Change in length recorded by the three-phase metrology system on June 9th, 2018. (c) Thermal contraction for the trial of June 9th, 2018.

## June 11th, 2018

On June 11th the CFRP holes were milled out to M4 and we were able to proceed with the experiment. Unfortunately, there were also a number of issues plaguing this data. The spikes which have since been corrected for were still present and there is a rapid contraction of 11mm which can't reasonably be explained by thermal contraction.

There are also intermittent spikes in the data which seem to reach a consistent peak. These spikes were masked and ignored to begin with, and now it seems that they have been corrected by Adam as they were a problem caused by bit conversion in the FPGA.

It became apparent by the end of this trial that either mechanical slipping was causing the photonics to miss fringes, or that something else was amiss.

Upon opening the cryostat it was found that two of the thermometers on the sample were detached. The temperature data shown for the thermometer that remained attached is shown in black.

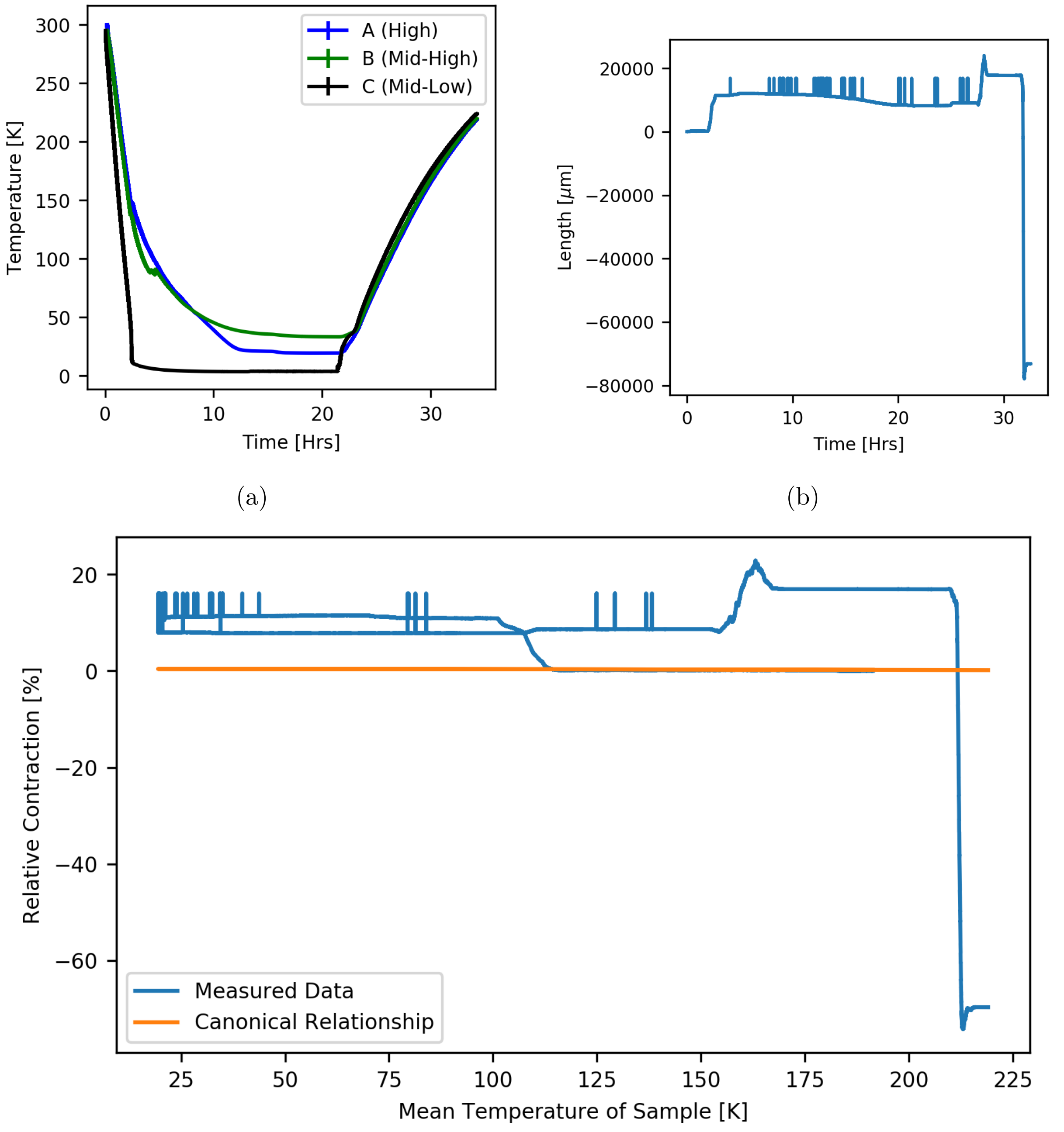

(a)

(b)

(c)

Figure B.7: Data for cryogenic thermal length contraction experiment on June 11th, 2018. (a) Temperature data for cryogenic thermal contraction measurements on June 11th, 2018. (b) Change in length recorded by the three-phase metrology system on June 11th, 2018. (c) Thermal contraction for the trial of June 11th, 2018.

## June 20th, 2018

On the night of June 20th a sample of aluminium was left in the opened cryostat overnight to sit at room temperature in C814.

There are a number of ’hiccups’ in this data set, but when they’re corrected for the data agree very well with what we’d expect (settling back to the baseline length when returning to the baseline temperature).

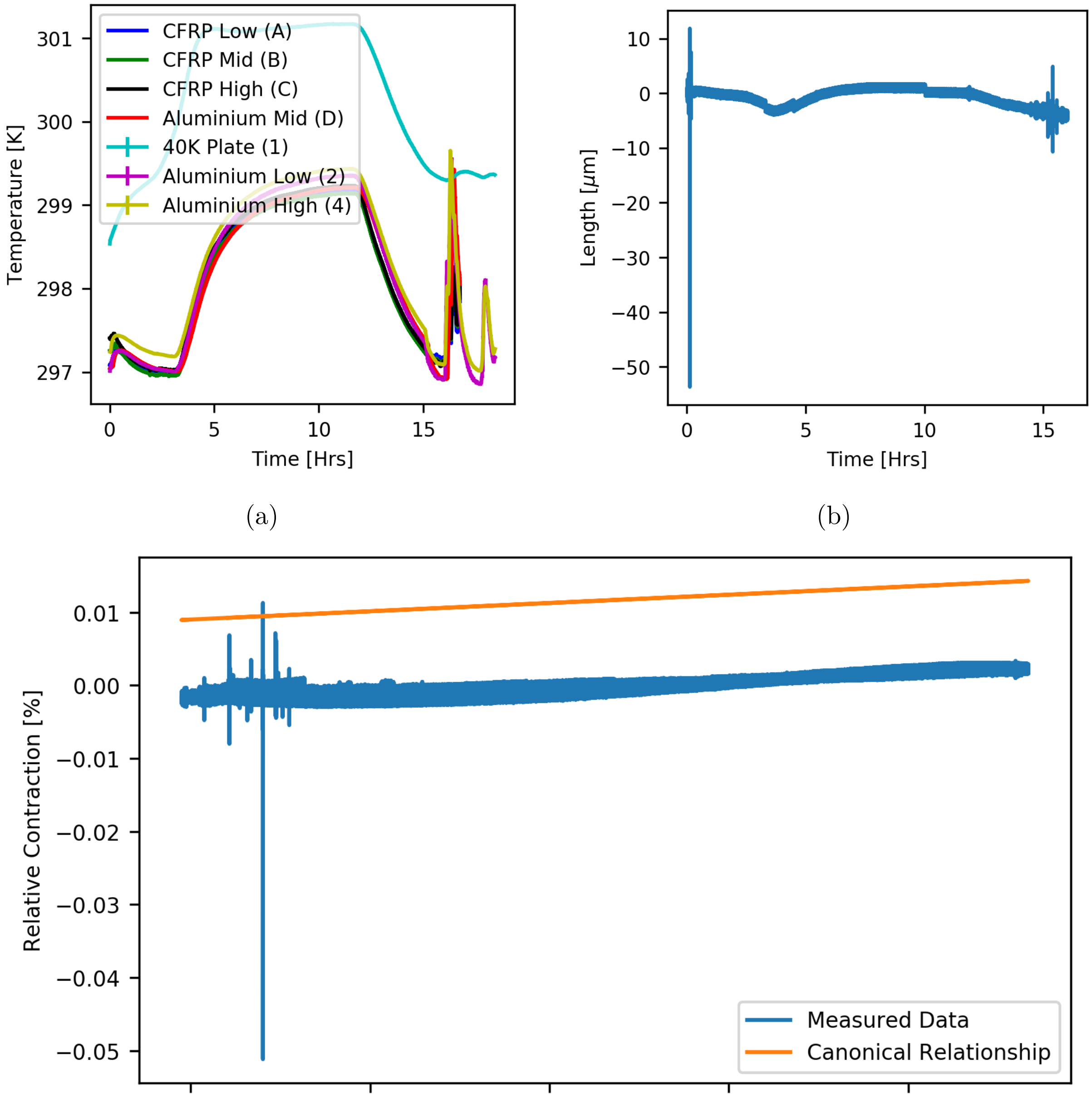

(a)

(b)

(c)

Figure B.8: Data for cryogenic thermal length contraction experiment on June 20th, 2018. (a) Temperature data for cryogenic thermal contraction measurements on June 20th, 2018. (b) Change in length recorded by the three-phase metrology system on June 20th, 2018. (c) Thermal contraction for the trial of June 20th, 2018.

## June 21st, 2018

On June 21st the aluminium sample was cooled again and the data recorded demonstrated that the FPGA does in fact have difficulties returning to it's original position as the drastic disparity between the cool-down and the warmup is almost certainly aphysical.

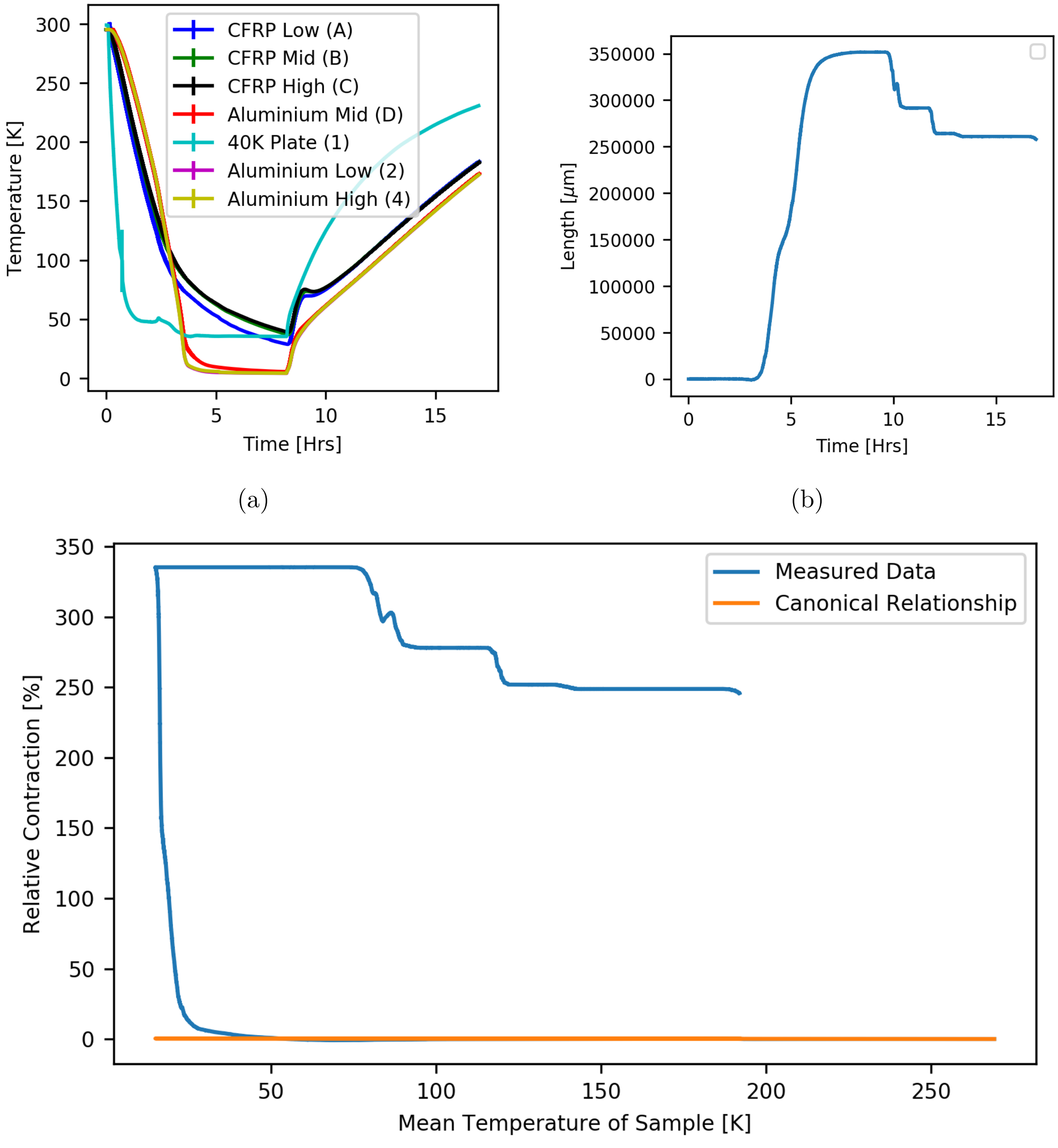

(a)

(b)

(c)

Figure B.9: Data for cryogenic thermal length contraction experiment on June 21st, 2018. (a) Temperature data for cryogenic thermal contraction measurements on June 21st, 2018. (b) Change in length recorded by the three-phase metrology system on June 21st, 2018. (c) Thermal contraction for the trial of June 21st, 2018.

# Appendix C

# CTIC Drawings

This appendix contains technical drawings of the components for the CTIC. Length units are in millimeters and the files from which these drawings are generated exist on the Spencer lab servers. Two of each of the side faces will be needed to complete the CTIC and three of each of the strut stands will be needed.

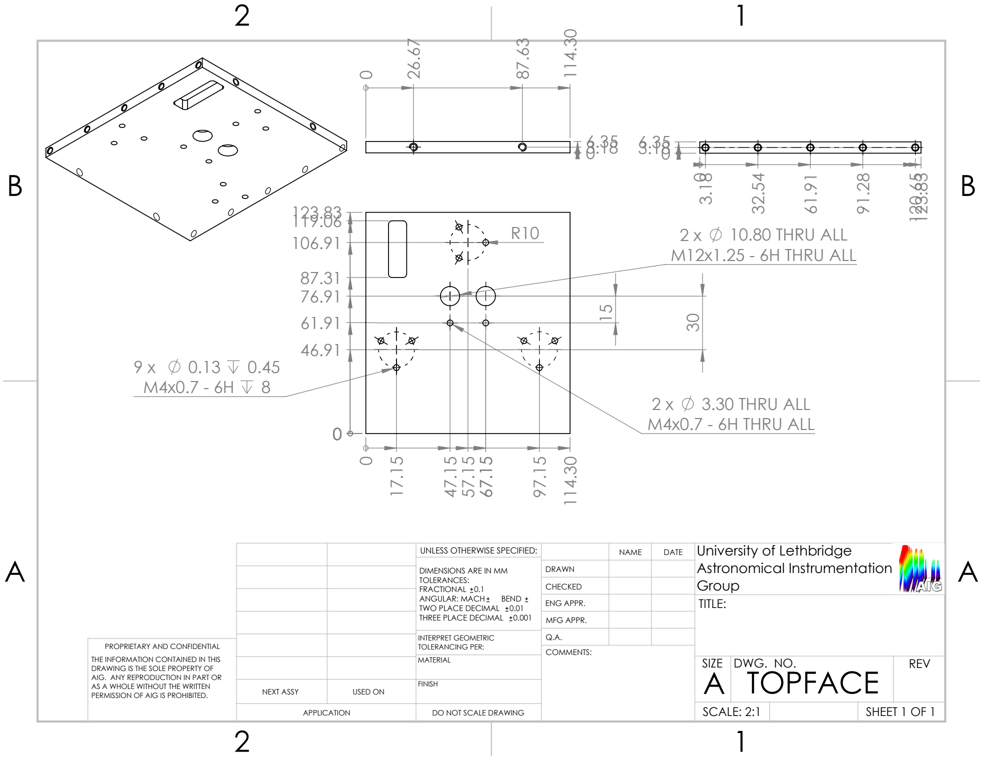

Figure C.1: Technical drawing for the top face of the CTIC. This is the most involved of the designs as it has many components to which it mates. Circular patterns of M4 holes must be tapped holes so that bolts can pass through to strut feet. Likewise the two M4 holes for mounting the apparatus internal to the box may be through holes with a nut on the opposite side. Two M12 holes must be threaded for the collimators.

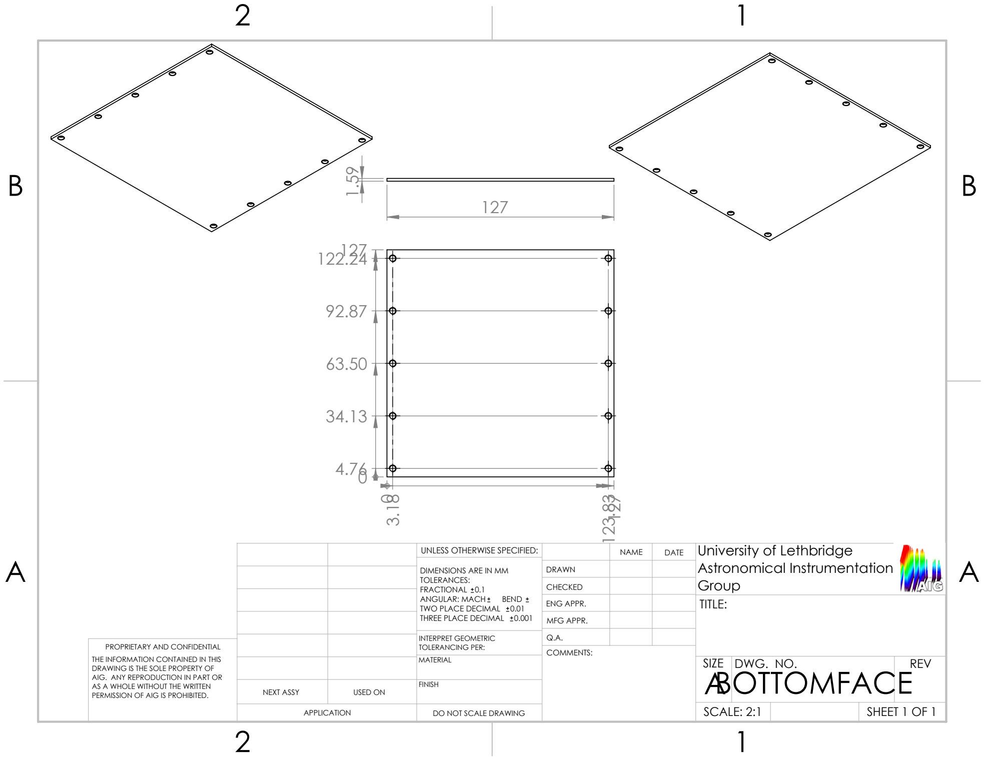

Figure C.2: The bottom face, or lid, of the CTIC. All holes are tapped holes.

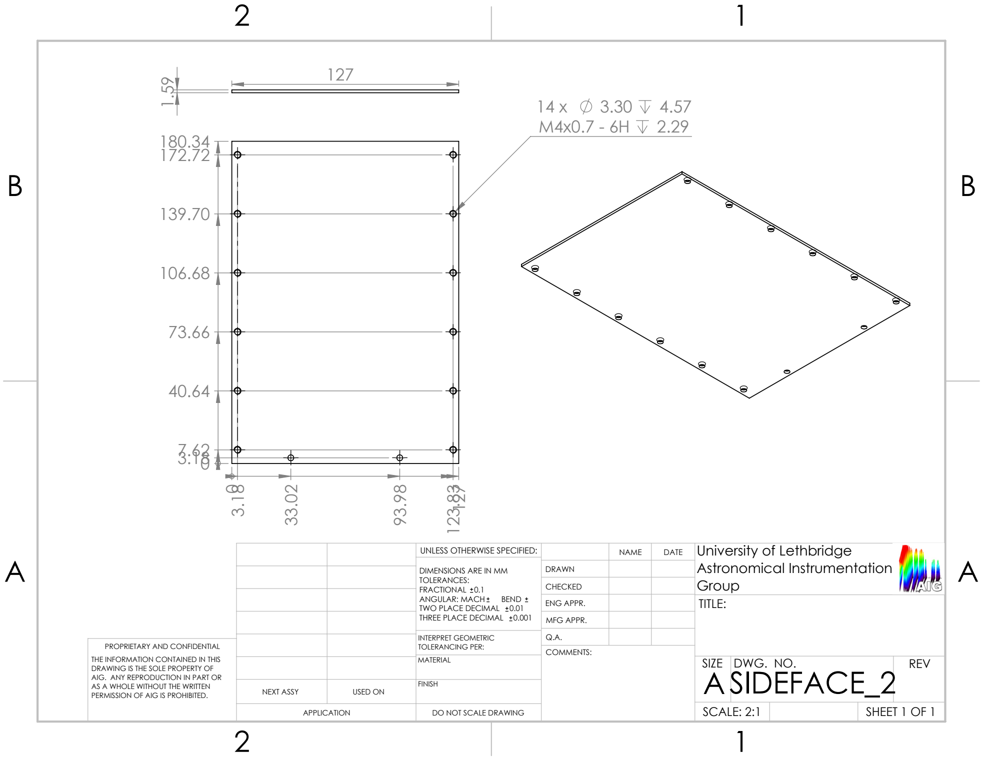

Figure C.3: The thin side face of the CTIC. All holes are tapped holes.

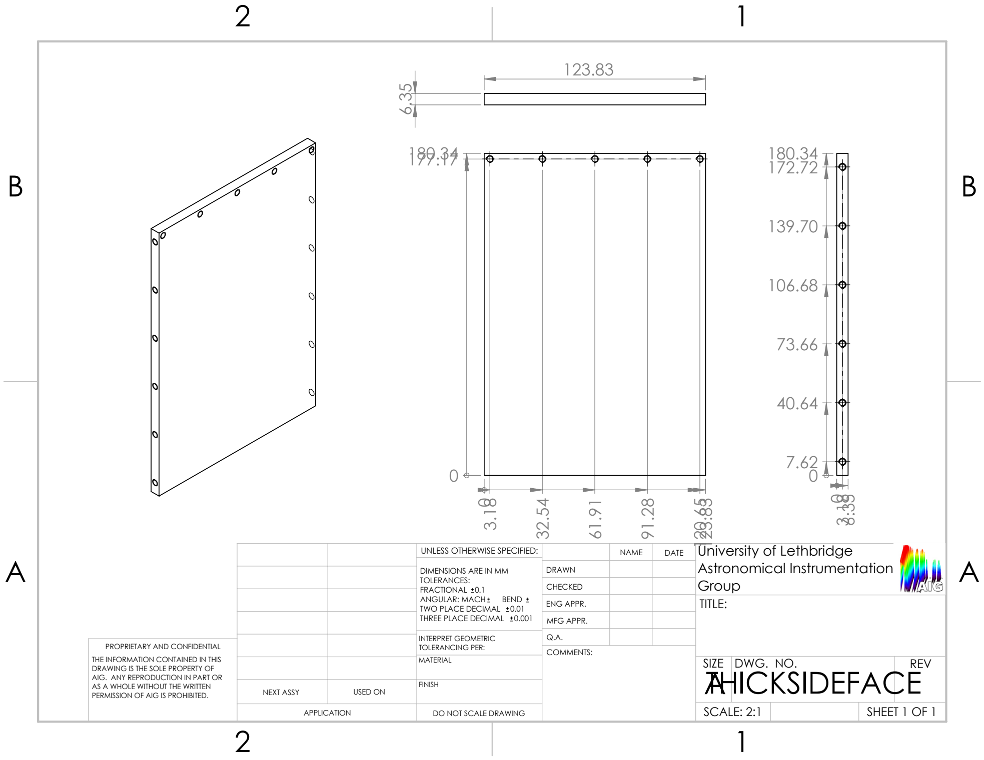

Figure C.4: The thick side face of the CTIC. Side holes along the length and bottom holes are threaded, with tapped holes at the top.

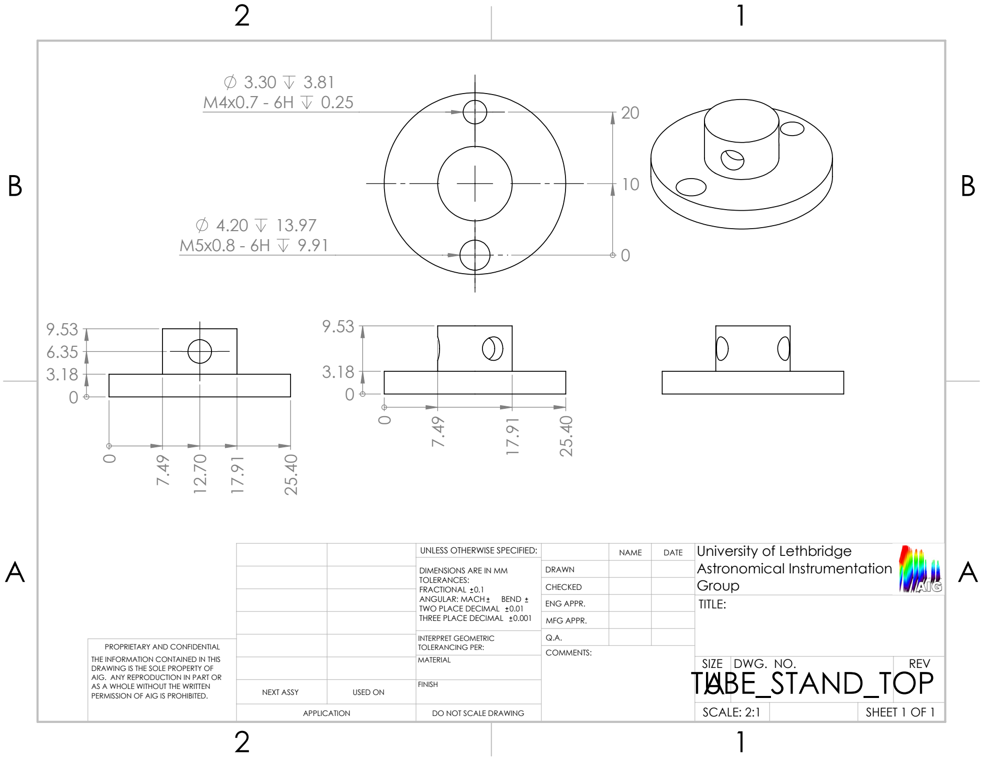

Figure C.5: The strut foot for bolting to the 4 K plate of the cryostat. Two holes for attaching to the plate must be tapped, and the three central holes must be threaded for attaching the strut.

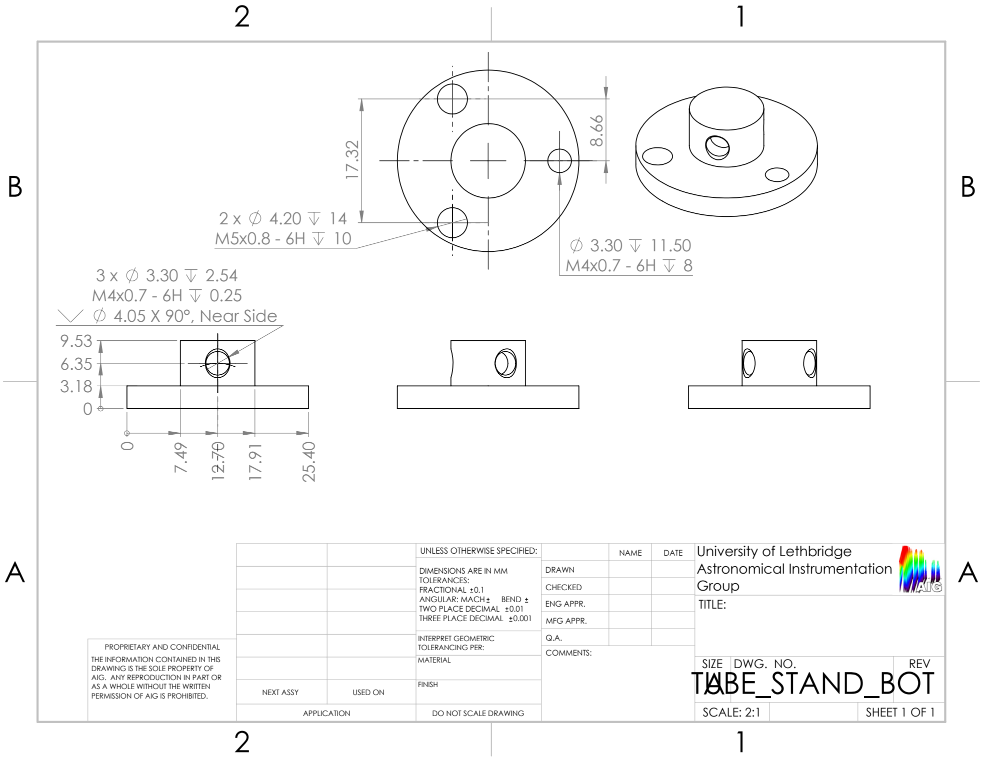

Figure C.6: The strut foot for bolting to the top face of the CTIC. Three holes for attaching to the face may be tapped or threaded, and the three central holes must be threaded for attaching the strut.